This is an authorized facsimile, made from the microfilm master copy of the original dissertation or masters thesis published by UMI.

The bibliographic information for this thesis is contained in UMI's Dissertation Abstracts database, the only central source for accessing almost every doctoral dissertation accepted in North America since 1861.

U·M·I Dissertation Information Service

University Microfilms International
A Bell & Howell Information Company
300 N. Zeeb Road, Ann Arbor, Michigan 48106
800-521-0600 OR 313/761-4700

Printed in 1993 by xerographic process
on acid-free paper

Order Number 9300275

The measurement of the magnetic moment of sigma plus using channeling in bent crystals

Chen, Dong, Ph.D.

State University of New York at Albany, 1992

U·M·I
300 N. Zeeb Rd.
Ann Arbor, MI 48106

THE MEASUREMENT OF THE MAGNETIC MOMENT OF SIGMA PLUS USING CHANNELING IN BENT CRYSTALS

By

Dong Chen

A Dissertation
Submitted to the State University of New York at Albany
in Partial Fulfillment of
the Requirements for the Degree of
Doctor of Philosophy

College of Sciences and Mathematics
Department of Physics

July, 1992

State University of New York at Albany

COLLEGE OF SCIENCE AND MATHEMATICS

The dissertation submitted by

Dong Chen

under the title

The Measurement of the Magnetic Moment of Σ^+ Using Channeling in Bent Crystals

has been read by the undersigned. It is hereby recommended for acceptance to the Faculty of the University in partial fulfillment of the requirements for the degree of Doctor of Philosophy.

(Signed)	7/10/92 (Date)
(Signed)	7/10/92 (Date)
(Signed)	7/10/92 (Date)
(Signed)	7/10/92 (Date)
(Signed)	7/10/92 (Date)
(Signed)	7/10/92 (Date)

Recommended by the Department of Physics: (Chairman's Signature)

Recommendation accepted by the Dean of Graduate Studies for the Graduate Academic Council:

(Signed)

(Date)

ABSTRACT

THE MEASUREMENT OF THE MAGNETIC MOMENT OF SIGMA PLUS USING CHANNELING IN BENT CRYSTALS

Dong Chen

State University of New York at Albany

July, 1992

The measurement of baryon magnetic moments has played an important role in determining the inner structure of baryons and constraining the quark models. The magnetic moments of the spin one-half baryons have been measured with good accuracy. The measurement of the magnetic moment of charm and beauty baryons is a challenge to experimental physicists because their life-times are a factor of 1000 shorter than conventional hyperons.

A new technique for measuring the magnetic moment of short-lived positively charged particles by using channeling in bent crystals has been tested in Fermilab Proton Center by using a polarized hyperon beam, specifically a Σ^+ beam. Two 4.5 cm long silicon crystals were bent by 1.6 mrad. There are eight implanted detectors on the surface of each crystal. These detectors are designed to measure the energy loss of those particles which pass through the crystal, and therefore let us select channeling particles. The bent crystal can provide to a relativistic channeling particle a very strong effective magnetic field. Under such a field, we observed spin precession of the channeled Σ^+ by an angle of the order of one radian. By measuring this precession angle, we find the value for the magnetic moment of the Σ^+, $2.40 \pm 0.46 \pm 0.40$ μ_N, the uncertainties being statistical and systematical, respectively. This value is consistent with the world average value of 2.42 ± 0.05 μ_N.

This new technique may be applied to measure the magnetic moments of short-lived positively charged particle such as Λ_c^+ in the future.

Acknowledgements

I would like to thank my advisor, Prof. C. R. Sun, for his support, patience and suggestions through my entire graduate studies. I was fortunate to also have Dr. R. A. Carrigan as my co-advisor. Without his daily guidance and knowledgeable advice, I could never have completed the research work reported herein. His remarkable effort to improve this thesis is greatly appreciated.

I am thankful to the rest of the members of my thesis committee: Prof. W. A. Gibson, A. Inomata, M. S. Alam and I. J. Kim for their valuable time and useful discussion.

A special thanks to the E761 collaboration. The success of the experiment was a team effort and I learnt a lot from almost everyone in our group. J. Lach and P. Cooper were always available for help and new ideas. V. Samsonov and A. Khanzadeev were the inspiration for the channeling section of the experiment. Their persistence and devotion really impressed me. I would like to thank my fellow graduate students: Antonio Morelos, Ivone Albuquerque, Roberto Mahon and Steve Timm. Of course, I can never thank too much my other two "stooges": "Moe", Maurice Foucher, and "Curly", Tim Dubbs. Their friendship made my life at Fermilab more joyful, and in return, I made them read the original, unpolished draft of this thesis, which might not have been so enjoyable. Their comments and suggestions were a great help.

My deep thanks to my parents and my sisters. Their understanding, love, encouragement and trust is always the source of my strength to go through the hard times in my life.

Contents

Acknowledgements ii

List of Figures vi

List of Tables xi

1 Introduction 2

2 Motivation 4

2.1 Theoretical Background 4

2.2 Experimental Background 7

3 Channeling 10

3.1 Introduction 10

3.2 Classical Theory of Channeling 11

3.2.1 Potential Well of Channeling Particles 11

3.2.2 Critical Angle of Channeling 14

3.2.3 Dechanneling 14

3.2.4 Energy Loss 15

3.3 Channeling in Bent Crystals 16

3.4 Previous Experimental Results 17

3.5 Measuring the Magnetic Moment Using Channeling in Bent Crystals 20

4 Apparatus 24

4.1 Introduction 24

4.2 Proton Center Beam Line 24
4.3 Target, Hyperon Magnet, and Hyperon Channel 26
4.3.1 Target 26
4.3.2 Hyperon Magnet and Hyperon Channel 27
4.4 Spectrometer 27
4.4.1 Hyperon Spectrometer 30
4.4.2 Baryon Spectrometer 30
4.5 Crystals and Bending Device 31
4.5.1 Crystals 31
4.5.2 Goniometer 31
4.5.3 Silicon Detectors on the Surface of Crystals 34
4.6 Crystal Channeling Trigger 34
4.6.1 Beam Trigger 36
4.6.2 Channeling Trigger 38
4.7 Data Acquisition 38
4.8 Rate and Tape 41

5 Alignment of Crystals **43**
5.1 Motion Calibrations 43
5.2 Online Alignment 46
5.3 Electronic Problem with the Crystals 48
5.4 Offline Alignment 50

6 Reconstruction of Channeling Events **55**
6.1 Event Reconstruction 55
6.2 Selecting Channeling Events 58
6.3 Problems with the 2nd Crystal 61
6.4 Crystal and Channeling Property Study 65
6.4.1 Crystal With Beam Phase Space 65
6.4.2 Channeling Incident Angle 68
6.4.3 Channeling Outgoing Angle 75
6.4.4 Crystal Bending Angle 79

6.5 Channeling Fraction 84
6.5.1 Theoretical Calculation 84
6.5.2 Experimental Estimation 86

7 Reconstruction of Channeled Σ^+ 89
7.1 Reconstruction of Nonchanneled Σ^+ 89
7.2 Reconstruction of Channeled Σ^+ Using a Channeling Cut 90
7.3 Reconstruction of Channeled Σ^+ without a Channeling Cut 99

8 Measurement of the Spin Precession and Magnetic Moment of Σ^+ 103
8.1 Polarization Measurement of the Σ^+ before the Crystals 103
8.2 Polarization Measurement of the Σ^+ after the Crystals 106
8.2.1 Theoretical Estimation 106
8.2.2 Experimental Measurement with the Channeling Cut 106
8.2.3 Experimental Measurement without the Channeling Cut . . . 109
8.3 Magnetic Moment of the Σ^+ 115
8.4 Systematic Error 116

9 Conclusions 119

List of Figures

2.1 Schematic diagram of the Σ^+ polarization production and precession in a magnetic field. 9

3.1 Planar channeling of a charged particle between two crystal planes. . 11

3.2 Comparison of the normalized Lindhard and Moliere potentials for He incident near the (110) planes of Si. 13

3.3 Modified continuum (110) planar potential of bent silicon for 10 GeV protons where x = 0 is in the central position between two adjacent planes. The bending radius is 10 cm. 18

3.4 Schematics of channeled planar orbits in (a) an unbent and (b) bent crystal. The center of the orbit moves toward the outer plane in the bent case. λ is the wavelength of the particle motion. 19

3.5 Electronic field and effective magnetic field for channeling particle in a bent crystal 21

3.6 Polarization vector precession in the effective magnetic field. ϕ is the precession angle. 22

4.1 Schematic diagram (plan view) of PC3 beam line. 25

4.2 The copper target 27

4.3 The hyperon magnet channel. 28

4.4 Schematic diagram of E761 spectrometer (not to scale). There are four main parts: target with hyperon magnet, hyperon spectrometer, baryon spectrometer and Crystals. The diagram also shows the decay of $\Sigma^+ \rightarrow p\pi^0$ with $\pi^0 \rightarrow \gamma\gamma$. 29

4.5 Seven crystals and their implanted silicon detectors on the surface of each crystal. 32
4.6 Crystal bending device. 33
4.7 Analytical calculation of the ionization losses. Small energy losses correspond to channeled particles; and the normal Landau energy loss distribution corresponds to nonchanneled particles. 35
4.8 Schematic of the energy loss signal being sent to ADC. 36
4.9 Anti counter with the crystals 37
4.10 Channeling trigger schematic diagram. 39
4.11 Data aquisition schematic diagram. 40

5.1 The linear motion motors with the ANTI counter on the top: (a) front view, (b) side view. 44
5.2 Schematic of the motion control system for both linear motions and goniometer. 45
5.3 Channeling scanning plot from a previous experiment. The x axis is the scanning angle and the y axis is the ratio of events in the smaller energy loss area over the number of events in the higher energy loss area. 47
5.4 (a) Normalized energy loss, ΔE, spectrum of a scanning run at the channeling position. (b) The height in the crystal Y (cm) versus normalized energy loss ΔE. 49
5.5 Normalized energy loss spectrum of several scanning runs after offline y cut: (a) goniometer at 700 μrad from the channeling position, (b) goniometer at 320 μrad from the channeling position, (c) goniometer at 19 μrad from the channeling position, and (d) goniometer at the channeling position. 52
5.6 Particle deflection angle distribution in the y direction for (a) goniometer at 700 μrad from the channeling position, (b) goniometer at 320 μrad from the channeling position, (c) goniometer at 19 μrad from the channeling position, and (d) goniometer at the channeling position. . 53

5.7 Channeling scanning plot from our offline alignment for the 5th crystal. Ratio of channeled events to nonchanneled events versus goniometer steps. 54

6.1 THETA versus R plot before R cut 57

6.2 (a) Energy loss spectrum from the center pad of the 5th crystal for the events that passed the PASS1. The energy loss was normalized to the Landau peak value. (b) Bending angle, DTY, distribution. The peak at -1.6 mrad corresponds to the 5th crystal, the one at +1.6 mrad to the 2nd crystal. 59

6.3 Normalized energy loss, ΔE, from the center pad of the 5th crystal versus the thickness of the crystal, Y, for RUN 4266. The area between the two straight lines was selected as the good part of the crystal. . . 60

6.4 (a) Normalized energy loss spectrum of center pad of good portion of the 5th crystal. (b) DTY distribution after strong energy loss channeling cut. 62

6.5 DTY distribution after energy loss channeling cut only on the center pad. 63

6.6 The Si-H film of the (111) plane of the 2nd crystal. The slip lines were in the crystal axis direction. 64

6.7 Computer simulation plot of crystal bending angle versus the crystal length. The total bending angle is normalized to 1.6 mrad. The angle difference between the 6th pad and the end of the crystal is about 60 μrad. 66

6.8 DTY distribution of the good part of 2nd crystal under the energy loss cut of (a) the coincidence of the first pad and last pad, and (b) the center pad only. 67

6.9 The size of (a) the total hyperon beam and (b) the part of beam going through the crystals. 69

6.10 The x phase space of (a) the total hyperon beam and (b) the part of beam going through the crystals. 70

6.11 The y phase space of (a) the total hyperon beam and (b) the part of beam going through the crystals. 70
6.12 The beam size that covered (a) the 5th crystal and (b) the 2nd crystal. 71
6.13 Beam phase space that covered the 5th crystal in (a) x direction and (b) y direction. 71
6.14 TY1 versus x under the strong channeling cut for (a) the 5th crystal and (b) the 2nd crystal. 73
6.15 TY1 of channeling events of a 0.05 cm x strip for (a) the 5th crystal and (b) the 2nd crystal. 74
6.16 TY1 as a function of x for (a) the 5th crystal and (b) the 2nd crystal. Straight line is the fit function. 76
6.17 Corrected channeling incident angle, TY1C, distribution for (a) the 5th crystal and (b) the 2nd crystal. 77
6.18 Channeling outgoing angle TY2 as a function of x for (a) the 5th crystal and (b) the 2nd crystal. 78
6.19 TY2 of channeling events of a 0.05 cm x strip for (a) the 5th crystal and (b) the 2nd crystal. 80
6.20 TY2 as a function of x for (a) the 5th crystal and (b) the 2nd crystal. Straight line is the fit function. 81
6.21 Channeling bending angle DTY as a function of x for (a) the 5th crystal and (b) the 2nd crystal. 82
6.22 DTY as a function of x for (a) the 5th crystal and (b) the 2nd crystal. Straight line is the fit function. 83
6.23 Crystal bending angle DTY under the strong channeling cut for (a) the 5th crystal and (b) the 2nd crystal. 84
6.24 Crystal bending angle DTY under the loose channeling cut for (a) the 5th crystal and (b) the 2nd crystal. 85
6.25 Potential and energy levels for silicon (111) plane. There are two potential wells. The deeper potential well is the major region for channeling. 85

7.1 THETA versus R plot of theoretical calculation for Σ^+ decay. 91

7.2 THETA versus R plot of the nonchanneling triggered data. 92
7.3 ZV distribution of the events after R and THETA cut. 93
7.4 Missing mass squared distribution of nonchanneled Σ^+. 94
7.5 THETA versus R after bending angle modification for (a) nonchanneled Σ^+ and for (b) channeled events. 96
7.6 Missing mass squared distribution of channeled Σ^+ under the channeling cut for (a) the 5th crystal and (b) the 2nd crystal. 98
7.7 ZV distributions for (a) nonchanneled events and (b) channeled events. 100
7.8 Missing mass squared distributions of channeled Σ^+ for (a) the 5th crystal and (b) the 2nd crystal. No channeling cut was used. 101

8.1 The $\frac{N_i^+ - N_i^-}{N_i^+ + N_i^-}$ distribution of nonchanneled Σ^+. About 65,000 nonchanneled Σ^+ are used here. 105
8.2 The initial polarization of Σ^+ and the final polarization of channeled Σ^+ from theoretical prediction for the 5th and 2nd crystals. 107
8.3 The $\frac{N_i^+ - N_i^-}{N_i^+ + N_i^-}$ distribution of the channeled Σ^+ with the channeling cut for (a) the 5th crystal and (b) the 2nd crystal. 108
8.4 The polarization and precession angle of the channeled Σ^+ measured with the channeling cut. The dashed lines are the initial value and the theoretical predicted value. 110
8.5 The $\frac{N_i^+ - N_i^-}{N_i^+ + N_i^-}$ distribution of the events in the signal area for (a) the 5th crystal and (b) the 2nd crystal. 111
8.6 The $\frac{N_i^+ - N_i^-}{N_i^+ + N_i^-}$ distribution of the events in the background area for (a) the 5th crystal and (b) the 2nd crystal. 112
8.7 The polarization and precession angle of the channeled Σ^+ measured without the channeling cut. The dashed lines are the initial value and the theoretical predicted value. 114
8.8 The χ^2 distribution of the systematic study. Connected line is the theoretical distribution. 118

9.1 Experimental measurements of Σ^+ magnetic moment in history. . . . 120

List of Tables

2.1 The magnetic moments of spin $\frac{1}{2}$ baryons from the prediction of the naive quark model and from experimental data. Using the p, n and . 6

4.1 Location of the important apparatus. Z = 0 is at the exit of the hyperon magnet. 31

4.2 Summary of the runs, tapes, and events. 42

6.1 Beam and trigger rate for channeling run 4266 and nonchanneled run 4388. 87

6.2 Channeling Fraction from one tape data of run 4266. 88

7.1 Statistics of reconstructed channeled Σ^+ under the channeling cut. . . 97

7.2 Statistics of reconstructed channeled Σ^+ and background without energy loss channeling cut. 102

8.1 Polarization of Σ^+ before the crystals. 105

8.2 Polarization results of the channeled Σ^+ with channeling cut. 109

8.3 Polarization results from our measurement. $\mathbf{A} = \alpha\mathbf{P}$ for Σ^+s. 113

8.4 Results of the μ_{Σ^+} measurement with statistical error only. 115

8.5 Final results of the μ_{Σ^+} measurement. 117

Chapter 1

Introduction

The Fermi National Accelerator Laboratory (Fermilab) experiment E761 was carried out from January to August, 1990 in the Fermilab proton center beamline by a group of physicists from FNAL; Institute of High Energy Physics, People's Republic of China; Petersburg Nuclear Physics Institute, Russia; University of Iowa; University of Sao Paulo, Brazil; Yale University; Centro Brasileiro de Pesquisas-fisicas, Brazil; Conselho Nacional de Pesquisas CNPq, Brazil; State University of New York at Albany; and University of Bristol, United Kingdom.

The main purpose of the experiment was to measure the branching ratio and asymmetry parameter of the Σ^+ radiative decay [1]. Along with the main goal, a new technique for measuring the magnetic moment of short-lived positively charged particles using channeling in bent crystals was tested.

Channeling of high energy particles in bent crystals has been observed in several experiments [2, 3, 4, 5, 6, 7, 8]. This technique has already found applications in the extraction of high energy beams [7, 8]. Another important application of channeling is to precess the spin direction of a polarized beam. Our experiment was designed to investigate this application [9].

A polarized Σ^+ beam was produced in the Fermilab proton center beam line via the inclusive reaction

$$\mathrm{p(800GeV)} + \mathrm{Cu} \Rightarrow \Sigma^+ + \mathrm{X}$$

The initial polarization of the Σ^+ before entering the crystals was measured, with the statistical error, to be 12 $\pm$ 1 % in a certain direction. If the polarization vector was precessed by the bent crystals, its direction after the crystals should be changed. By measuring the polarization of about 2000 channeled Σ^+ after the crystals, we measured the precession angle. This is the first observation of spin precession of particles channeled in a bent crystal. From the precession angle, the magnetic moment of Σ^+ was determined to be 2.40 $\pm$ 0.46 $\pm$ 0.40 μ_N, the first error is statistical and the second is systematical, which is consistent with the Particle Data Group value 2.42 $\pm$ 0.05 μ_N [10]. Here μ_N is the nuclear magneton.

This new technique might allow the measurement of magnetic moments of heavy quark baryons, for instance, charm baryons. Charm baryons travel only a few centimeters even at the highest available accelerator energy due to their short lifetimes. These short lifetimes imply that classical spin precession techniques using conventional magnets would produce negligibly small spin precession angles. On the other hand, channeling in bent crystals can provide an equivalent magnetic field of up to 1000 T thus offering the potential of significant precession angles within a few centimeters of crystal length.

Chapter 2 describes the theoretical motivation and experimental status of hyperon magnetic moment measurements. A general explanation of the theory of crystal channeling as well as an introduction to some important channeling properties are given in chapter 3. A detailed description of the experimental apparatus is given in chapter 4. The procedure for crystal scanning is described in chapter 5. Chapter 6 discusses how we selected channeling events and measured the channeling properties using the long-lived channeled particles. The reconstruction of the channeled Σ^+ is explained in chapter 7. Chapter 8 illustrates how we measured the polarization of the channeled Σ^+ and therefore measured its magnetic moment. The future prospects of measuring the magnetic moment of short-lived positively charged heavy quark baryons, specifically the Λ_c^+, using channeling in bent crystals is discussed in the last chapter, chapter 9.

Chapter 2

Motivation

This chapter presents some theoretical calculations and a summary of current experimental results of the magnetic moments of hyperons.

2.1 Theoretical Background

The magnetic moment is one of the static properties of a particle. For a spin-S particle, its magnetic moment is defined as

$$\vec{\mu} = \frac{eg_s}{2mc}\vec{S}, \tag{2.1}$$

where g is the gyromagnetic ratio, e is the charge of the particle, m is its mass, and $\vec{S}$ is its intrinsic spin.

If we bring a magnetic moment into a magnetic field, $\vec{B}$, a torque, $\vec{\tau}$, is applied to the magnetic moment:

$$\vec{\tau} = \vec{\mu} \times \vec{B} \tag{2.2}$$

and the interaction energy, E, is

$$E = -\vec{\mu} \cdot \vec{B}. \tag{2.3}$$

If we assume the quark is a point-like particle, the magnetic moment of the quark is

$$\vec{\mu_q} = \frac{ge_q\hbar}{4m_qc}\vec{\sigma}, \tag{2.4}$$

where e_q, m_q, $\vec{\sigma}$ are quark's charge, mass and spin unit vector respectively.

The quark model assumes that the baryons are formed by constituent quarks. Therefore, the magnetic moment of a baryon is the sum of the contribution from both the spin moments and the orbital angular momenta of the quarks that make up the baryon.

Studying the magnetic moments of baryons has played an important role in the development of our current understanding of the spin and angular momentum structure of baryon wave functions, and of the values of quark magnetic moments and masses. Since the theoretically predicted value of the magnetic moment considerably depends on the models that are used, an accurate measurement of the magnetic moment provides a useful tool to check the models.

Since the first modern calculation of the baryon magnetic moments carried out by Coleman and Glashow [11], a model called the naive quark model has been developed. The naive quark model assumes:

1) Quarks are point-like particles.

2) Baryon magnetic moments arise solely from quark magnetic moments with orbital effects, relativistic effects and exchange effects being negligible,

$$\vec{\mu_B} = \sum \vec{\mu_q}. \tag{2.5}$$

Therefore, the baryon magnetic moments can be derived in terms of quark magnetic moments by using the baryon spin wavefunction [12].

Using the well measured magnetic moments of the proton, neutron, and Λ as inputs, the magnetic moments of spin $\frac{1}{2}$ hyperons were calculated. The theoretical values and the experimental data [10] are listed in Table 2.1. The unit of the magnetic moments is μ_N, and $\mu_N = e\hbar/2m_p c$ is the nuclear magnetons. For Σ^0, because it decays electromagnetically, $\Sigma^0 \rightarrow \Lambda\gamma$ with lifetime in the order of 10^{-20} s, we are not able to measure its static magnetic moment. However, a related quantity, the $\Sigma^0 - \Lambda$ transition magnetic moment, which is just as fundamental as the static moment, could be and was measured [13] as I quoted in the Table. The theoretical value based on the naive model agreed qualitatively with the experimental data. This was a good indication that the model was basically correct. But the obvious

Baryon	Magnetic Moment Prediction	Nuclear magnetons	Experiment Data
P	$4/3\ \mu_u - 1/3\ \mu_d$	Input	2.7928
n	$4/3\ \mu_d - 1/3\ \mu_u$		-1.9130
Λ	μ_s		-0.613 ± 0.004
Σ^+	$4/3\ \mu_u - 1/3\ \mu_s$	2.673	2.42 ± 0.05
Σ^-	$4/3\ \mu_d - 1/3\ \mu_s$	-1.091	-1.157 ± 0.025
$\Sigma^0 - \Lambda$	$\sqrt{1/3}(\mu_d - \mu_u)$	1.63	1.61 ± 0.08
Ξ^0	$4/3\ \mu_s - 1/3\ \mu_u$	-1.435	-1.250 ± 0.014
Ξ^-	$4/3\ \mu_s - 1/3\ \mu_d$	-0.493	-0.679 ± 0.031

Table 2.1: The magnetic moments of spin $\frac{1}{2}$ baryons from the prediction of the naive quark model and from experimental data.

discrepancies between the theoretical values and experimental data have required some modifications of the naive quark model.

There have been many different approaches to modifying the naive quark model to calculate the magnetic moment.

Isgur and Karl [14] added small contributions to the naive model. They included relativistic correction and the configuration mixing between ground-state wavefunctions and higher states. The isospin mixing was also used as a correction. These corrections made the calculated magnetic moments of spin $\frac{1}{2}$ hyperons in better agreement with measurements, but the remaining discrepancies were still noticeable.

Verma [15] introduced the concept of effective charge of a quark in baryon. He assumed that when a quark is being probed by a soft photon, the other two quarks of the baryon may shield the charge of the quark under probe, thus modifying the charge and hence the magnetic moment of the quark. His approach also reduced the discrepancies between the theoretical values and experimental values of the baryon magnetic moments compared to the naive quark model.

Chodos et al.[16, 17] proposed a model, called the MIT bag model, which treats the quarks as massless, non-interacting, free particles confined to a finite region of space, called a bag. This model provides quantitative results for the proton and neutron magnetic moments as well as hyperon magnetic moments [18]. However, the prediction of the proton magnetic moment of 1.9 μ_N is still far from the experimental

value of 2.79 μ_N. The cloudy bag model introduced the pion field and included lowest-order pionic corrections to the calculation of the magnetic moments of hyperons. Ushio [19] added the one-gluon exchange correction to the bag model. He gave a better result for μ_Λ and μ_{Ξ_-}.

There are other models and attempts, such as the chiral bag model [20] and model independent QCD sum rules [21, 22]. However, no attempt has, so far, succeeded in finding a convincing mechanism to bridge the gap between theory and experiment. The experimental data still play the constraining role to the model builder.

2.2 Experimental Background

All the magnetic moments of the spin $\frac{1}{2}$ baryons and the transition moment for Σ^0 – Λ have been measured. The results are shown in Table 2.1. All the measurements except those of the proton, neutron and Σ^0 – Λ were obtained using a technique called spin precession. Fig. 2.1 illustrates the conventional technique that is used at Fermilab to measure the magnetic moment of Σ^+ [23]. If the expectation value of the particles' spins reaches a maximum value (s) in a given direction ($\vec{e_0}$), the particles are polarized with the polarization vector, $\vec{\mathbf{P}}$, defined as

$$\vec{\mathbf{P}} = s\vec{e_0} \tag{2.6}$$

At Fermilab, the polarized hyperon beam is produced through a strong interaction by using an unpolarized proton beam impinging on an unpolarized target. According to the parity conservation law in strong interactions, the direction of the polarization vector of the Σ^+ is given by the direction of incoming proton and outgoing Σ^+ at the target

$$\hat{n} = \frac{\vec{k}_{proton} \times \vec{k}_{\Sigma^+}}{|\vec{k}_{proton} \times \vec{k}_{\Sigma^+}|}. \tag{2.7}$$

In Fig. 2.1, the polarization vector, $\vec{\mathbf{P}}$, is in the Y direction normal to the production plane, the XZ plane. The mechanism of the spin production through the strong interaction is still under study by physicists and there is not yet a satisfactory explanation.

When the Σ^+ passes a magnetic field ($\vec{B}$) that is perpendicular to the polarization ($\vec{B}$ is in x) direction, the polarization vector $\vec{\mathbf{P}}$ rotates on the YZ plane. The precession

angle, $\Delta\phi$, is proportional to its magnetic moment μ_{Σ^+}. The polarization vector can be measured from the decay proton distribution through the equation

$$\frac{dN}{d\Omega} = \frac{N}{4\pi}(1 + \alpha \mathbf{P} \cdot \vec{\mathrm{p}}), \tag{2.8}$$

where N is the number of events, Ω is the solid angle, $\vec{p}$ is the proton direction in the Σ^+ rest frame, α is the asymmetry parameter of $\Sigma^+ \rightarrow \mathrm{p}\ \pi^0$, and $\mathbf{P}$ is the polarization at the point of decay. From the measured polarizations before and after the magnetic field B, we can calculate the precession angle. If we know the magnetic field B and measure the momentum of the Σ^+, then, the magnetic moment of Σ^+ can be determined.

The advantage of Fermilab hyperon experiments, compared with previous bubble chamber and spark chamber experiments, is that the high flux, high momentum (hundreds of GeV/c) hyperon beams at Fermilab give rise to hyperon decay lengths of a few to tens of meters. For the polarization vector of the hyperons, this results in a sufficient precession angle in a conventional magnet.

But for the baryons whose lifetimes are much shorter than the hyperons, for instance, 500 GeV/c Λ_c^+ would have decay lengths of only 1.25 cm, a conventional magnet will not be able to produce a measurable angle of precession of the polarization vector before the baryons decay.

Measuring the magnetic moments of these much shorter lived particle is now becoming a challenge to experimental particle physicists. Some theorists, such as S. N. Jena and D. P. Rath [24], E. M. Nyman and D. O. Riska [25], J. Kunz and P. J. Mulders [26], and D. P. Min and Y. Oh [27], have already predicted the values of magnetic moments of charmed and b-flavored baryons. One proposal to meet the challenge is to use the strong effective magnetic field inside the channels of a bent crystal instead of the conventional magnetic field to precess the polarization vector and measure the magnetic moment.

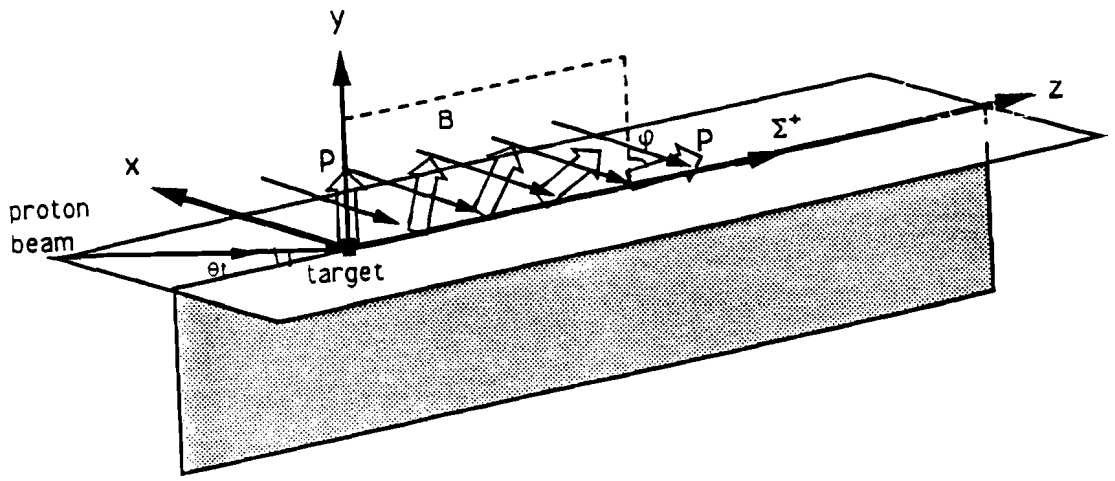

Figure 2.1: Schematic diagram of the Σ^+ polarization production and precession in a magnetic field.

Chapter 3

Channeling

3.1 Introduction

Channeling effects were observed at the beginning of the 1960's. Positively charged particles, which move parallel to the channels formed by major crystal planes or axes, are trapped in the channels because the repulsive force between the particles and the major lattice nuclei sites suppress the close interaction.

Lindhard [28], Datz, Noggle, Moak [29], and Thompson and Morgan [30] developed a classical theory which approximately explains most of the channeling phenomena in principle. Several effects, such as reduction of energy loss for a channeled particle and the concept of a critical angle, have been introduced and explained by the classical theory.

The channeling effect has also been used and studied at higher energies in recent years. I will discuss in this chapter the process of bending high energy beams in a curved crystal. The subject of the thesis will be the application of channeling in bent crystals for measuring the magnetic moments of short-lived particles.

The crystals we used were cut along the (111) plane. To introduce the channeling theory, I will use the (110) plane, instead, for the sake of simplicity. In later chapters, when we calculate the channeling properties, I will use the (111) plane.

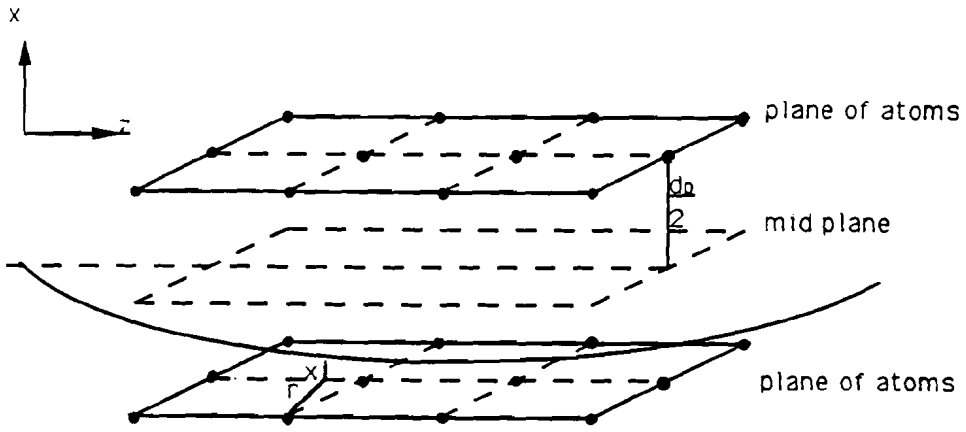

Figure 3.1: Planar channeling of a charged particle between two crystal planes.

3.2 Classical Theory of Channeling

3.2.1 Potential Well of Channeling Particles

When a particle is trapped between crystal planes, for instance the (110) plane of Si, we call it planar channeling. If the particle is trapped in the transverse well formed by axial strings, [111] of Si for example, it is called axial channeling. Planar channeling, compared with axial channeling, is better explained in theory due to the relative simplicity of the one dimensional potential. I will only introduce planar channeling theory here.

Ellison [32, 33, 34, 35] made a series of detailed calculations of the properties of channeling. I am going to briefly introduce his approach here. The behavior of a channeled particle is based on the classic equation of motion of a charged particle due to the continuum potential of the channel. In the case of planar channeling, the motion of a particle along a major crystal plane is due to the potential of the nearby planes of atoms, see Fig. 3.1.

The equation of motion of a charged channeled particle in x (the transverse distance from the center of the channel) versus z (the distance down the channel) under

the continuum potential approximation is

$$\frac{d^2x}{dz^2} + \frac{1}{2E}\frac{\partial V(x)}{\partial x} = 0, \tag{3.1}$$

where E is the relativistic longitudinal energy of the particle and

$$V(x) = U(\frac{1}{2}d_p + x) + U(\frac{1}{2}d_p - x) - 2U(\frac{1}{2}d_p). \tag{3.2}$$

U(x) is the planar-continuum potential experienced by the particle at a distance x from the plane and d_p is the separation between the atomic planes.

One of the most commonly used planar-continuum potentials is based on the Lindhard approximation. The Lindhard continuum potential can be written [36] as

$$U(x) = 2\pi Z_1 Z_2 e^2 N d_p[(x^2 + C^2a^2)^{\frac{1}{2}} - x]. \tag{3.3}$$

where N is the atomic density of the crystals, a = 0.8853 $a_0(Z_1^{\frac{2}{3}} + Z_2^{\frac{2}{3}})^{-\frac{1}{2}}$ is the screening distance, and a_0 is the Bohr radius. Z_1 is the atomic number of the incident particle, Z_2 is the atomic number of the lattice atoms, and C is a standard constant which he sets equal to $\sqrt{3}$.

With the Lindhard approximation, the potential can be written as

$$V(x) = K\{[(1+X)^2 + \frac{12}{D^2}]^{\frac{1}{2}} + [(1-X)^2 + \frac{12}{D^2}]^{\frac{1}{2}} - 2(1 + \frac{12}{D^2})^{\frac{1}{2}}\}, \tag{3.4}$$

or

$$V(x) = KW(X, D) \tag{3.5}$$

where W(X,D) is the normalized form of the continuum potential, X = $2x/d_p$ is the normalized distance, D = d_p/a is the normalized planar separation and K = $\pi Z_1 Z_2 e^2 N d_p$ is the parameter scaling the magnitude of the potential.

Another commonly used planar-continuum potential is based on the Moliere approximation. The normalized potential W(X,D) from both approximations as a function of normalized position X (taken from Ellison [33]) is plotted in Fig. 3.2.

From Fig. 3.2 we see that both potentials are very close to the harmonic approximation potential. The harmonic-continuum potential, V(x) = V_0x^2, which was used by Alexandar [37], Kumakhov [38] and Kim [39], gives very good qualitativel results.

The effects of quantum mechanics are more important for lighter particles and lower incident energies. For our purpose these effects are very small.

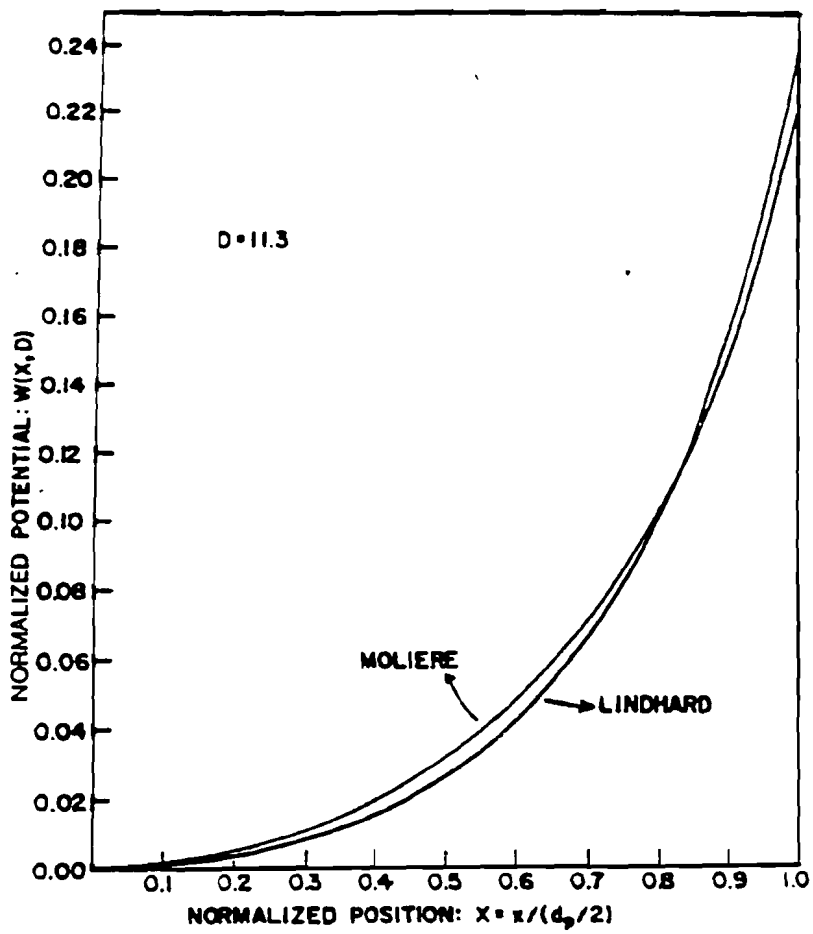

Figure 3.2: Comparison of the normalized Lindhard and Moliere potentials for He incident near the (110) planes of Si.

3.2.2 Critical Angle of Channeling

The critical angle is defined as the maximum incident angle under which the particle will be channeled.

For relativistic particles, the critical angle for planar channeling can be derived, as Lindhard did [36], by considering the closest distance the particle can approach to the planes, X_C. At that distance, the kinetic energy of the transverse component is equal to zero, so that the transverse energy is equal to the potential energy

$$E \cdot \theta^2 = V(X_C),$$

where E is the energy of the particle and θ is the angle between the particle momentum and the crystal plane. The same principle applies to axial channeling, too.

The planar critical angle from the Lindhard calculation is given as

$$\theta_{c,p} = [4\pi Z_1 Z_2 e^2 N d_p C a / E]^{\frac{1}{2}}. \tag{3.6}$$

For the axial case the critical angle is given as

$$\theta_{c,a} = [4 Z_1 Z_2 e^2 / E d_a]^{\frac{1}{2}} \tag{3.7}$$

where d_a is the atomic spacing along the corresponding axis. The equations tell us that the higher the energy of incident particle, the smaller the critical angle will be.

To a good approximation, the critical angle of the planar channeling is three times smaller than that of the axial channeling. A definition of the critical angle may be somewhat vague depending on the circumstances. If one uses different assumptions and potentials in his approach, then the critical angle may vary by a few percent. Using our crystals, (111) plane, and our beam energy of 375 GeV as an example, we have 9.03 μrad for the major plane by using equation (3.6) and 8.16 μrad (FWHM) by using Gemmel's approach [41]. They are of the same order of magnitude.

3.2.3 Dechanneling

Some particles are channeled when they enter crystals, but as they move along the channel, their transverse energy gradually increases which results in those particles escaping the channel. This phenomenon is called dechanneling.

There are many sources of dechanneling, the major source is multiple scattering because it changes the transverse momentum of the originally channeled particle.

There are other sources that are due to the change of the potential of the channel. This potential change can arise from the deviation from perfect crystal structure, dislocations as Hiroshi suggested [42], or some external mechanical function (the bending of the crystal).

The dechanneling caused by the bending process was described by Carrigan [43] and Gibson [44]. They used Tsyganov radius, R_T, to estimate the dechanneling factor.

$$R_T = \frac{E}{eE_c} \tag{3.8}$$

where E is the total energy of the particle and E_c is the interatomic field intensity at a distance from the atomic plane of the crystal lattice where the trajectory of the particle no longer remains stable due to its interaction with individual atoms. If a crystal is bent in a smaller radius than the Tsyganov radius, dechanneling will become a dominate factor. In our case, the eE_c is about 15 eV/$\AA$ which makes the R_T to be 250 cm. The average radius of our bent crystals is 2730 cm which is much larger than the R_T. This means dechanneling due to the bending is not dominant in our case.

The dechanneling is characterized by a parameter called dechanneling length, L_d. While dechanneling is a diffusion process, the dechanneling fraction can be approximated as

$$1 - e^{-\frac{L}{L_d}},$$

where L is the length of a crystal. In our experiment, the dechanneling length for silicon (111) plane is about 38 cm [9] and the crystals are 4.5 cm long, so that the dechanneling fraction is estimated to be 11 %. A simple way of estimation suggested by Carrigan [43] gives about 9 % dechanneling fraction due to the bending.

3.2.4 Energy Loss

The theory of the energy loss of an incident charged particle in a crystal is based on Bohr's [45] classic theory. He suggested two types of interaction between the projectile

and an atom initially at rest. One is an inelastic interaction which contributes a higher transfer of momentum because the impact parameter is very small and the electrons can be considered free under this type of interaction. The second type are due to distant collisions in which the interaction is limited to excitations of the outer electrons. The first type of interaction is stronger, but the second type happens more frequently, so the contributions from the two interactions are roughly the same. Since Bohr's solution has a problem when it predicts the energy loss at low and high energy, it has been modified and corrected by Bethe [46], Block [47] and Fanno [48] using quantum mechanics.

By solving the transport equation associated with the process, Landau [49] found the distribution function of the energy loss known as the Landau distribution. The long tail of the the distribution is a result of the small fraction of close collisions.

Since channeled particles avoid close collisions with atoms and are constrained to a relatively smaller spatial area in the transverse direction, their energy losses are smaller compared with those of nonchanneled particles. According to experiment, the energy loss of a channeled particle is about 60 % of that of a nonchanneled particle. Lindhard [50], Gemmel [41], Pines [51], Esbensen [52] and Ahlen [53] have discussed the energy loss reduction for channeled particles in their papers.

One can implant detectors on crystals to measure the numbers of ionized electron-hole pairs, thereby measuring the energy loss of the particle going through the crystal. This technique has proved to be a useful method for observing the channeling phenomena in high energy experiments.

3.3 Channeling in Bent Crystals

During the course of the first multihundred GeV particle study of channeling carried out at Fermilab in the mid seventies [54] by the Albany - Chalk River - Dubna - Fermilab group, Tsyganov [55] first suggested using channeling in elastically bent crystals for deflecting a charged particle beam. He introduced a centrifugal force into the particle motion equation

$$\frac{d^2x}{dz^2} + \frac{1}{2E}\frac{\partial V(x)}{\partial x} + \frac{1}{R} = 0, \tag{3.9}$$

where the R is the bending radius. This equation suggests a modification of the effective potential:

$$V^B(x) = V(x) + \frac{2E}{R}x. \tag{3.10}$$

For the harmonic potential approximation, V(x) = V_0x^2,

$$V^B(x) = V_0(x^2 + ux), \tag{3.11}$$

where u = $\frac{2E}{V_0R}$.

The centrifugal term introduces an asymmetry in the effective potential. Fig. 3.3 (taken from Kudo [40]) shows that the height of the outer potential well is lower while the height of the inner wall is higher compared to the potential of the unbent crystal. This would cause the equilibrium planar trajectory to move away from the midpoint of the planar channel (see Fig. 3.4). It is expected that some of the channeled particles would become dechanneled, but some would still follow the curved trajectory through the crystal. One can use a bent crystal to replace the conventional magnetic or electrostatic field to deflect high energy charged particles. This equivalent magnetic field can be as strong as 1000 Tesla depending on the energy of the incident particles and the crystal bending angle.

Although, in principle, negatively charged particles should also be channeled and deflected, they are strongly scattered in the crystal and are quickly dechanneled. So far, only positively charged channeled particles have been observed for planar bending.

3.4 Previous Experimental Results

The first experiment using bent crystals to deflect high energy beams was carried out at Dubna in 1979 [2]. The 8.4 GeV/c proton beam was deflected up to 26 mrad relative to the incident beam direction by planar channeling in a bent silicon crystal.

In the following year, at CERN, a 12 GeV/c proton beam was successfully deflected up to 52 mrad by both planar and axial channeling in a silicon crystal [3].

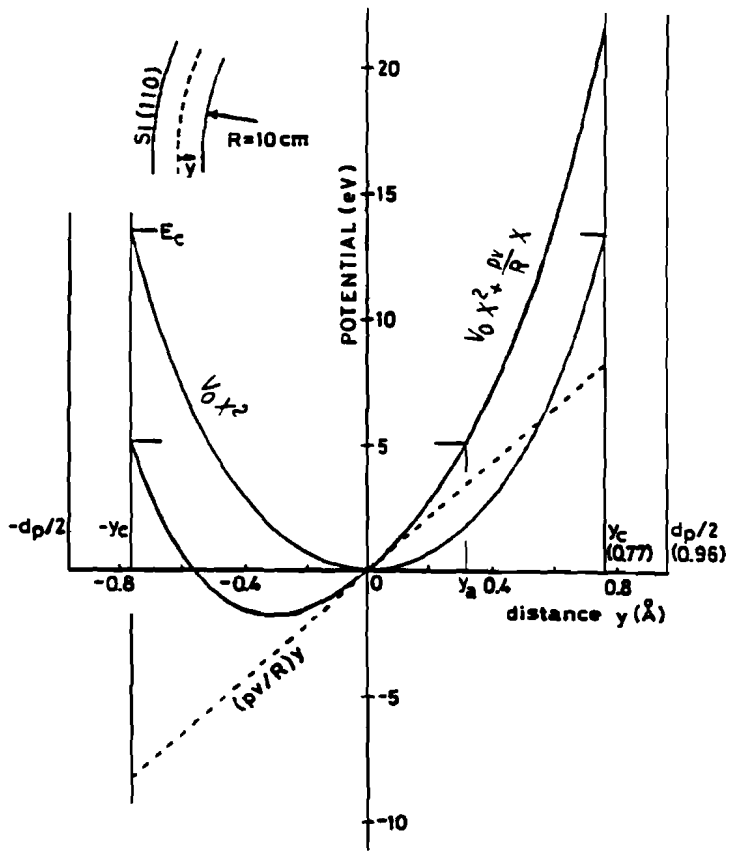

Figure 3.3: Modified continuum (110) planar potential of bent silicon for 10 GeV protons where x = 0 is in the central position between two adjacent planes. The bending radius is 10 cm.

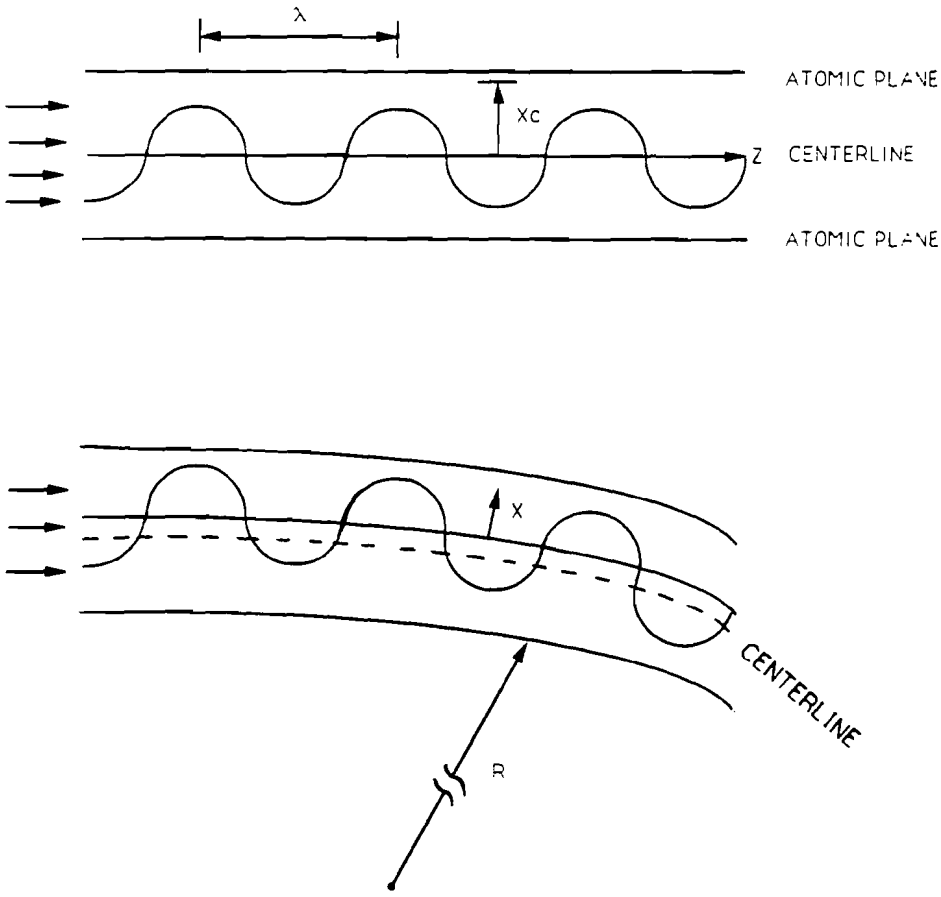

Figure 3.4: Schematics of channeled planar orbits in (a) an unbent and (b) bent crystal. The center of the orbit moves toward the outer plane in the bent case. λ is the wavelength of the particle motion.

At Fermilab, a series of experiments were conducted starting in 1982 by the Albany - Chalk River - Dubna - Fermilab group to test the properties of channeling in a bent crystal. In 1982, a high energy proton and π^+ beam with momentum ranging from 12 to 180 GeV/c [4] was deflected up to 28 mrad. Some of the channeling properties were also studied. Salman's Ph.D thesis [56] includes the first quantitative measurements of channeling in bent crystal. In 1984, a 225 GeV/c beam was bent 8.9 mrad as designed [5]. Wijayawardana's Ph.D dissertation [57] included a practical demonstration of the technique where a crystal was used to transmit the Fermilab primary beam (400 GeV/c) to the Meson Beam line in the full momentum while the conventional magnetic septum could only transmit the beam momentum up to 225 GeV/c. In 1986, the channeling of a 800 GeV/c proton beam in a bent crystal was observed [6]. Silicon crystals and planar channeling were used in these Fermilab experiments.

In 1990, at CERN, a 450 GeV/c proton beam was bent 7 mrad using planar channeling in a 5 cm long single crystal of silicon [7]. The bending dechanneling was also studied and found to be in agreement with calculations.

In 1991, a 70 GeV/c proton beam was sucessfully extracted to a secondary beam line by a Si crystal bent to 80 mrad at IHEP, Protvino, Russia [8].

3.5 Measuring the Magnetic Moment Using Channeling in Bent Crystals

In 1979, V. G. Baryshevsky [58] first discussed the possibility of relativistic particle spin rotation when it passes through a bent crystal in a channeling regime. V. L. Lyuboshits [59] then studied the relation of the spin rotation and the curvature of the trajectory of a relativistic charged particle moving through an effective field due to crystal channeling. L. Pondrom independently suggested using this spin rotation to measure the magnetic moment of short-lived charmed particles [60], and I. J. Kim treated the topic in more detail [39].

A particle channeled through a bent crystal is under the action of an electric field

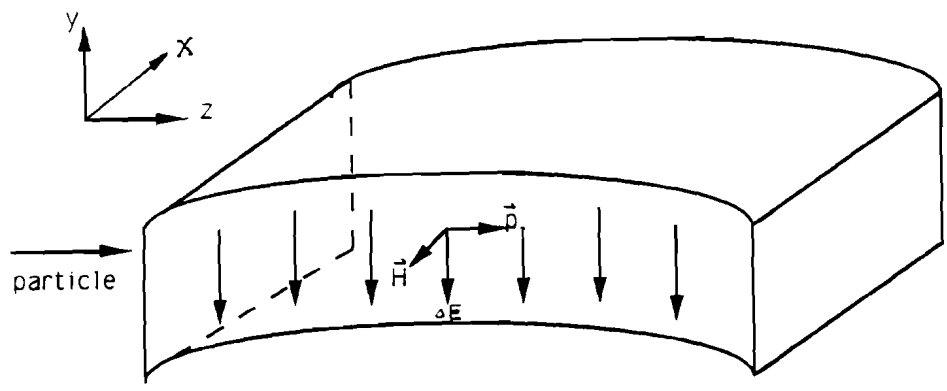

Figure 3.5: Electronic field and effective magnetic field for channeling particle in a bent crystal

of $\Delta\vec{E}$. The $\Delta\vec{E}$ averages about 10^9 v/cm along the period of its oscillator movement. Due to the Lorentz transformation there is an effective magnetic field, $\vec{H}$ (Fig. 3.5), for the particle in its own coordinate frame. This gives

$$\vec{H} \sim \Delta\vec{E} \times \vec{p}/m,$$

where $\vec{p}$ is the particle momentum and m is its mass.

The value of the magnetic field in the rest frame of the particle can be as high as hundreds of Tesla, depending on the particle's energy and the crystal bending angle. If the particle has a magnetic moment with a component perpendicular to $\vec{H}$, this moment will precess around $\vec{H}$ (Fig. 3.6) as shown in the equation

$$\frac{d\vec{S}}{dt} = g\mu\vec{S} \times \vec{H}, \tag{3.12}$$

where $\vec{S}$ is the spin, g is the gyromagnetic ratio, and μ is the magnetic moment of the particle. The same equation applies to the polarization vector, which is the statistical average of the spins.

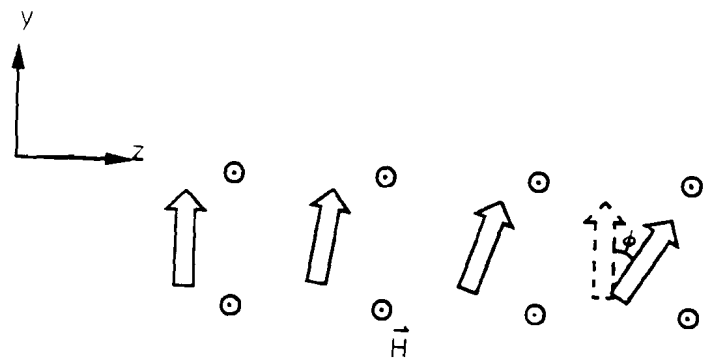

Figure 3.6: Polarization vector precession in the effective magnetic field. ϕ is the precession angle.

According to Lyuboshits [59], the rotation angle $\Delta\phi$ is

$$\Delta\phi = [\frac{1}{2}(g-2)\frac{\gamma^2-1}{\gamma} + \frac{\gamma-1}{\gamma}]\Delta\theta \tag{3.13}$$

where $\gamma = E/m_0c^2$ (the Lorentz factor), E is the particle total energy, $\Delta\theta$ is the angle between beam directions before and after the crystal (for channeling particles), m_0 is the particle rest mass, c is the speed of light, and g is the gyromagnetic ratio. For large γ, the equation 3.13 becomes

$$\Delta\phi \approx \frac{(g-2)}{2}\gamma\Delta\theta \tag{3.14}$$

For Λ_c^+ whose life-time is on the order of 10^{-13}s, the mean path for a 500 GeV beam in the laboratory frame is about 1.25 cm, which is too short to produce a measurable precession angle using a conventional magnet. A bent crystal, on the other hand, can provide a much stronger effective field in a very short distance, which has given the potential tool for measuring the magnetic moments of positively charged charm baryons, such as the Λ_c^+.

Before it is possible to consider a program of measuring the magnetic moment of short-lived heavy-flavor particles, it is useful to test the new technique on a well

studied particle, such as Σ^+, whose magnetic moment has been previously measured to be $2.42 \pm 0.05\ \mu_N$ using a conventional magnetic field. In our case, the momentum of Σ^+ is about 375 GeV/c and the crystal bending angle is about 1.6 mrad. Using equation(3.14), we expected the spin rotation angle $\Delta\phi$ to be 1 rad. Our experiment demonstrated the usefulness of the new technique.

Chapter 4

Apparatus

4.1 Introduction

A portion of the Fermilab 800 GeV/c primary proton beam from the Tevatron was transported to Proton Center with a spill duration of about 23 seconds per minute. This 800 GeV/c beam was then tuned and sent to our target to produce a secondary positive beam, including polarized Σ^+ hyperons. This chapter will briefly introduce the proton beamline, the target and the hyperon production channel. It will also describe the spectrometer used in this experiment, the crystals and the bending device, the trigger and data aquisition system, and finally, the data. There were two different geometrical configurations that were used for the E761 experiment. I will describe the configuration which was used by the channeling part of the experiment.

4.2 Proton Center Beam Line

Of the whole 890 meter long Proton Center beam line, The E761 experiment controlled the last part of it, the PC3 pre-target beam line. The beam tuning magnets in PC3 are shown in Fig. 4.1.

The three quadrupole magnets focused the 800 GeV/c proton beam onto our copper target. The beam spot size at the target was 0.5 mm horizontally and 1.0 mm vertically, which matched the size of our target (0.6 mm horizontally and 2.0 mm

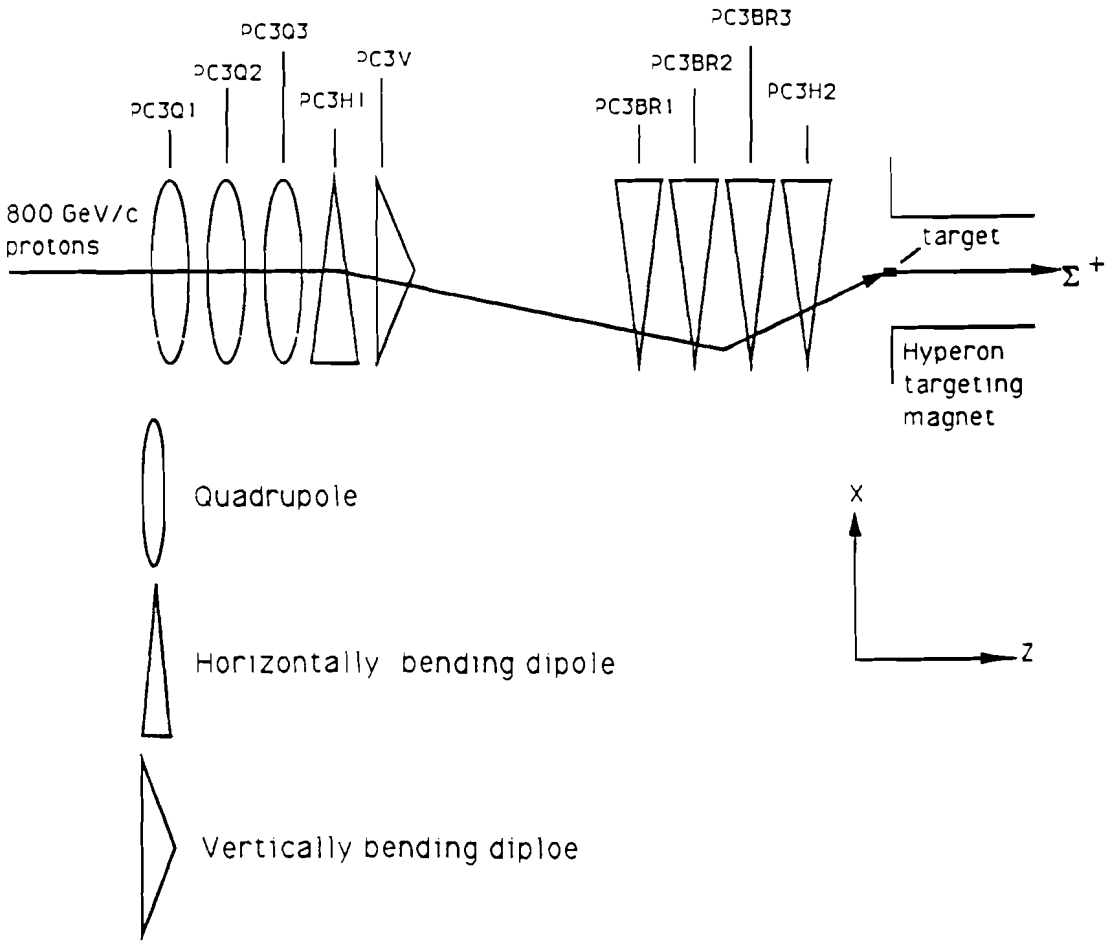

Figure 4.1: Schematic diagram (plan view) of PC3 beam line.

vertically). We used the dipole PC3H1 for bending the beam out horizontally in one direction, then used the four downstream dipoles PC3BR-1, PC3BR-2, PC3BR-3 and PC3H2 to bend the beam in the opposite direction back onto the target to produce a finite targeting angle. By reversing the polarities of these dipole magnets, we could change the direction of the targeting angle.

As we know, in the inclusive reaction

$$P(800GeV/c) + Cu \Rightarrow \Sigma^+ + anything,$$

the direction of the polarization of Σ^+ was determined by the direction of incoming proton and outgoing Σ^+ as

$$\hat{n} = \frac{\vec{k}_{proton} \times \vec{k}_{\Sigma^+}}{|\vec{k}_{proton} \times \vec{k}_{\Sigma^+}|}.$$

Reversing the targeting angle direction enabled us to change the sign of the polarization of Σ^+.

In our experiment, we defined our coordinate system such that the y axis pointed up, the z axis along the Σ^+ beam direction, and the x axis in a direction to form a right-handed coordinate system ($\hat{x} \times \hat{y} = \hat{z}$). The targeting angle shown in Fig. 4.1 was defined as a positive targeting angle which corresponded to the Σ^+ polarization in the -y direction. Our experiment used two opposite targeting angles, +4 mrad and -4 mrad, with error of $\pm$ 0.4 mrad. This gave us two sets of data with the Σ^+ polarization up and down so that we could cancel the apparatus biases. This will be discussed in chapter 8.

4.3 Target, Hyperon Magnet, and Hyperon Channel

4.3.1 Target

Our target was made of one interaction length Copper (see Fig. 4.2). It was 2 mm high in the vertical (y) and 0.6 mm wide in the horizontal (x) respectively. The small dimension in horizontal, production bend plane, would increase the momentum resolution by a factor of 2 if we required that the particles hit the target.

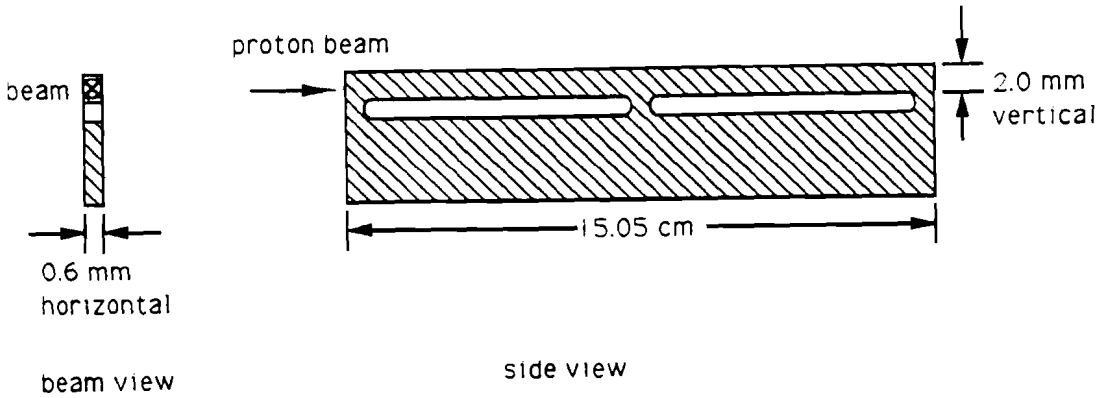

Figure 4.2: The copper target

4.3.2 Hyperon Magnet and Hyperon Channel

After the proton beam struck the target, the secondary beam was bent by the hyperon magnet and the hyperon beam was selected by a channel embedded inside the magnet. The hyperon magnet is a 7.31 meter long dipole magnet with a vertical field up to 3.5 Tesla.

The hyperon channel was made of blocks of the tungsten alloy, see Fig. 4.3 [62]. The curvature of the channel selected the hyperon momentum with a central momentum of about 375 GeV/c. The size of the beam at the exit was 0.9 cm (y) $\times$ 0.36 cm (x). It was estimated by Jastrzembski [63] from previous experiments that the secondary beam at a location 10 m downstream of the target contained 60% protons, 30% π^+, 6% K^+, 2% Σ^+, and other particles.

4.4 Spectrometer

The entire spectrometer of E761 is shown in Fig. 4.4. It includes four parts: the target with the hyperon magnet is at the upstream side, the hyperon spectrometer is located right after the hyperon channel, the crystal channeling device is located right

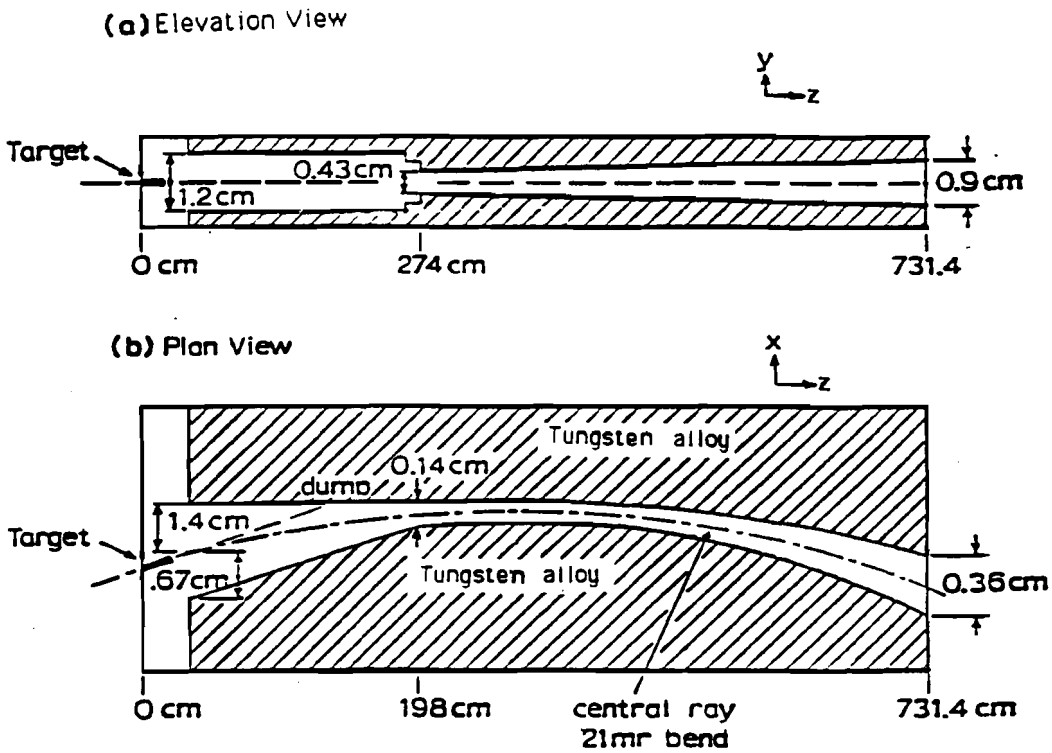

Figure 4.3: The hyperon magnet channel.

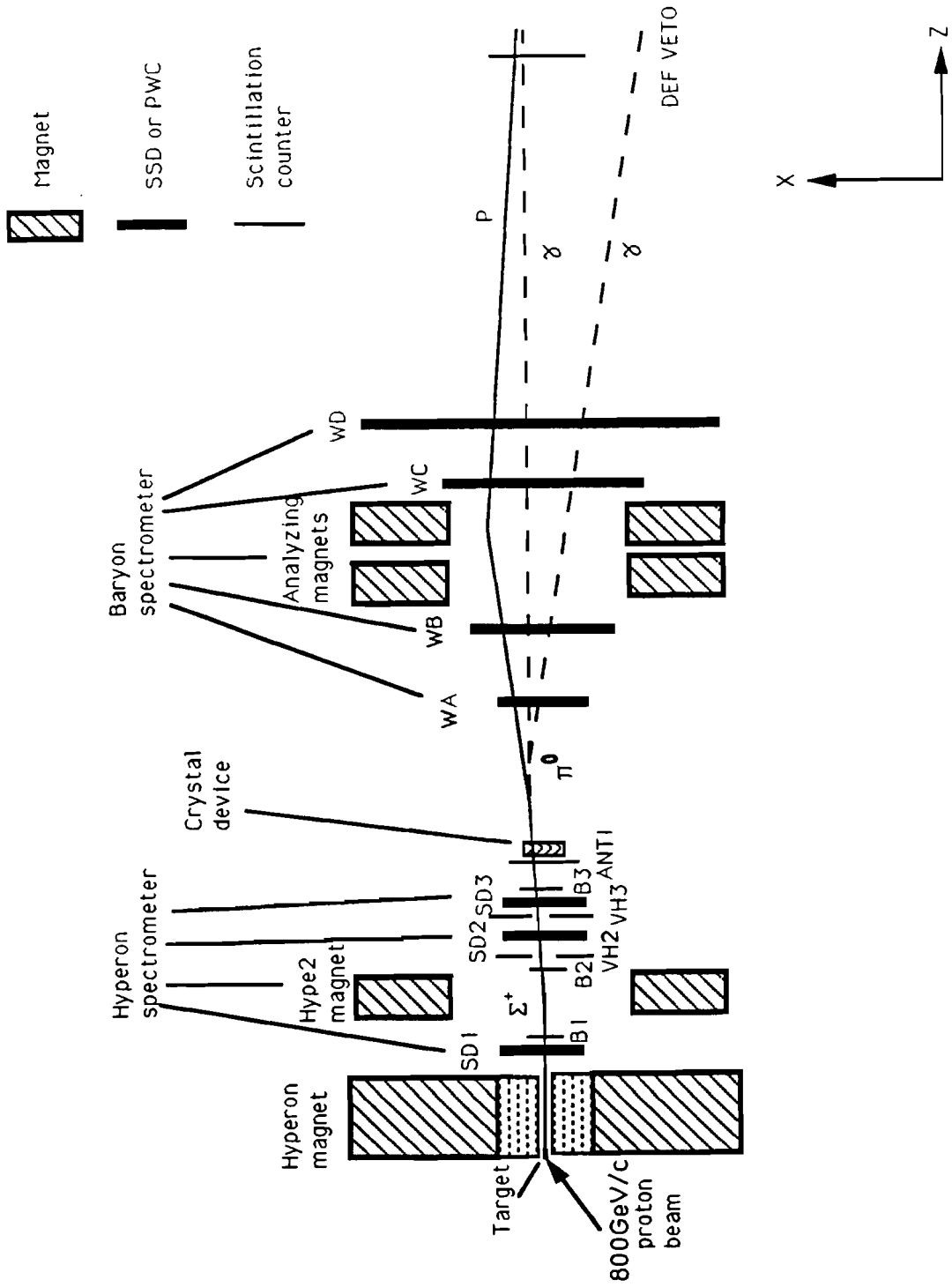

Figure 4.4: Schematic diagram of E761 spectrometer (not to scale). There are four main parts: target with hyperon magnet, hyperon spectrometer, baryon spectrometer and Crystals. The diagram also shows the decay of $\Sigma^+ \rightarrow p\pi^0$ with $\pi^0 \rightarrow \gamma\gamma$.

after the hyperon spectrometer, and the baryon spectrometer is at the end.

4.4.1 Hyperon Spectrometer

The hyperon spectrometer contained three stations of silicon strip detectors (SD1, SD2 and SD3) and one magnet (Hype2 Magnet) located between SD2 and SD3 with a p_t kick of 1.43 GeV/c. Each station was made up of three silicon detector planes: X, Y and U. The X plane had strips perpendicular to the x axis, the Y plane perpendicular to the y axis, and U plane had a 45^0 rotation with respect to X and Y. Each plane had an aperture of 5 cm $\times$ 5 cm, was 300 μm thick, and was spaced with a 50 μm pitch. The spectrometer measured the momentum of the secondary hyperon with a resolution (σ_p/p) of 0.7%. The spacial resolution was 10 μm and the angular resolution (σ) was 10 μrad which allowed us to measure the hyperon incident angle to the crystals very accurately.

4.4.2 Baryon Spectrometer

The baryon spectrometer contained four stations of proportional wire chambers (PWC) (WA, WB, WC and WD) and two analyzing magnets (A and B) located between WB and WC. WA was composed up of eight planes of proportional wire chamber: X, Y, X, Y, U, V, U and V, where X, Y, and U were defined as before and plane V was rotated 90^0 with respect to U. The aperture of the plane was 5 cm $\times$ 5 cm and the wire spacing was 1 mm. WB and WC also had eight chamber planes with wire spacing 1 mm, but WB's aperture was 10 cm $\times$ 10 cm and WC's was 20 cm $\times$ 20 cm. For WD, there were only six proportional wire chamber planes X, Y, X, Y, U, and V, with wire spacing 2 mm. Its aperture was 60 cm $\times$ 60 cm. All of the chambers used a standard magic gas mixture (75% argon, 25% isobutane with small amounts of freon). The p_t kick of the analyzing magnets was -1.64 GeV/c. The momentum resolution (σ_p/p) of the baryon spectrometer was 2.0%. The spacial resolution (σ) was 0.25 mm and the angular resolution (σ) was 10 μrad, which was good enough for us to measure the outgoing angle of the channeled particles from the crystals.

Table 4.1 gives information about the z location of the center of some important

apparatus	location Z(cm)	aperture X(cm) · Y(cm)	Pt kick (GeV/c)
SD1	99.0	5.0 × 5.0	
Hype2 Magnet	224.0	35.6 × 3.8	1.43
SD2	480.5	5.0 × 5.0	
SD3	648.6	5.0 × 5.0	
ANTI	734.4	10.0 × 10.0	
Crystals	767.8	2.5 × 0.04	
WA	2054.6	5.0 × 5.0	
WB	2872.7	10.0 × 10.0	
Magnet A	3072.7	61.0 × 20.3	-0.987
Magnet B	3305.5	61.0 × 20.3	-0.987
WC	3538.4	20.0 × 20.0	
WD	3838.4	60.0 × 60.0	
DEF VETO	6800.0	12.6 × 8.0	

Table 4.1: Location of the important apparatus. Z = 0 is at the exit of the hyperon magnet.

apparatus and their aperture. The scintillation counters ANTI and DEF VETO will be introduced in the later sections of the chapter.

4.5 Crystals and Bending Device

4.5.1 Crystals

Seven silicon crystals were produced and assembled at the Petersburg Nuclear Physics Institute, Russia. They were each 2.5 cm wide, 0.04 cm thick and 4.5 cm long, see Fig. 4.5. We numbered them # 1 to # 7 from bottom to the top. The crystals were cut along the (111) plane with the angular uncertainty within 300 μrad to the surface planes of the crystals [61].

4.5.2 Goniometer

All seven crystals were housed in a specially designed goniometer. The goniometer could rotate the crystal around the x axis in 2 μrad steps to align the crystals with the beam. We could also remotely adjust the x and y position of the goniometer as

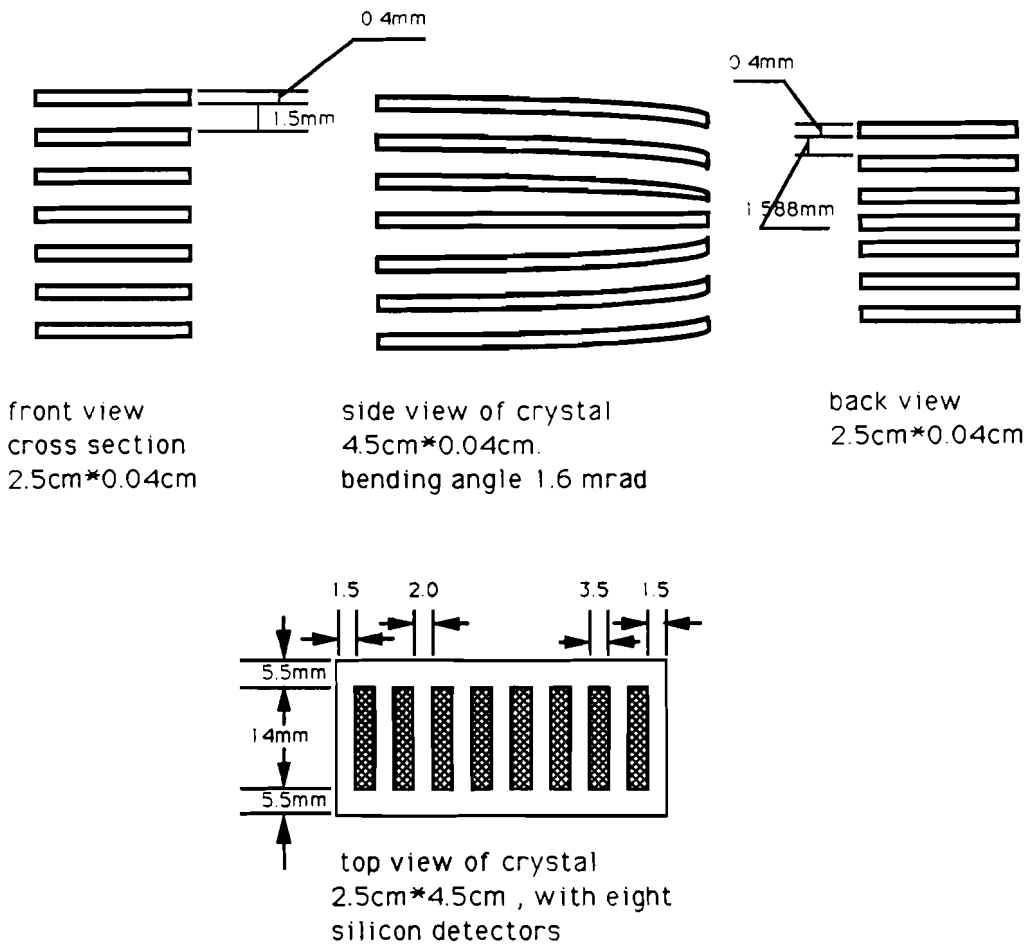

Figure 4.5: Seven crystals and their implanted silicon detectors on the surface of each crystal.

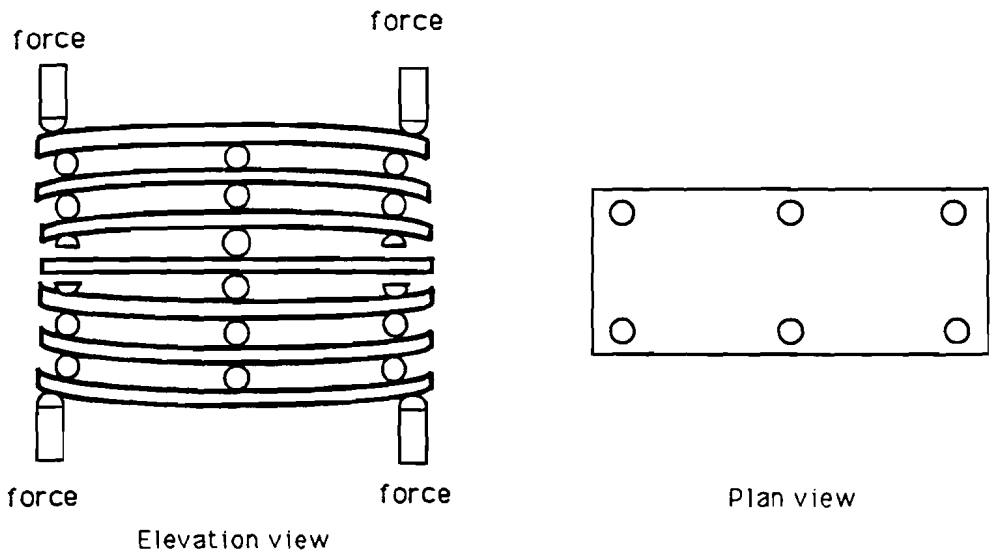

Figure 4.6: Crystal bending device.

well as the bending angle of the crystals.

To bend the crystal, pressure was applied to the four corners of the top and bottom crystal as shown in Fig. 4.6. There were ball bearing between each crystal on the four corner and in the middle of the side edges of the crystals. When pressure was applied, the upper three crystals were bent down, the lower three crystals were bent up, and the center crystal was not bent. The upper (lower) crystals deflected the beam down (up). The front bending and back bending could be adjusted separately. The front bending should be adjusted to match beam phase space. The back bending would decide the total bending angle.

After some initial testing, we found that only the five center crystals, from # 2 to

6, were inside the Σ^+ beam phase space in the y direction. Then, during the run, we were only able to align two of the five crystals, # 2 and # 5 with the beam. Our final data were the events from both the 5th crystal and the 2nd crystal. The crystal bending angle was limited by the aperture of downstream PWCs. The 5th crystal was bent down 1.6 mrad and the 2nd crystal was bent up 1.6 mrad.

4.5.3 Silicon Detectors on the Surface of Crystals

There were eight implanted sensitive strips (p-n junction) on the surface of every crystal as shown in Fig. 4.5. Notice that only the center 1.4 cm region of the crystals in the x direction were covered by the implanted detectors. Therefore, we only considered the center 1.4 cm part of the crystals as the active and useful part in the x direction. The crystals with the detectors allowed us to "mark" all the particles passing through the crystals and to measure their ionization losses. A particle which passed through a crystal in the channeling regime would usually have a smaller value of ionization loss compared with a particle passing through a crystal without channeling. Fig. 4.7 illustrates the analytical energy loss spectrum for a 350 GeV/c positively charged particle. It shows that the energy loss of the channeling particles is about 60% of that of the nonchanneled particles.

Fig. 4.8 shows the block diagram of how we received the energy loss signal from a detector on a crystal. The signal after the preamplifier was on average about -30 mV with rise time 300 ns. The signal went through a signal line driver and then was sent to our control room. The signal was amplified again to about -300 mV and was sent to CAMAC charge ADC (Analog to Digital Converters) module 2249A.

4.6 Crystal Channeling Trigger

Our crystal channeling trigger consisted of two sections: a beam trigger and a channeling trigger.

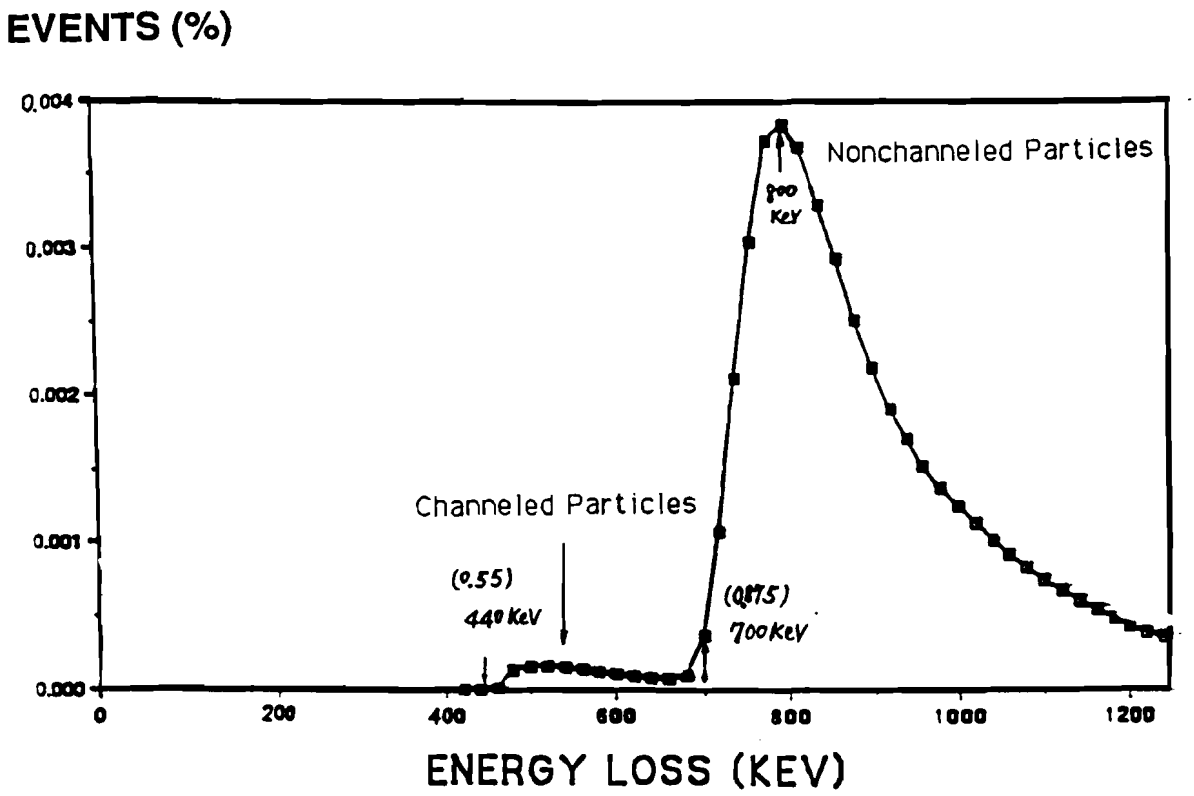

Figure 4.7: Analytical calculation of the ionization losses. Small energy losses corresponds to channeling particles, and normal Landau energy loss distribution corresponds to nonchanneled particles.

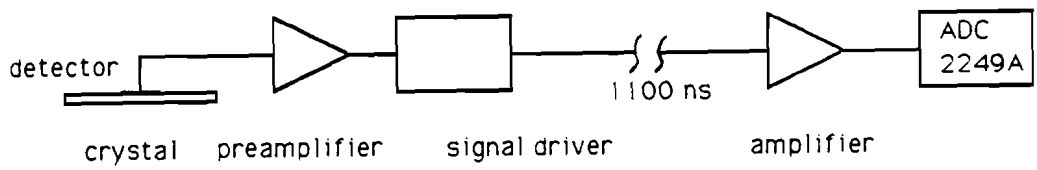

Figure 4.8: Schematic of the energy loss signal being sent to ADC.

4.6.1 Beam Trigger

The beam trigger, also called level one trigger T1, required coincident hits in the upstream scintillation counters B1, B2, B3 and no hits in the halo counters, VH2 and VH3. The cross section of our two crystals was only a small fraction of the total beam size. An additional scintillation veto counter, ANTI, was inserted in front of the crystals to reduce the beam rate and thereby the data collection rate was increased. The ANTI counter aperture was 4 in × 4 in. There were two holes in it with the approximate size to match the useful cross sections (1.4 cm × 0.04 cm) of the two crystals (see Fig. 4.9). It rejected the particles which did not hit the two useful crystals. The ANTI counter was also used to cut off that fraction of the beam which hit the side edges of the crystals. Those parts of the crystals would not give a proper ionization signal. The beam trigger can then be defined as:

$$\mathrm{T1} = \mathrm{B1} \cdot \mathrm{B2} \cdot \mathrm{B3} \cdot \overline{VH2 + VH3 + ANTI}.$$

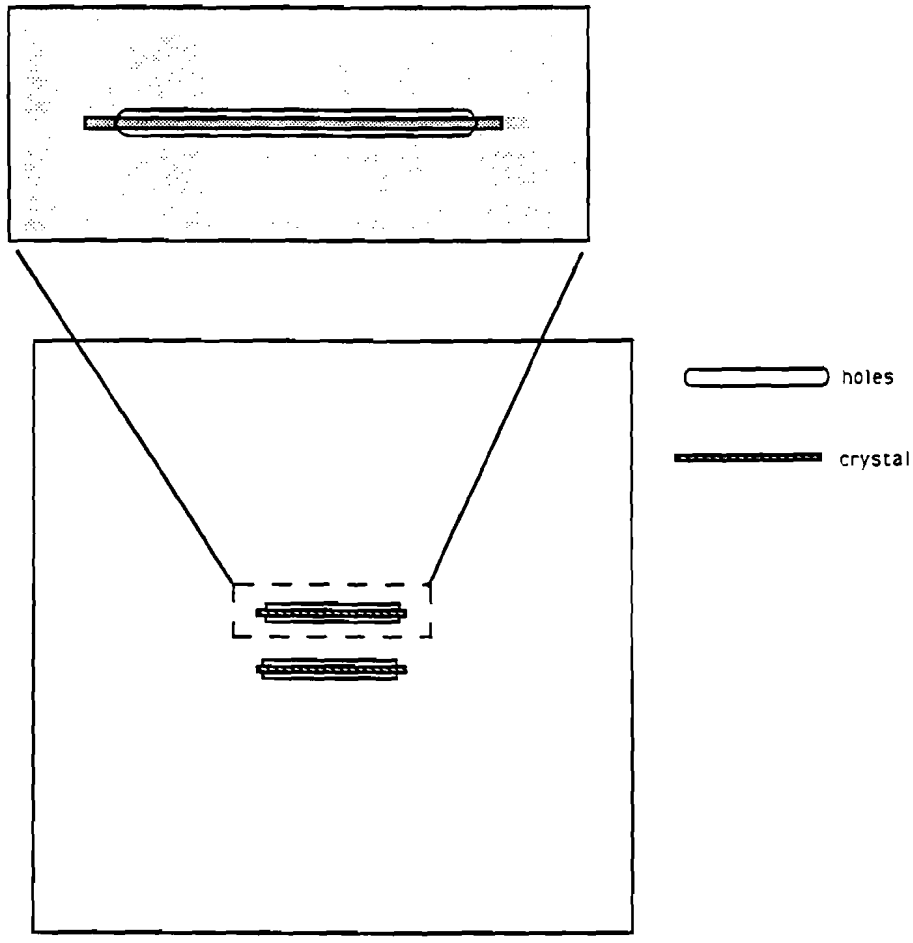

View from beam.
Anti countor: 4"* 4";
Hole: 1.2cm * 0.05cm.
Crystal: 1.4cm * 0.04 cm.

Figure 4.9: Anti counter with the crystals

4.6.2 Channeling Trigger

The schematic drawing of our channeling trigger, level three trigger T3, is shown in Fig. 4.10. To make sure that a particle entered the crystals, we required a signal from the first detector (XTAL) on the surface of the crystals to have a threshold just above the electronic noise level, 30 mV. Since we had an ANTI counter, those events which had a signal caused by a δ ray emitted from the other neighboring crystals were not able to pass the trigger.

Another scintillation counter was used downstream of the baryon spectrometer, called a deflection veto counter (DEF VETO). This counter was designed to cut off all the straight-through, undeflected, and presumably nonchanneled particles. Due to the beam divergence, the nonchanneled beam had a spot size at the DEF VETO of 5 cm in y. Channeling particles would have spots centered at $\pm$ 16 cm. The proton from the decay of channeled Σ^+ could have a decay angle up to 0.65 mrad (see the shaded area in Fig. 4.10). This veto counter had a size of 8 cm in the y direction. The counter with the small size could not cut off all the nonchanneled events especially those decayed particles and interaction particles from the nonchanneled beam. The point of making a smaller deflection veto counter was to not cut off any channeling particles.

Our final crystal channeling trigger was:
$T3 = T1 \cdot \mathrm{XTAL} \cdot \overline{DEFVETO}$.

4.7 Data Acquisition

When an event satisfied the trigger, a signal was sent to three Fermilab Smart Crate Controller (SCC) [64] modules in three CAMAC crates, see Fig. 4.11. The SCC then sent all the data signals to a buffer memory RBUF [65] in a VME crate. The apparatus included 10,500 channels of SSD and PWC read out through Russian-designed modules called RMLs, 150 ADC and Time to Digital Converters(TDC) channels and about 100 channels of scalers. Through the RBUF, the data were sent to one of 14 Advanced Computer Project (ACP) [66] nodes which ran the offline event reconstruction program online. The ACP could handle about 10% of our data online.

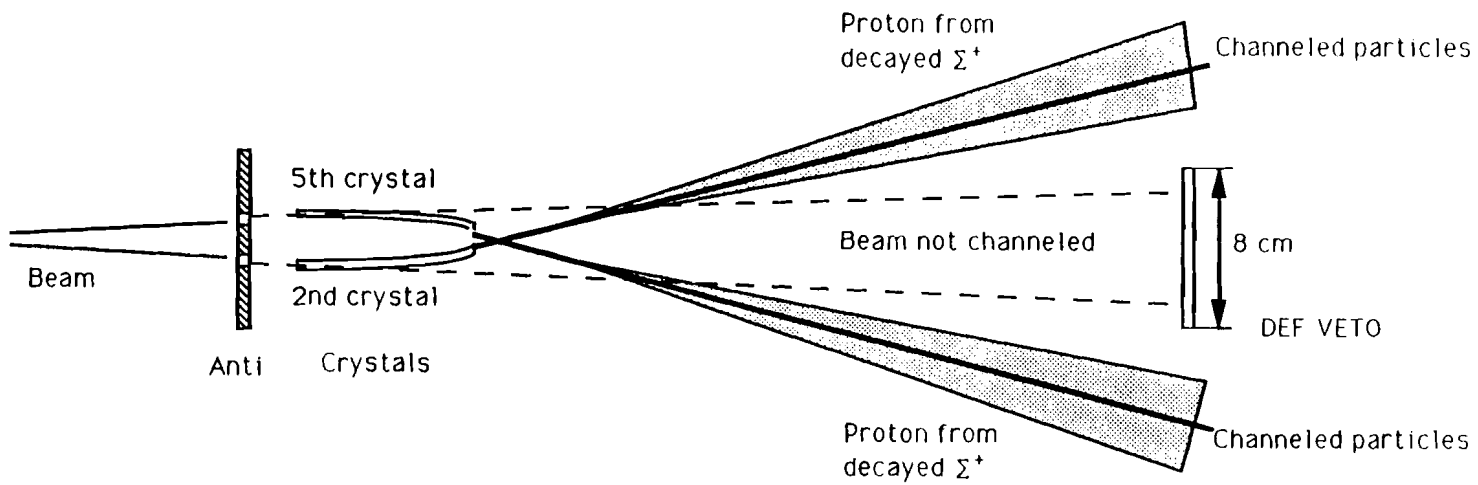

Figure 4.10: Channeling trigger schematic diagram.

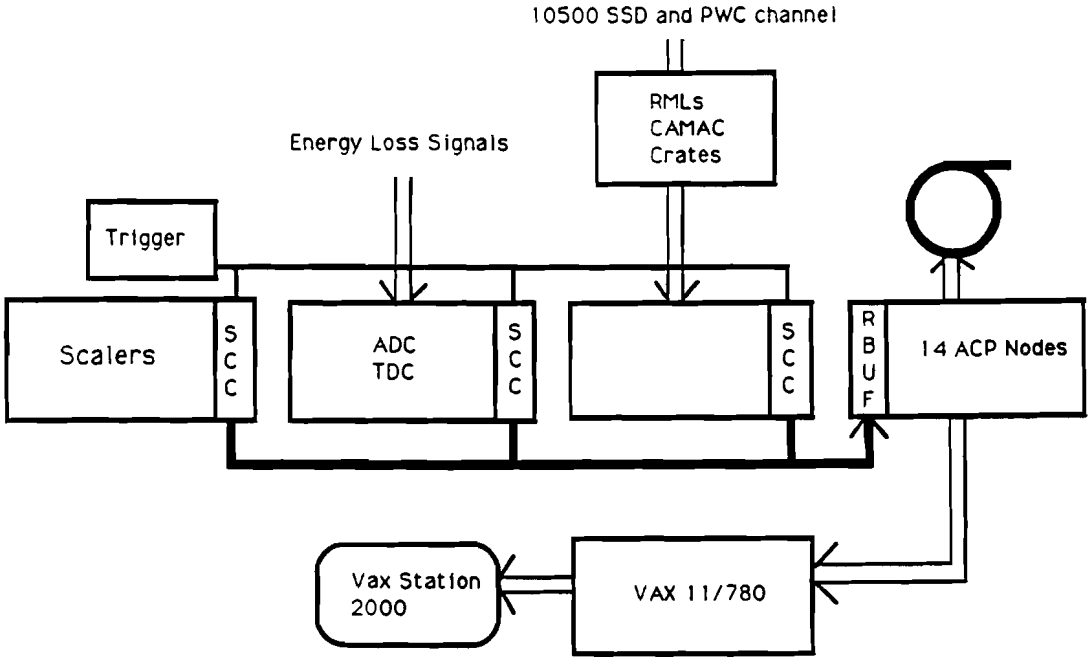

Figure 4.11: Data aquisition schematic diagram.

The data were sent to a VAX 11/780 and a VAX station 2000. These online events were very useful to monitor the data taking process and treat problems as soon as they occurred. Each event was about 400 bytes long and took 400 μs to read out. We read 10,000 events per spill with 50 % dead time. All the data were finally written to 6250 bpi 9-track tapes.

4.8 Rate and Tape

The proton rate was variable from 3 $\times 10^{11}$/spill to 8 $\times 10^{11}$/spill, controlled by the operation center. Our trigger rate was about 6 % of our beam trigger. The average events per spill we took was about 10,000. We took two continuous runs at one incident beam angle in horizontal plane, +4 mrad, and then two runs at opposite angle, -4 mrad.

Our three phases of data were taken at three different time periods between other parts of the experiment. We had to move our crystal device out of the beam when we were not taking data, and moved it back into the beam when we took data. The vertical position of the crystals differed about 0.1 mm for these three phases. Table 4.2 shows all the data we had with the run number, numbers of tapes, targeting angle and number of events. We collected a total of 26.6 million events for our crystal channeling experiment. During the third phase of data taking, run 4256 was interrupted due to a controlled access into the experimental area, and the crystals were moved down during this time. After the access, the crystals were moved back into position and run 4259 was started. Since the y position of run 4259 was not very stable at the beginning, we treat it separately from rest of the runs of phase 3. During the phase 3 series of runs, we removed some unnecessary informations from our data structure. This information was from some parts of the detectors which were only used for other parts of the experiment, such as the energy deposited in the lead glass. By doing that, we reduced the size of the data structure and data taking time, and therefore increased data taking rate and rate of events per tape.

	run #	targeting angle (mrad)	# of tapes	# of spills	# of events
phase 1	run 3948	+ 3	3	59	501744
	run 3949	+ 3	3	61	532151
	run 3950	- 5	3	83	520416
	run 3951	- 5	3	84	516624
	run 3949	+ 3	3	63	504632
	run 3951	- 5	3	95	515222
phase 2	run 3997	+ 3	3	80	622851
	run 3998	+ 3	3	72	603034
	run 3999	- 5	3	179	600862
	run 4000	- 5	3	137	578560
	run 4001	+ 3	3	81	623214
	run 4002	+ 3	3	77	597812
	run 4003	- 5	3	119	595662
	run 4004	- 5	3	142	579781
	run 4005	+ 3	3	101	633183
	run 4006	- 5	3	128	581351
phase 3	run 4256	+ 3	3	117	1279611
	run 4259	- 5	3	312	1221441
	run 4260	- 5	3	230	1269126
	run 4261	+ 3	3	128	1222366
	run 4262	+ 3	3	133	1279771
	run 4263	- 5	3	232	1226861
	run 4264	- 5	3	353	1273193
	run 4265	+ 3	3	203	1243477
	run 4266	+ 3	3	118	1262560
	run 4267	- 5	3	228	1234184
	run 4268	- 5	3	220	1260105
	run 4269	+ 3	3	171	1222438
	run 4270	+ 3	3	265	1292394
	run 4271	- 5	3	392	1251330
total	30 runs		90	4663	26645959

Table 4.2: Summary of the runs, tapes, and events.

Chapter 5

Alignment of Crystals

The key procedure of the channeling experiment is to align the crystal (111) plane with the Σ^+ beam so that channeling will occur. In this chapter, the motion calibrations are described; the concept of the online alignment is introduced; some problems with our crystals are discussed; and the offline alignment to overcome the problems is described.

5.1 Motion Calibrations

Our crystals were raised into the beam when we were doing the channeling experiment and were lowered out of the beam while other parts of the E761 experiment were running. We used two linear motion motors to move the crystals in both x and y directions. Fig. 5.1 shows the outline of the linear motions that carried the ANTI counter. Two UniSlide motor driven assemblies (Model B4015P10J) with adapter plates, one for the x direction and one for y, were used. The range of the movements were both 12 cm. The motors were controlled by Fermilab-made "044M" CAMAC control modules through an interface box. We could control the motors remotely by the Fermilab beamline control system EPICURE. Fig. 5.2 shows a schematic of the motion control system for both linear motions and goniometer. We calibrated the linear motion controller to 0.05 mm accuracy.

The stepping motor of the goniometer, which rotates the crystals, was controlled

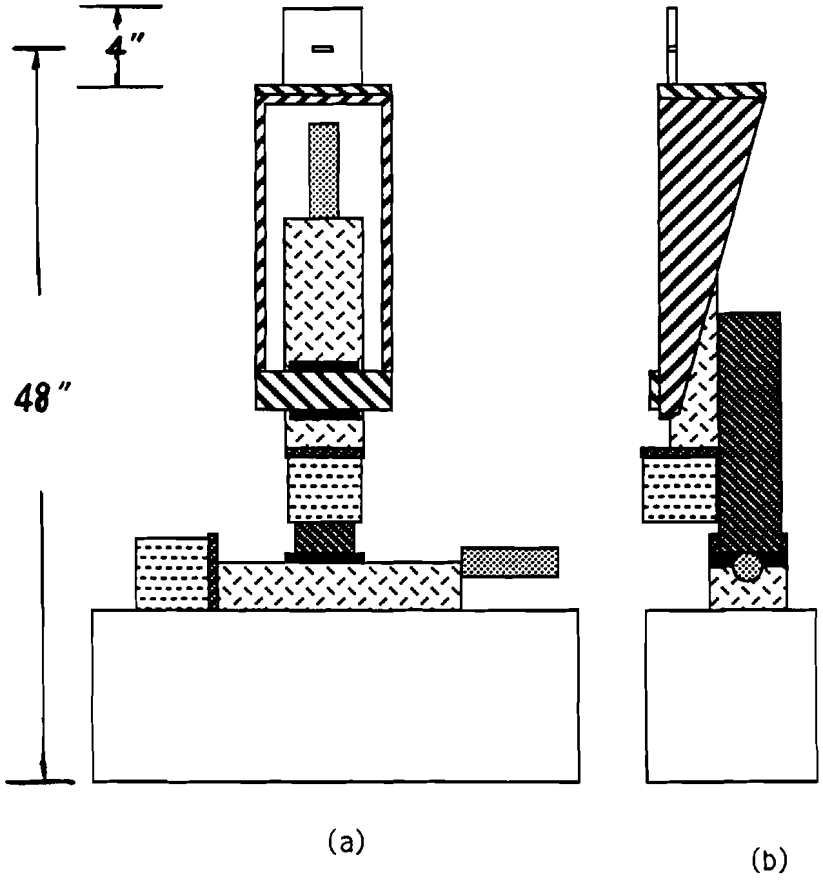

Figure 5.1: The linear motion motors with the ANTI counter on the top: (a) front view, (b) side view.

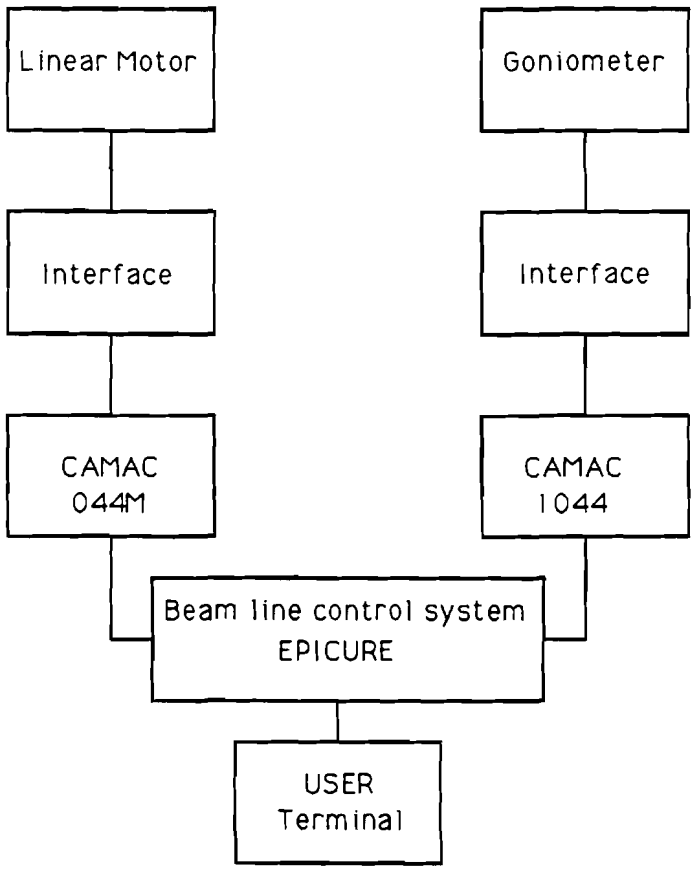

Figure 5.2: Schematic of the motion control system for both linear motions and goniometer.

by a Fermilab-made motion controller [67]. The motion controller could be controlled remotely by a Fermilad-made CAMAC interface module "1044 Module" through the EPICURE. We calibrated the goniometer by letting it go through a large number of steps and recording the turning angle. We calibrated the goniometer to 1.88 $\pm$ 0.02 μrad per step. This allowed us to make a precise scan through a $\pm$10 μrad channeling critical angle with a beam angular divergency of about 100 μrad for an individual crystal.

5.2 Online Alignment

As we mentioned in the previous chapter, the energy loss responses for channeled and nonchanneled particles from the detectors implanted on the crystals were different. The channeling particles lose less energy in the crystals and therefore make up the small energy loss spectrum on the low energy side of the Landau peak, which is due to the nonchanneled particles. The standard method used in past experiments to align crystals was to measure the energy loss. The ratio of the number of events in the smaller energy loss area over the number of events in the normal Landau area were monitored online while the crystals were scanned. When the crystal plane was found, the ratio should have a maximum value. Fig. 5.3 [56] shows a typical channeling online scan plot obtained in a previous channeling experiment. The peak in the plot demonstrates that channeling occurred when the scanning angle was at about 0.9 mrad.

We started to align the crystals using this same standard procedure. However, a large fraction of the events had an energy loss on the low energy loss side of the spectrum. Fig. 5.4 (a) shows the energy loss spectrum from a scanning run at the channeling position. The energy loss was normalized to the Landau peak value. We knew many of these events were not channeling events but nonchanneled background because they appeared at the scanning angles. This background contaminated the real channeling small energy loss region. From the two dimensional plot of the height in the crystal (y) versus the energy loss, shown in Fig. 5.4 (b), we see that the energy loss from the high y (top side) part of the crystal is normal as we expected. On the

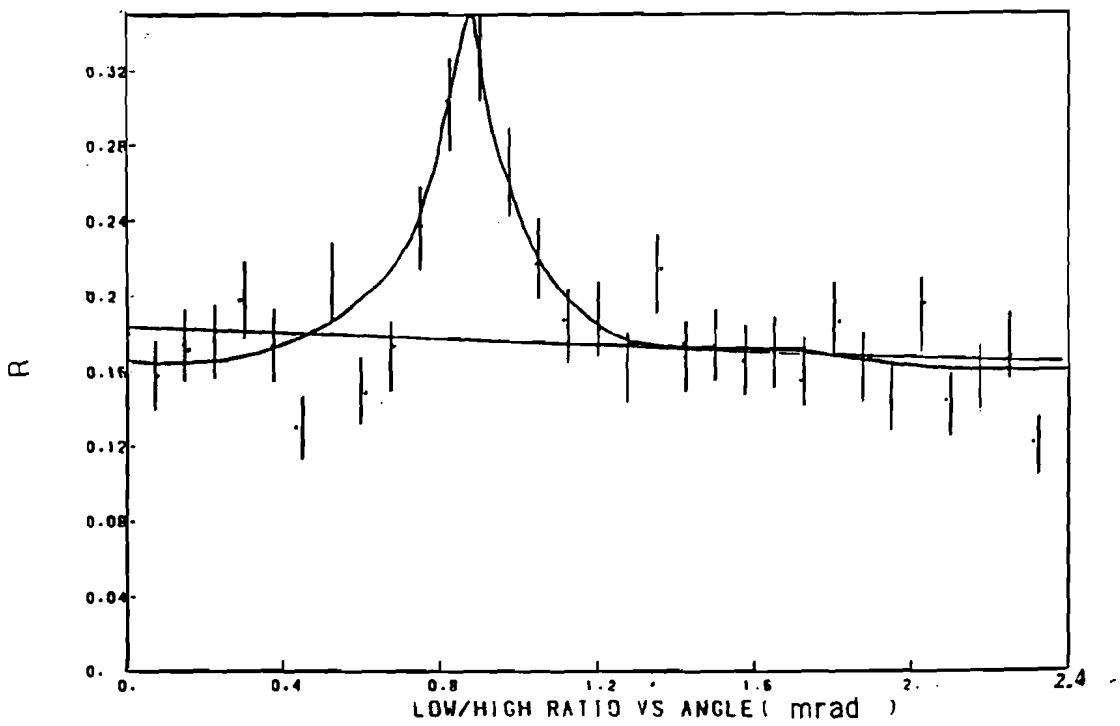

Figure 5.3: Channeling scanning plot from a previous experiment. The x axis is the scanning angle and the y axis is the ratio of events in the smaller energy loss area over the number of events in the higher energy loss area.

low y (bottom side) part of the crystal, however, the energy loss decreased to zero. Since there were many more background events than real channeling events (when the channeling occurred) in the lower energy area, the ratio of the lower energy loss events over the high energy loss events was not sensitive to the channeling. Therefore, we could not use this standard method to align the crystal online.

5.3 Electronic Problem with the Crystals

The distortion of the energy loss spectrum is due to the incomplete depletion of the lower part of the crystal. The cause of the problem has been carefully investigated since the experiment by our Russian colleagues in St. Petersburg. They repeated all the procedures of fabricating the Si detectors on a silicon wafer. They closely monitored the material resistivity after each stage of the process.

According to our Russian colleagues [61], there were six significant stages of treatment:

(1) Starting materials;

(2) Thermal oxidation at 1000^0C in wet oxygen with Cl doping;

(3) Thermal oxidation at 1150^0C in dry oxygen with Cl doping;

(4) Thermal boron diffusion at 1150^0C in a mixture of oxygen and nitrogen;

(5) Annealing in a hydrogen atmosphere at 900^0C for 5 minutes;

(6) Annealing in a hydrogen atmosphere at 450^0C for 30 minutes.

They observed that a significant decrease in material resistivity took place after the 5th stage because a new electrically-active center emerged with concentration exceeding the main impurity concentration by several times. Because atomic hydrogen cannot produce any kind of deep levels in Si, and because none of the known impurities besides hydrogen can penetrate Si to a depth of 150 - 200 μm in a 5 minute anneal at 900^0C, it is suggested that the concentration is formed as a complex of hydrogen and an electrically inactive impurity contained in the starting material.

The reduction of the resistivity is the reason for the incomplete depletion layer. We tried to solve the problem during the run by increasing the bias voltage on the detector from the designed 100 V up to 180 V. It did increase the output signal by a

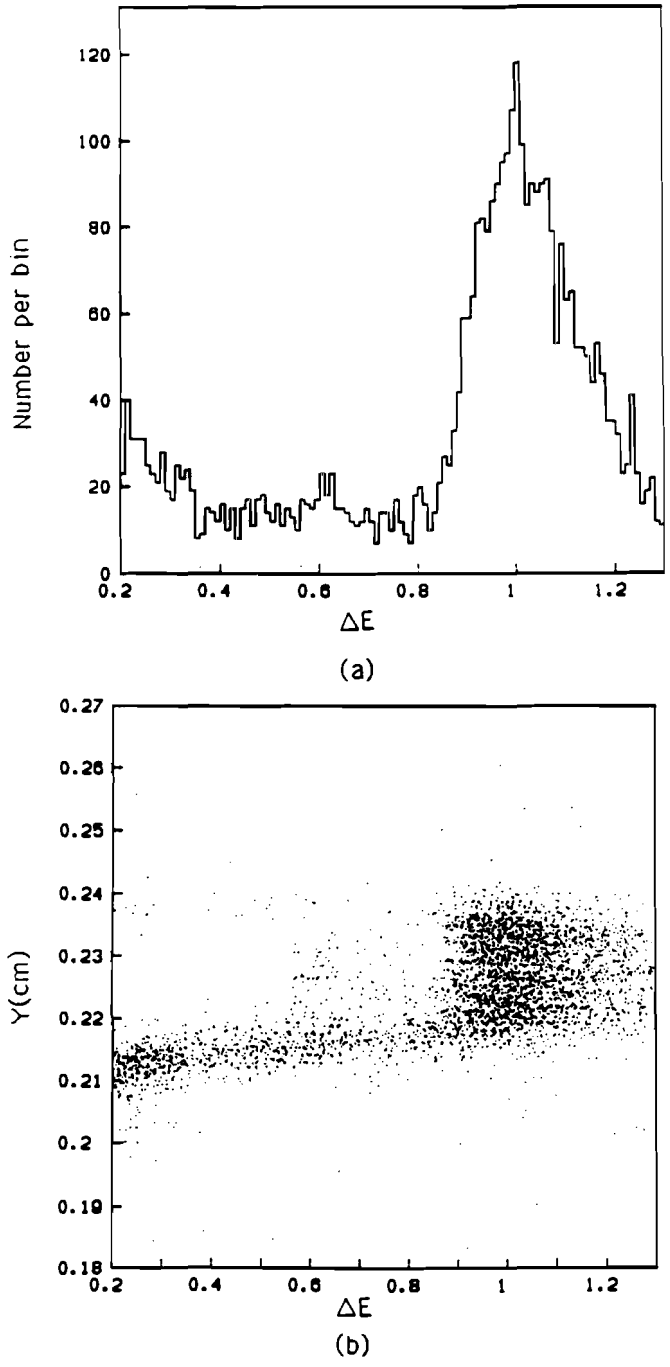

Figure 5.4: (a) Normalized energy loss, ΔE, spectrum of a scanning run at the channeling position. (b) The height in the crystal Y (cm) versus normalized energy loss ΔE.

small value, but it did not solve the problem.

5.4 Offline Alignment

To solve the problem of the partially nondepleted crystals, we decided to use the energy loss signal only from the good, depleted, part of the crystals. Since we could not separate the particles in the good part of the crystals from those in the imperfect part online, we had to use our data acquisition and offline system to align the crystals.

When we scanned the crystals, we rotated the crystals in 54 μrad steps. This step size was smaller than the beam divergence of 100 μrad. On the other hand, we could go through a large range of angles in a relatively short time because of the not very small step size. We recorded two spills of data, about 50,000 events, on magnetic tape for every goniometer step. The data we recorded contained all the energy loss and spatial information for the events. Through the offline program, we calculated the y position of each beam particle at the front of the crystals and removed events with y in the imperfect area. The energy loss spectra of several scanning runs after the offline y cut are shown in Fig. 5.5. Fig. 5.5 (a) is for the goniometer at 700 μrad from the channeling position, (b) is for the goniometer at 320 μrad from the channeling position, (c) is for the goniometer at 19 μrad from the channeling position, and (d) is for the goniometer at the channeling position. We then applied the standard alignment technique to the good part of the crystals. Fig. 5.7 shows the scanning plot of our offline alignment for the 5th crystal. The peak shows that channeling occurred. The width of the peak corresponds to the convolution of the beam divergence over the crystal critical angle, and the resolution of the system. The FWHM of the peak is about 180 μrad, which is wider than we expected. This is due to the tilt of the channeling plane in the x direction, as I will explain it in Chapter 7. The background of the peak is due to the contamination from of those events which went through the nondepleted part of the crystals. To confirm the channeling, we also checked the beam deflection downstream of the crystals. Fig. 5.6 shows the beam angle deflection in the y direction in a logarithmic plot. Fig. 5.6 (a) is for the goniometer at 700 μrad from the channeling position, (b) is for the goniometer at

320 μrad from the channeling position, (c) is for the goniometer at 19 μrad from the channeling position, and (d) is for the goniometer at the channeling position. The center peak consists of nonchanneled events, and the peak at −1.6 mrad in Fig. 5.6 (c) and (d) is a clear evidence for channeling. This beam deflection technique, called the "Kim technique", was also used as an alignment technique in previous channeling experiments. To use this technique, one has to know the bending angle of the crystal very well. We used this technique as a double check. To align the 5th crystal more accurately we then used smaller steps of the goniometer, and did a finer scan around the peak. The 5th crystal was successfully aligned.

Aligning other crystals turned out to be more difficult. Because the goniometer and the bending device controlled all of the crystals at once, we were not able to align the crystals individually. We tried adjusting the force at the front bending points to change the relative orientations of the planes of the different crystals. After several attempts we aligned another crystal, the 2nd crystal, with the beam and did not destroy the alignment of the 5th crystal. Time constraints prevented us from aligning other crystal, only the 2nd and 5th crystals were finally aligned.

After the two crystals were aligned, we made the ANTI counter with two holes. The y aperture of the holes was 0.05 cm which would cover the whole thickness of the crystal. We did not try to use the ANTI counter to cut off the events from the imperfect part of y . After adjusting the position of the ANTI counter to let the holes cover the 5th and 2nd crystals, we started to take data.

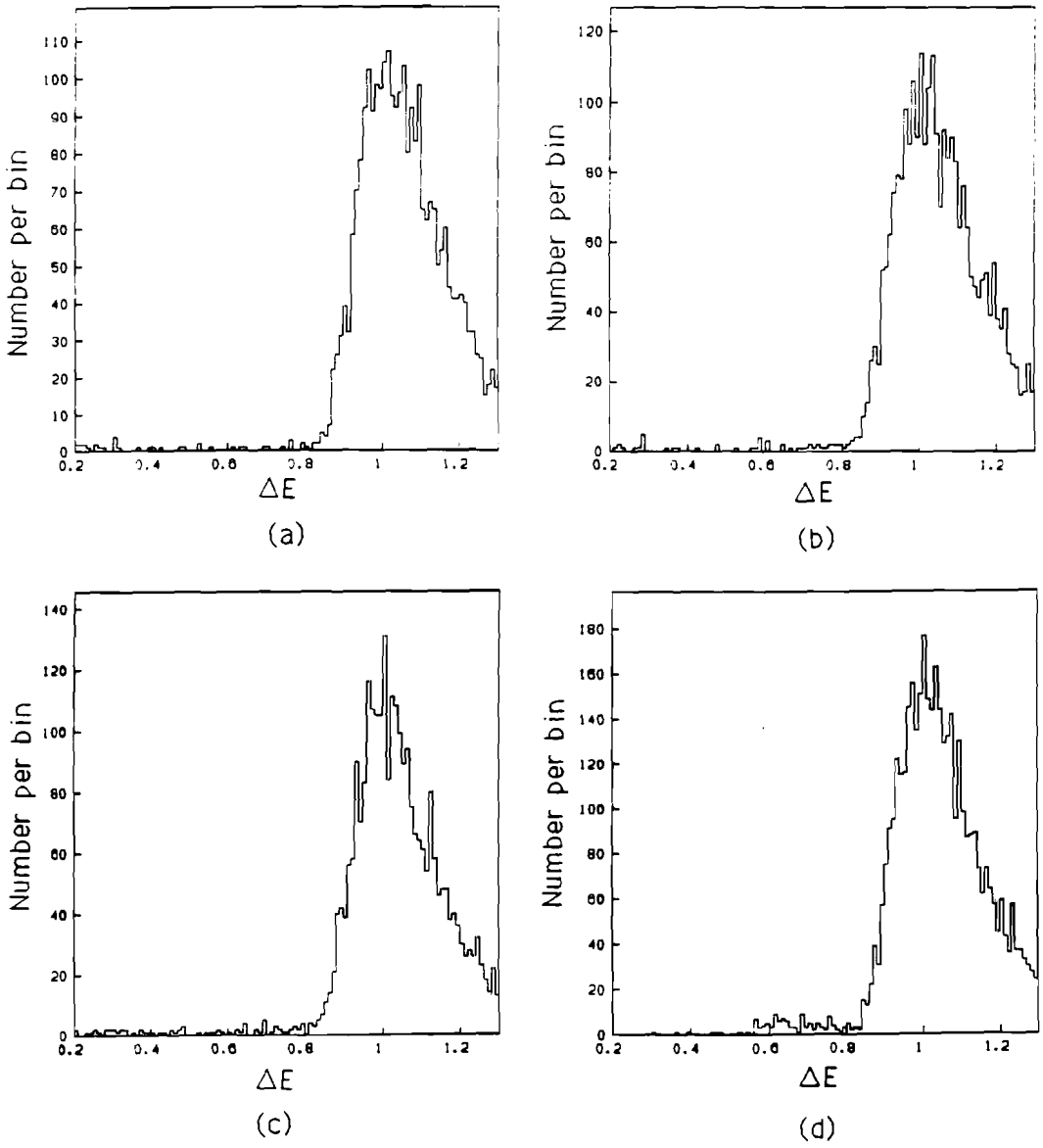

Figure 5.5: Normalized energy loss spectrum of several scanning runs after offline y cut: (a) goniometer at 700 μrad from the channeling position, (b) goniometer at 320 μrad from the channeling position, (c) goniometer at 19 μrad from the channeling position, and (d) goniometer at the channeling position.

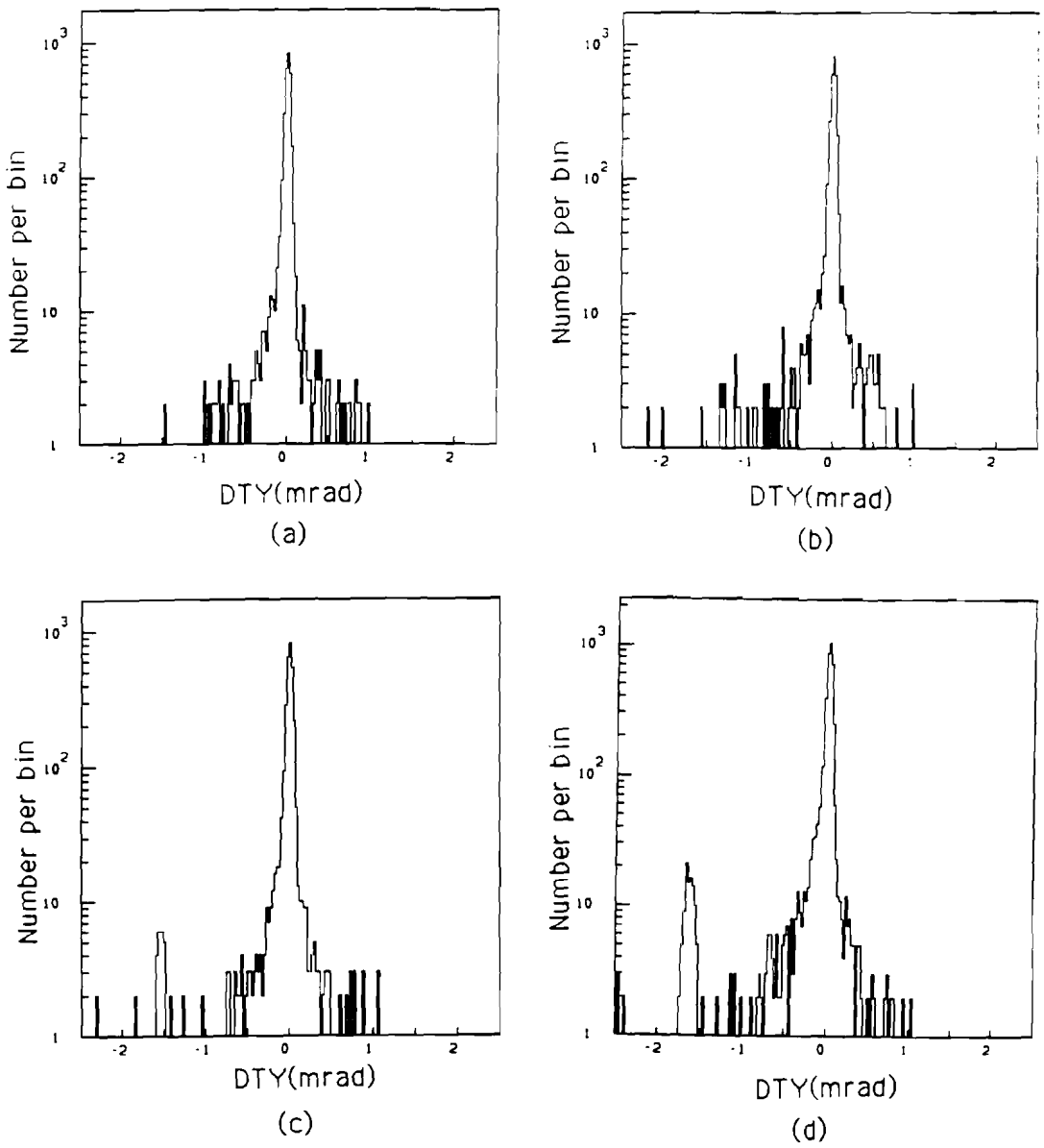

Figure 5.6: Particle deflection angle distribution in the y direction for (a) goniometer at 700 μrad from the channeling position, (b) goniometer at 320 μrad from the channeling position, (c) goniometer at 19 μrad from the channeling position, and (d) goniometer at the channeling position.

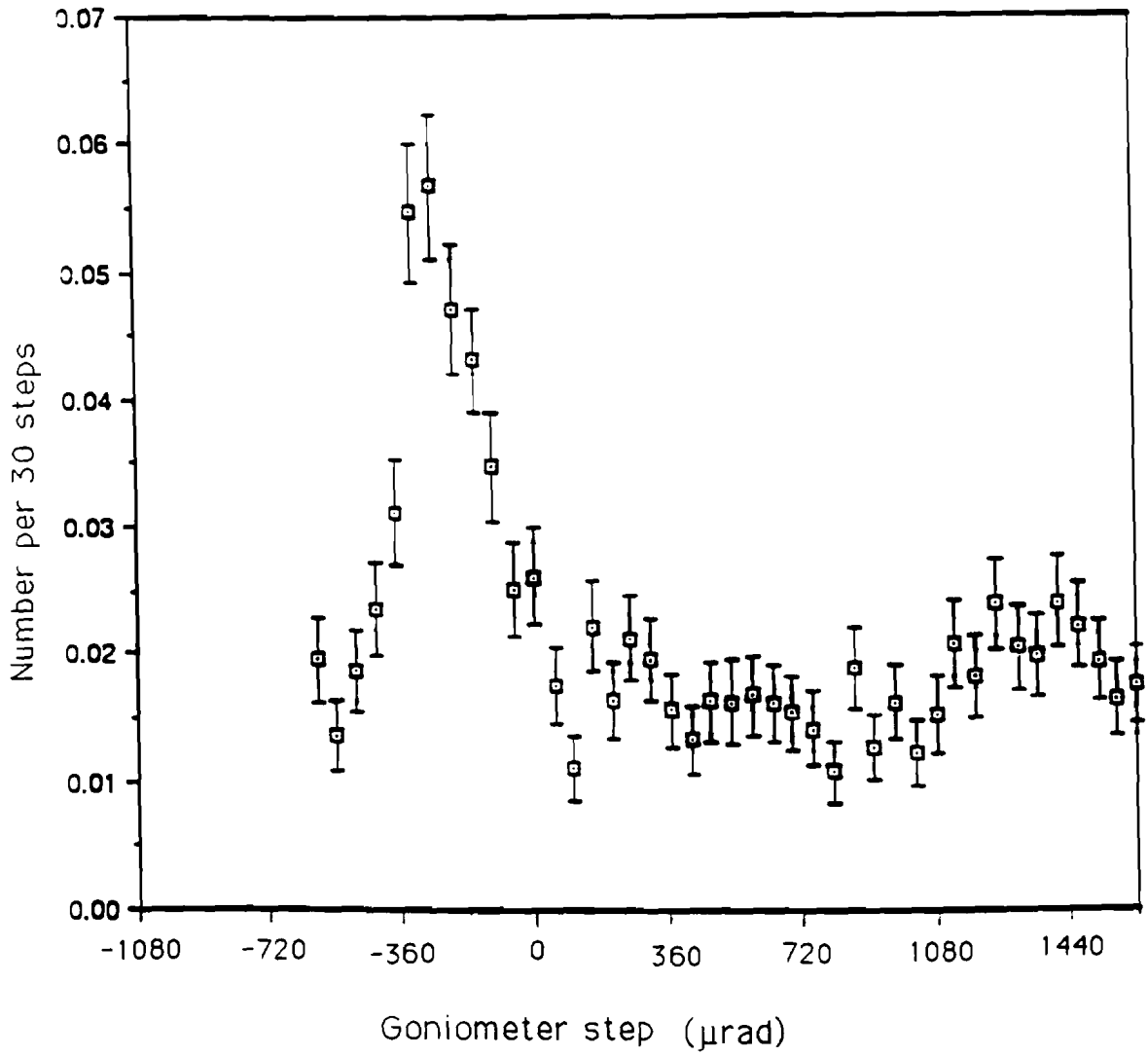

Figure 5.7: Channeling scanning plot from our offline alignment for the 5th crystal. Ratio of channeled events to nonchanneled events versus goniometer steps.

Chapter 6

Reconstruction of Channeling Events

This chapter describes the offline procedure that was used to reconstruct the channeling events. Some of the channeling properties are also studied by using channeled long-lived particles.

6.1 Event Reconstruction

The experimental data were first analyzed by our general event reconstruction program, called the PASS1 program. There is no channeling requirement in the PASS1 program. For every event, a track finding subroutine of the program, called TRKFD, fit the hits in the SSD (PWC) chambers to tracks in the hyperon (baryon) spectrometer, and then required the fits to have a reduced χ^2 less than 15. Only the events which had one track in each of the spectrometers were accepted. Multiple track events were rejected. A 4.5 cm long crystal is one tenth of the silicon nuclear interaction length so that both crystals themselves would cause about 10 % of the nonchanneled random particle interactions producing secondary particles which made multiple tracks. These interaction events would not pass the TRKFD subroutine requirements.

The PASS1 program calculates some useful parameters such as the momentum measured by the hyperon spectrometer, referred to as the hyperon momentum; the

momentum measured by the baryon spectrometer, referred to as the baryon momentum; the ratio of the baryon momentum over the hyperon momentum, R; and the hyperon to baryon decay opening angle, THETA, which is calculated by the equation

$$THETA = [(TY2 - TY1)^2 + (TX2 - TX1)^2]^{\frac{1}{2}}$$

for a small decay angle where TY1 and TY2 are the measured hyperon and baryon angles in the y direction, and TX1 and TX2 are the corresponding angles in the x direction in the laboratory system. Three criteria were set in the PASS1 program: (1) The hyperon momentum must be between 325 GeV/c and 425 GeV/c, (2) R must be less that 1.0, and (3) A "blob" cut, i.e. events were discarded if $0.98 < R < 1.0$ and THETA < 50 μrad at the same time. The last criterion was used to eliminate some of the long-lived beam events such as protons and π^+s.

The channeling trigger vetoed mostly small deflection angle events and therefore enhanced interaction events. As a result, about 50 % of the data we took were killed by TRKFD. Another 20 % of our data were eliminated by the PASS1 criteria. The main reason for the loss is that our crystal trigger is a channeling beam trigger. Most of the events we triggered on had R around 1.0. Due to finite resolution of the spectrometers, about half of the beam events had R larger than 1.0. When we made the cut $R > 1.0$, we cut off almost half of the beam events, both channeled and nonchanneled. One of the very useful plots in our data analysis is the two dimension scatter plot of THETA versus R shown in Fig. 6.1. This plot illustrates the characteristics of all kinds of events that were triggered. The nonchanneled long-lived particles are on the right-lower corner of the plot with R around 1.0 and THETA about 0.0 mrad. The channeled long-lived particles are on the right middle section of the plot with R around 1.0 and THETA about 1.6 mrad. The events between the two groups are those dechanneled events with $0.0 <$ THETA < 1.6 mrad. We can also see some evidence of nonchanneled Σ^+, The curve on the left side shows the kinematics of Σ^+ two body decay $\Sigma^+ \rightarrow n\ \pi^+$ and the curve next to the long-lived particle blob shows the $\Sigma^+ \rightarrow p\ \pi^0$. I will explain it in more detail in chapter 7. The small blob cut here only cut off a few percent of the events, and most of them were long-lived nonchanneled particles. Later in our final analysis, larger R and THETA cuts were used. Only 30

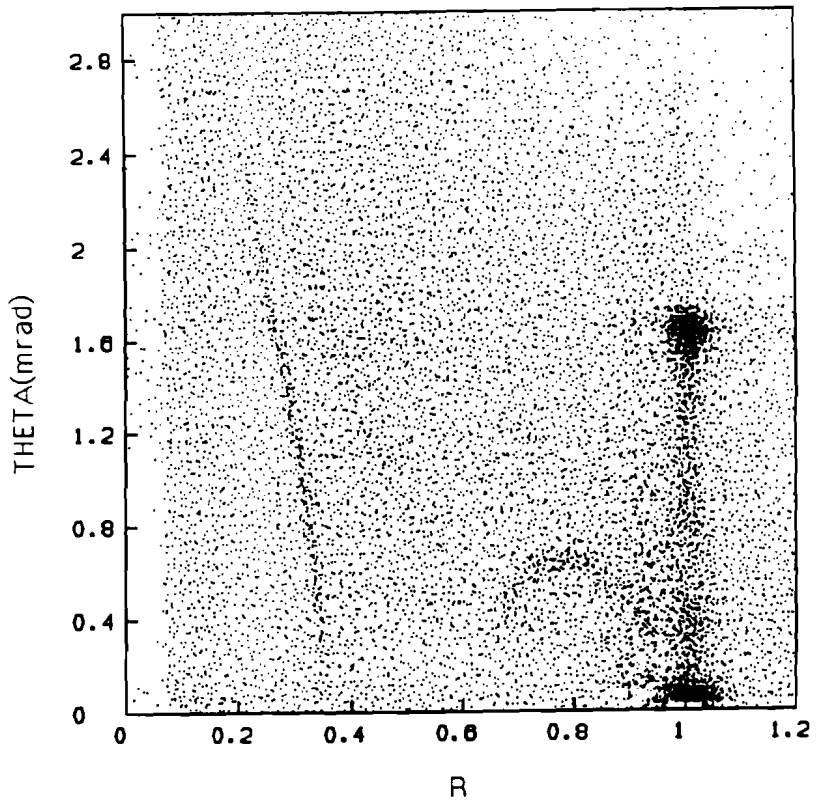

Figure 6.1: THETA versus R plot before R cut

% of our raw data survived the PASS1 program and the majority of them were either channeled or nonchanneled long-lived particles.

Fig. 6.2 (a) shows the energy loss, ΔE, spectrum from the center pad of the 5th crystal for the events that passed the PASS1 program. We had fitted the higher energy loss peak from random nonchanneled events to a Landau distribution, and normalized the spectrum to the Landau most probable energy loss peak value. We required the ΔE to be larger than 0.2 so that we eliminated the background events which had energy loss signal at the electronics noise level. We can see the smaller energy loss channeling peak even with the background because our channeling trigger enhanced the channeling fraction by more than a factor of 10. Fig. 6.2 (b) shows the

distribution of the angle change of a particle track before and after crystals in the Y direction, DTY. From the DTY distribution, we can estimate that about 1/10 of these events were channeling events which had peaks at either -1.6 mrad for the 5th crystal or at +1.6 mrad for the 2nd crystal.

6.2 Selecting Channeling Events

The simplest way to select the channeling events is to select the events that have DTY near or at the two channeling peaks. This could not be done for channeled Σ^+ because the Σ^+ decays and therefore the DTY we measured was not at 1.6 mrad.

The energy loss technique is a well established way to select channeling events from random nonchanneled background events. However, as I mentioned in the previous chapter, there was an incomplete depletion problem with our crystals. The energy loss information from the detectors for the particles that went through the imperfect, lower part of the crystal did not correspond to the real energy loss of the particles. Therefore, we can only apply the standard energy loss technique to the events that went through the perfect part of the crystal. This would lose about half of the channeling events, including the channeled Σ^+s, that went through the imperfect part of the crystal. For selecting channeled Σ^+, of which there are only a few thousands in our data, the energy loss cut may not be the best approach. However, for the purpose of channeling studies, the energy loss cut is a suitable one because we only need to use the long-lived channeling particles of which there are about one million.

We selected the good portion of our crystals by cutting off about 200 μm of the lower section and keeping about 150 μm of higher part of the crystals. Fig. 6.3 plots the energy loss from the center pad of the 5th crystal versus the thickness of the crystal, Y, for a channeling run 4266. The area between two straight lines, $0.221 < Y < 0.236$, was selected as the good portion of the crystal.

Fig. 6.3 also shows an interesting feature about the crystal. We have noticed that there were no channeling small energy loss events at the top 50 μm of the crystal. A possible explanation is that the procedure of implanting detectors on the crystal induced impurities on the top area of the crystal and therefore reduced the channeling.

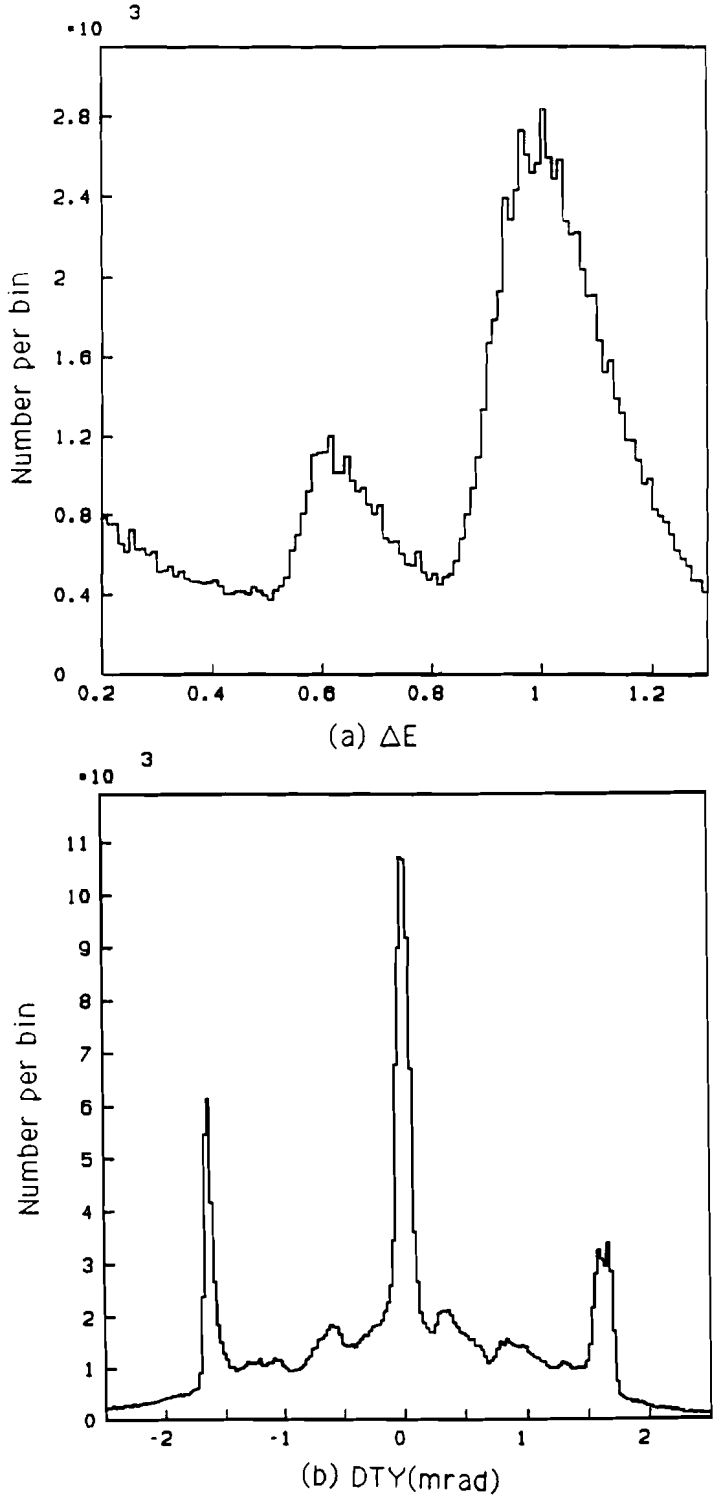

Figure 6.2: (a) Energy loss spectrum from the center pad of the 5th crystal for the events that passed the PASS1. The energy loss was normalized to the Landau peak value. (b) Bending angle, DTY, distribution. The peak at -1.6 mrad corresponds to the 5th crystal, the one at +1.6 mrad to the 2nd crystal.

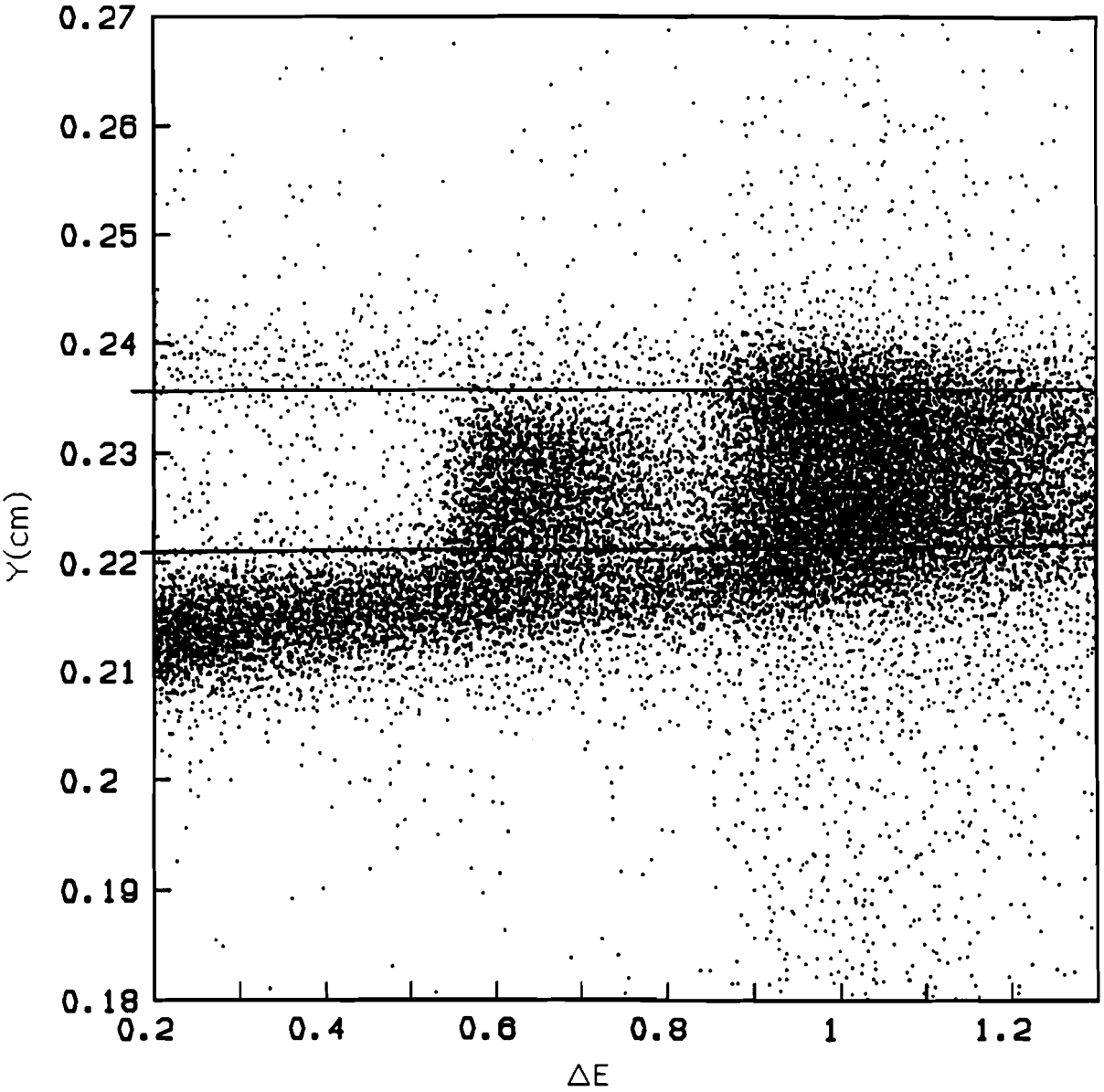

Figure 6.3: Normalized energy loss, ΔE, from the center pad of the 5th crystal versus the thickness of the crystal, Y, for RUN 4266. The area between the two straight lines was selected as the good part of the crystal.

Fig. 6.4 (a) shows the normalized energy loss spectrum of the good portion of the crystal from the center pad of the 5th crystal. An additional cut on bending angle, DTY < -0.8 mrad, was used to enhance the channeling peak. There were very few background events. The channeling energy loss cut was chosen from 0.5 to 0.85 of the Landau peak value.

The energy loss cut on the different pads makes some differences. Using the first pad, the sample might contain many dechanneling events which emerged at the back of the crystals. Using the last pad, one would cut off these dechanneled events but accept particles that scatter into the channel along the bend. This is called volume capture or feeding-in. Using the center pad gave large samples of channeling events, but included both feed-in and dechanneling events. The coincidence of the energy loss cut on the front pad and the back pad gave a very clean channeling signal as shown in Fig. 6.4 (b). There were a few events around DTY=0 which leaked through from the channeling cut. If we apply an additional DTY cut, | DTY | > 0.0008 mrad, we can get rid of these background events. This cut is a very strong channeling cut, which we call "strong channeling cut". We need this strong cut to get clean channeling events for channeling property studies.

Fig. 6.4 (b) shows that there were almost twice as many channeling events from the 5th crystal as those from the 2nd crystal under the coincident energy loss cut. If we are using the energy loss cut only on the center pad, (see Fig. 6.5), we would see almost the same number of channeling events from the two crystals, but the angular distribution of the 2nd crystal was about twice as wide as that of the 5th crystal. What was wrong with the 2nd crystal? This will be discussed in the next section.

6.3 Problems with the 2nd Crystal

After the experiment, all the crystals were shipped back to the Nuclear Physics Institute in St. Petersburg, Russia. A film decorating technique was used to check the crystals. This method [61] could reveal invisible defects in the Si wafers and different inhomogeneities connected with impurities and structure defects. When a thin Si-H film was grown on a Si wafer surface in a special solution, all kinds of inhomogeneities,

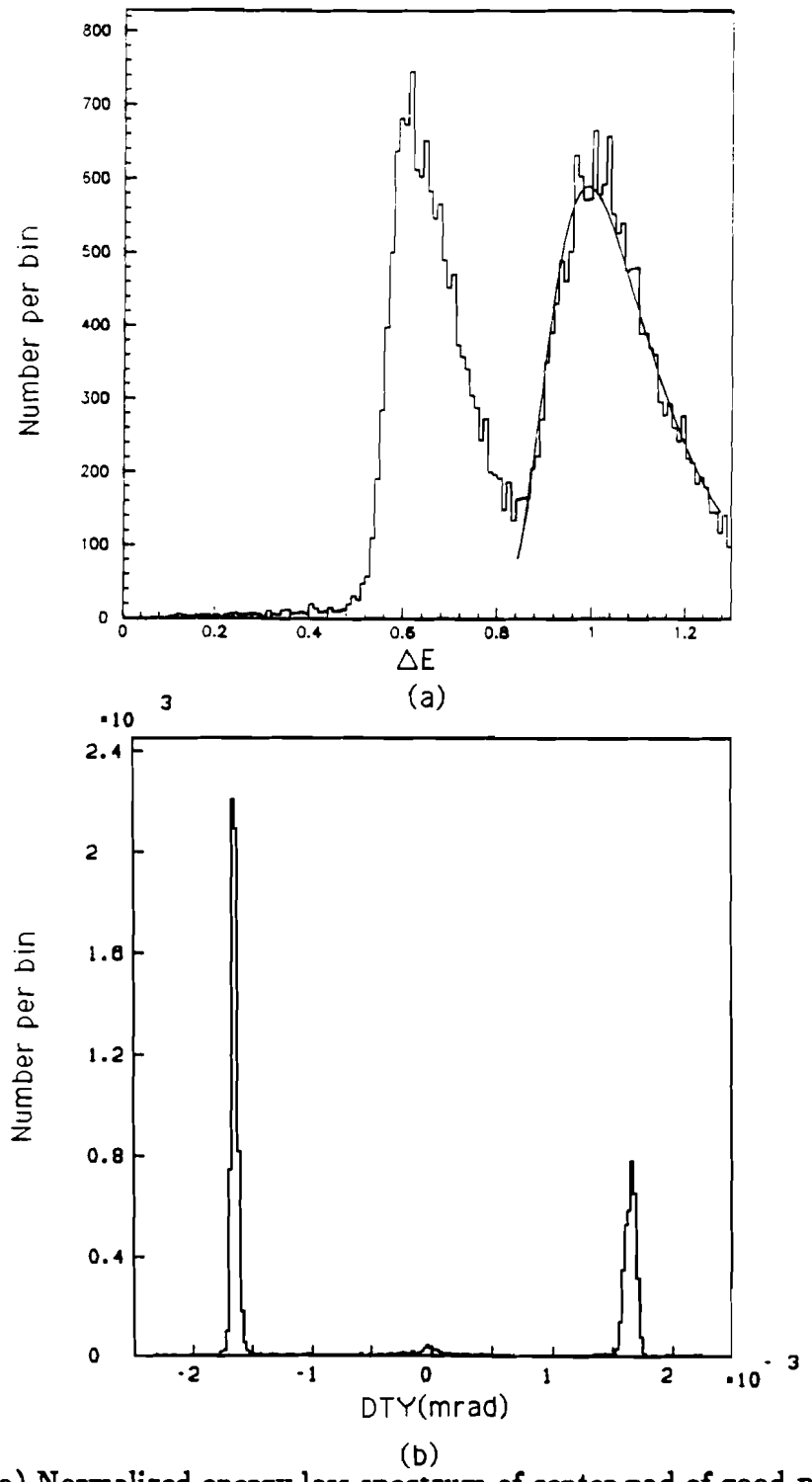

Figure 6.4: (a) Normalized energy loss spectrum of center pad of good portion of the 5th crystal. (b) DTY distribution after strong energy loss channeling cut.

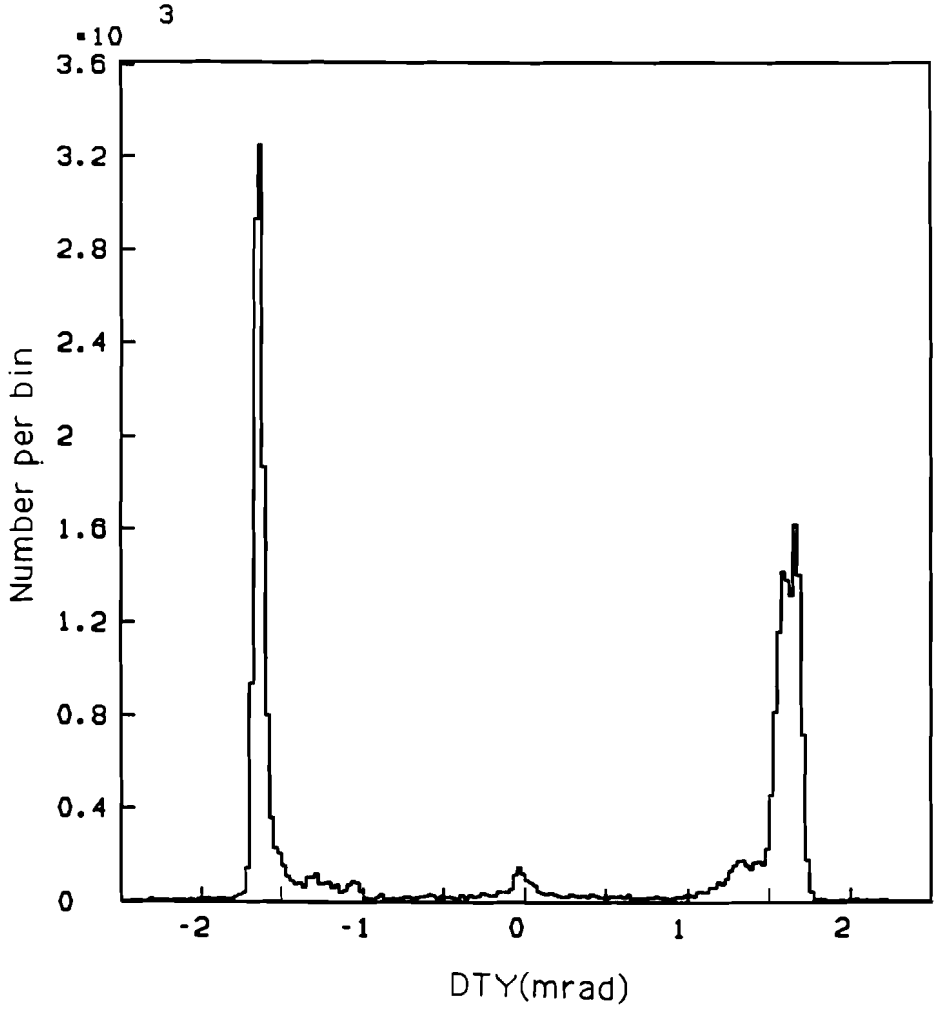

Figure 6.5: DTY distribution after energy loss channeling cut only on the center pad.

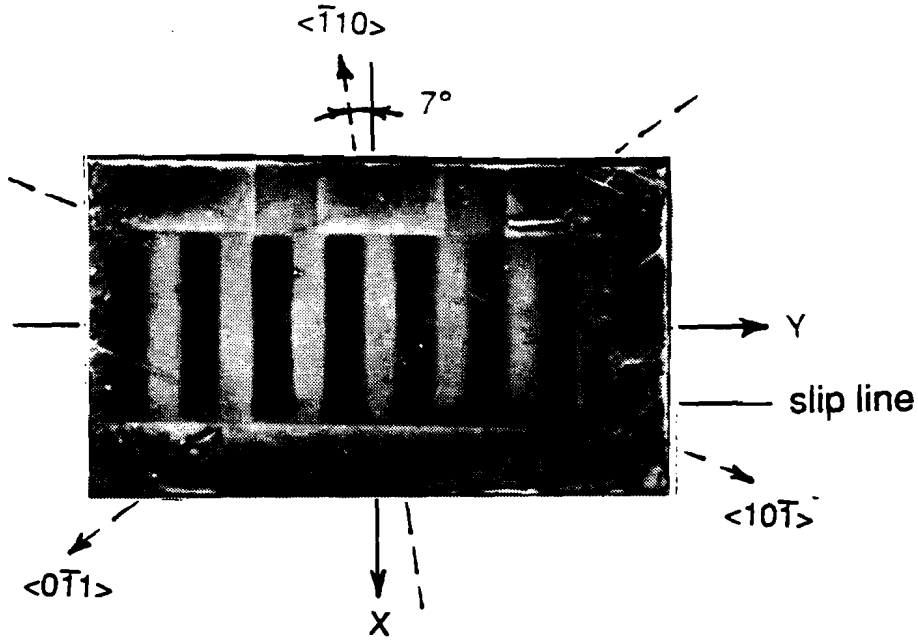

Figure 6.6: The Si-H film of the (111) plane of the 2nd crystal. The slip lines were in the crystal axis direction.

exposed on the crystal surface, would change the growth conditions of the Si-H film. As a result, the film had different thicknesses with different colors corresponding to the structure inhomogeneities and defects.

Fig. 6.6 shows a Si-H film which was grown on the surface of the 2nd crystal after the run. A prominent set of slip lines starting at the 6th pad revealed the structure defects. Notice that the direction of the slip lines corresponds to the the crystallography orientation, axis <110>, <101> and <011>.

These slip lines might have occured when strains appeared during the growth of the crystals or during the cutting procedure used to fabricate the crystals. They

could also have been caused by the plastic deformation of the crystals in the bending device. The carefully aligned and prebent crystals were shipped from Russia inside the goniometer to preserve the orientation in a specially-made double box with spring suspension. Unfortunately, a spring broke during the transportation subjecting the crystals to some strong shocks. One of the crystals (# 7) was even broken.

These slip lines could have caused some irregular dechanneling at the downstream end of the 2nd crystal so that some events had a relatively smaller deflecting angle. To estimate the reduction of the particle bending angle by this kind of dechanneling, we plot the computer simulation results from Nicol [68] of the correlation between the crystal bending angle and the crystal length as shown in Fig. 6.7. The 6th pad is at 2.9 cm in the z direction in this coordinate system. From the plot, we can estimate that the distance from the 6th pad to the end of the crystal corresponds to a bending angle of 60 μrad. To check this hypothesis, we plot the particle bending angle, DTY, distribution of the good part 2nd crystal. Fig. 6.8 (a) shows the DTY distribution under the coincidence of the energy loss channeling cut of the front pad and the last pad detectors. Under such a strong channeling cut, the DTY distribution shows a peak at 1.660 mrad which corresponds to perfect channeling events. Fig. 6.8 (b) shows the DTY distribution under the channeling cut only on the center pad. Those irregular dechanneled events would pass the cut and appeared at a peak of 1.600 mrad. The dechanneling peak is not very well separated from the channeling peak and it makes up 1/3 of total events. The angular difference of these two peaks is about 60 μrad which agreed very well with our estimation. The irregular dechanneling events would contribute about 3 % error to the bending angle measurement for the 2nd crystal if we use the irregular dechanneling events.

6.4 Crystal and Channeling Property Study

6.4.1 Crystal With Beam Phase Space

The beam phase space of our experiment was determined by the aperture of the exit of the hyperon production magnet channel (See chapter 4.3). The size of the beam

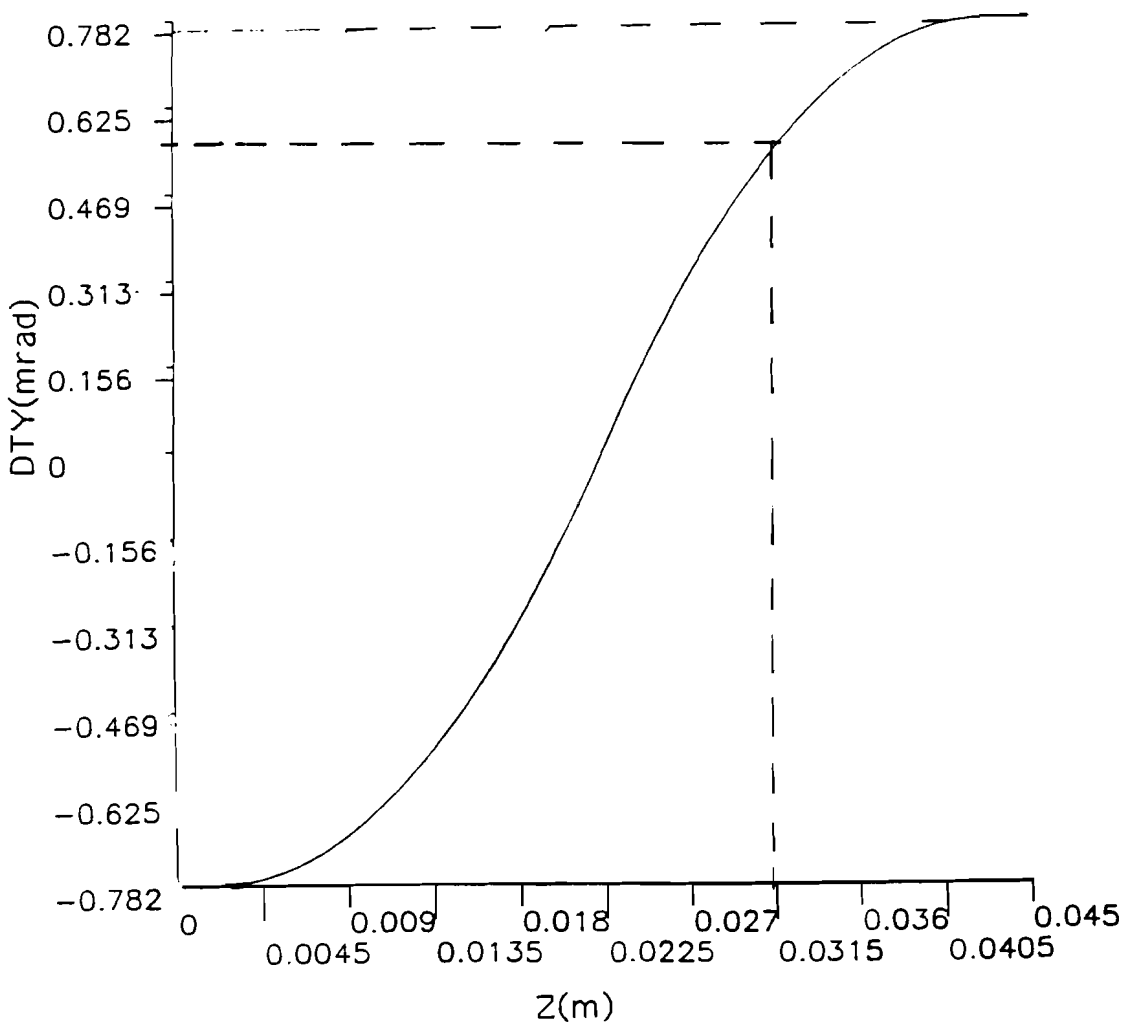

Figure 6.7: Computer simulation plot of crystal bending angle versus the crystal length. The total bending angle is normalized to 1.6 mrad. The angle difference between the 6th pad and the end of the crystal is about 60 μrad.

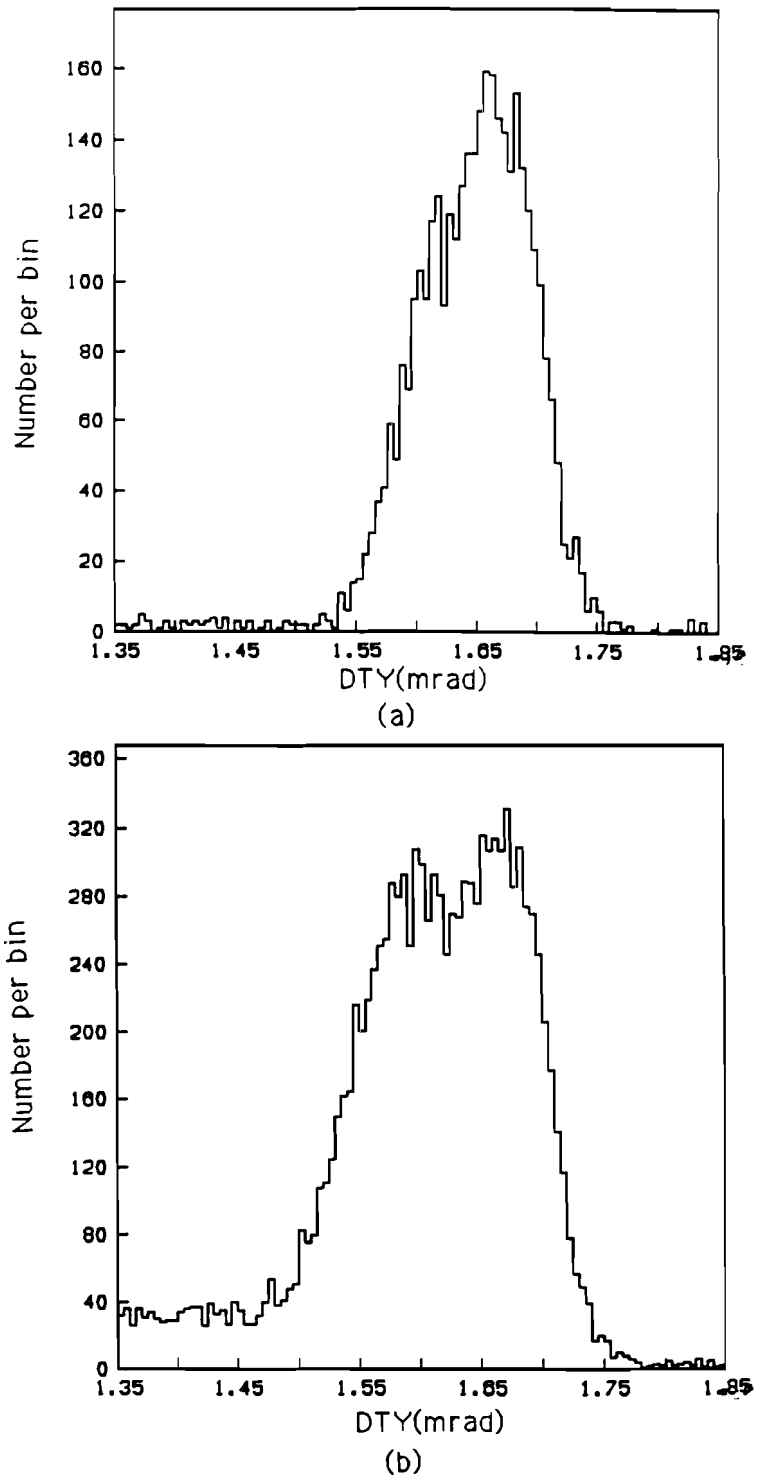

Figure 6.8: DTY distribution of the good part of 2nd crystal under the energy loss cut of (a) the coincidence of the first pad and last pad; (b) the center pad only.

at the front end of the crystals was obtained from a nonchanneled run, 4327, without any cut. The portion of the beam that struck the crystals was determined by the crystal cross section. It can be obtained from a crystal channeling run, like RUN 4266. These two runs were taken under the same conditions, especially the same targeting angle. Fig. 6.9 gives the beam size at the front end of the crystal for (a) the hyperon beam and (b) the part of the beam going through the crystals. The difference of the plots was due to the channeling trigger that required the particle to go through the holes at the ANTI counter and small a energy loss signal from the front detectors on the crystals. Fig. 6.10 shows the x beam phase space, beam opening angle in x (TX1) versus x, for (a) the total beam and (b) the beam going through the crystals. Fig. 6.11 gives the y beam phase space, beam opening angle in y (TY1) versus y, of (a) the total beam and (b) the beam going through the crystals. The background shade on the figures of the crystal trigger corresponds to the total beam size and phase space. This background was due to the inefficiency of our channeling trigger.

To estimate the fraction of the beam that went through the crystals, we enlarged the Fig. 6.9 (b) in the y direction. Fig. 6.12 (a) and (b) show the fraction of the beam cross section which intersects the 5th and 2nd crystals respectively. The total beam size was measured to be 1.3 cm $\times$ 1.8 cm in x and y (FWHM) at the front crystals. Each crystal size in x and y was 1.0 cm $\times$ 0.04 cm (FWHM). From these numbers, we estimated that the crystals' cross sections covered about 3.4% of the total beam.

Fig. 6.13 (a) and (b) show the x and y phase space respectively of the beam that covered the 5th crystal. The beam opening angle in Y is more important. We measured it to be about 70 μrad (FWHM). If we know the channeling critical angle, we can estimate the fraction of channeling.

6.4.2 Channeling Incident Angle

The channeling incident angle in y, TY1, was measured by our hyperon spectrometer under the strong channeling cut, the coincidence of the energy loss cuts of the first and last pad. The resolution of the incident angle was determined by the channeling critical angle and the angular resolution of the spectrometer. The critical angle was estimated to be about 10 μrad and the angular resolution (σ) of the hyperon

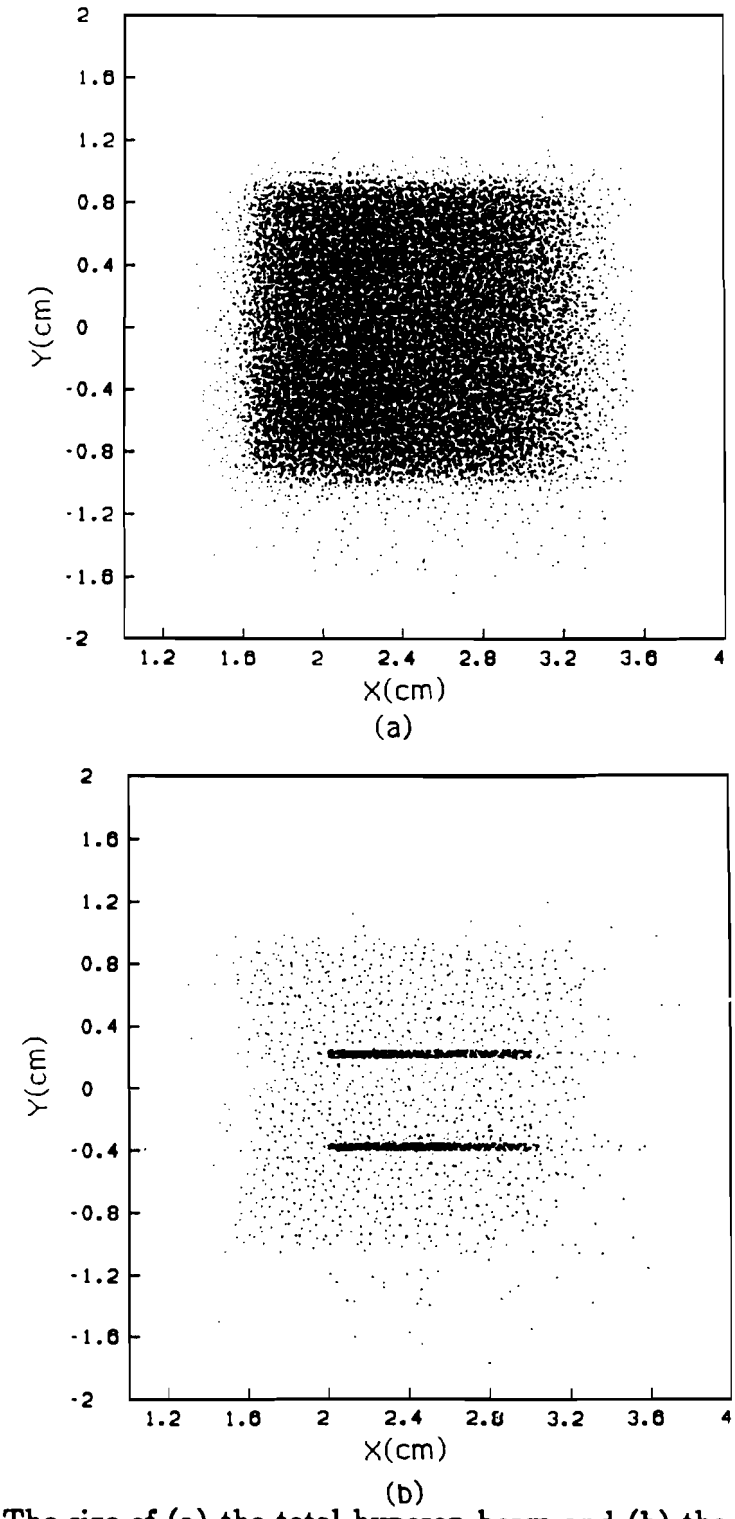

Figure 6.9: The size of (a) the total hyperon beam and (b) the part of beam going through the crystals.

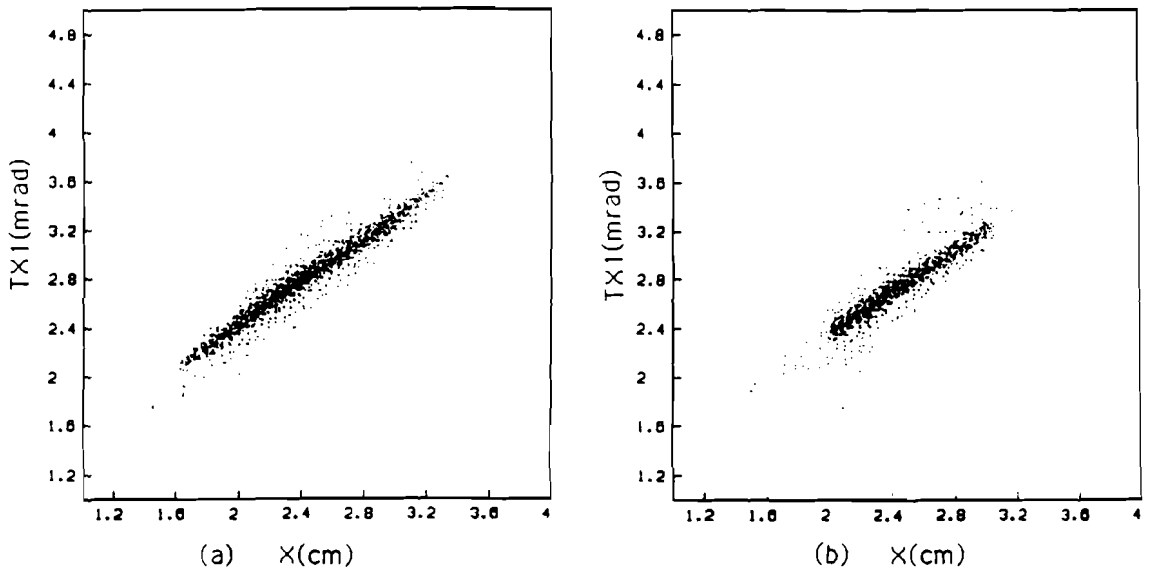

Figure 6.10: The x phase space of (a) the total hyperon beam and (b) the part of beam going through the crystals.

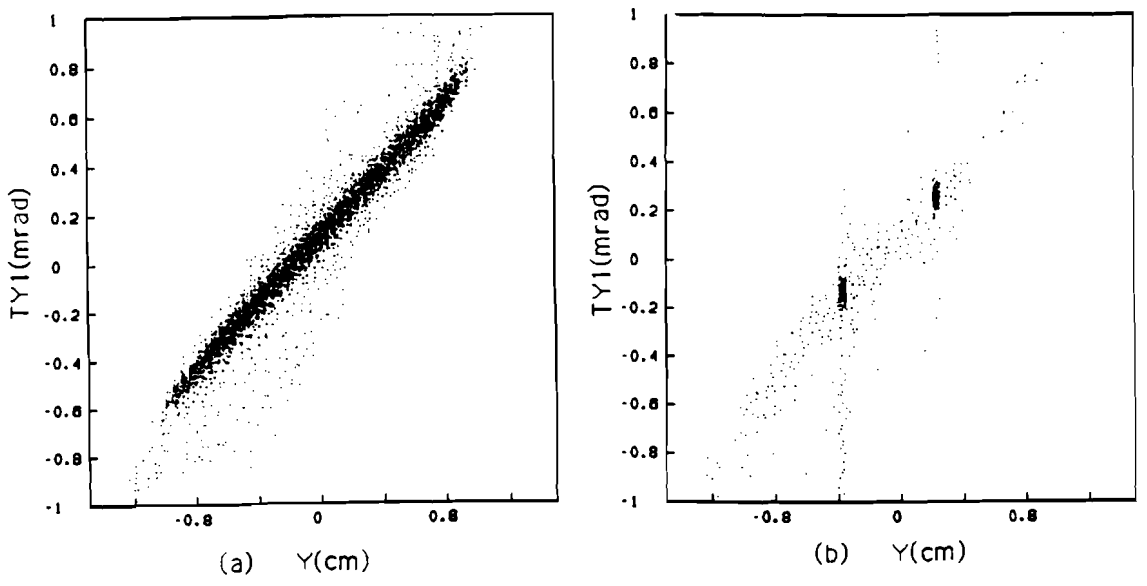

Figure 6.11: The y phase space of (a) the total hyperon beam and (b) the part of beam going through the crystals.

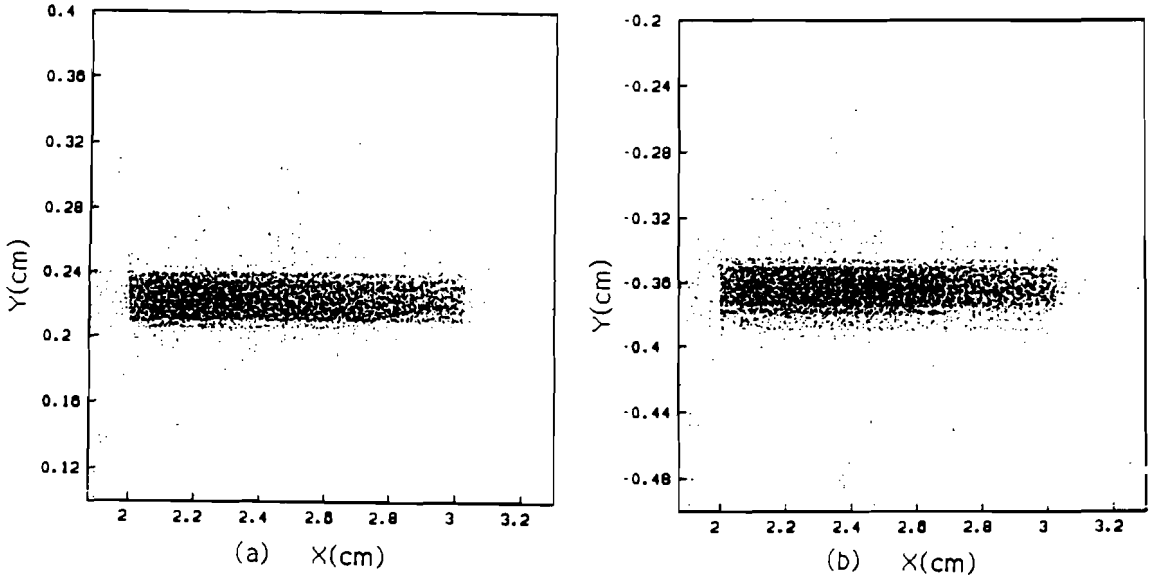

Figure 6.12: The beam size that covered (a) the 5th crystal and (b) the 2nd crystal.

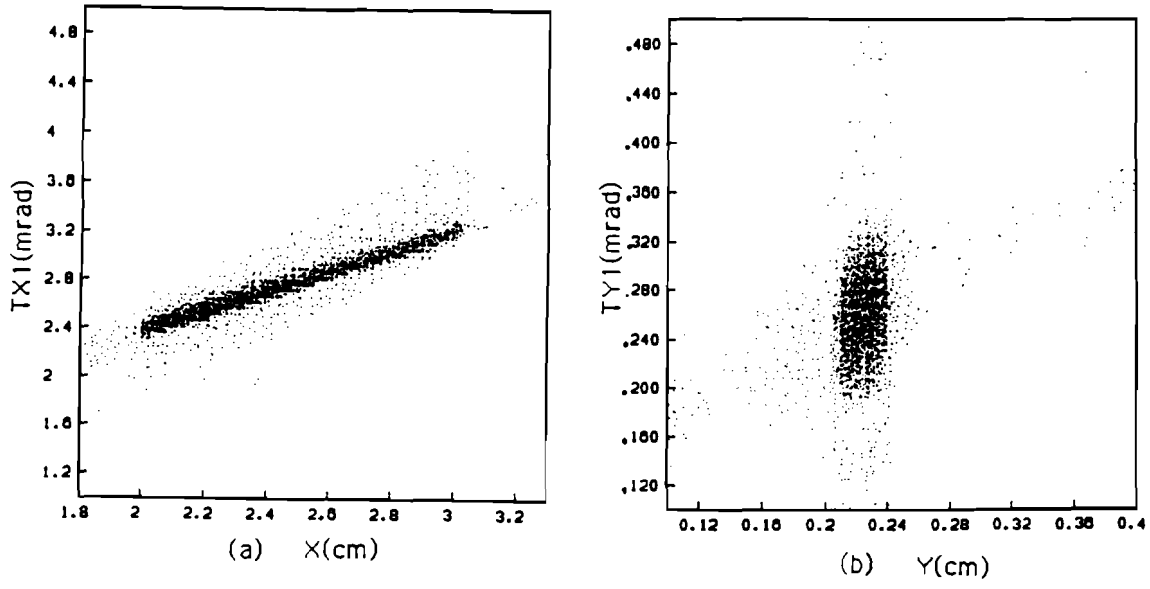

Figure 6.13: Beam phase space that covered the 5th crystal in (a) x direction and (b) y direction.

spectrometer was calculated through a Monte Carlo program to be 10μrad. If we combined these two numbers in quadrature, we would estimate the TY1 resolution (σ) to be about 14 μrad. However, direct measurement of the TY1 of the crystals gave us 30 μrad, much larger than we expected.

The first clue to explain the large experimental TY1 spread for channeling events was from the scatter plot of TY1 versus the position across the front edge of the crystal, x, shown in Fig. 6.14 for (a) the 5th crystal and (b) the 2nd crystal. The plots show a correlation between TY1 and x for the clean channeling events. The tilted (or rotated, or twisted, as we also sometimes call it differently) TY1 from the x axis increased the range ofthe entire TY1 we measured. The tilt of the TY1 was thought to correspond to a tilt of the (111) channeling plane to the x-z plane which was the crystal surface plane. This was a reasonable suggestion because when the crystal plates were cut, the (111) plane was only guaranteed to be within 300 μrad of the cut surface. In addition, during the experiment, we did not make any special effort to insure that the channeling planes were perfectly level, in part because we did not have a convenient and accurate way to do that.

To estimate the channeling incident angle without the effect of tilt, we can simply measure the TY1 in a very narrow x region, for example 2.20 cm $< x <$ 2.25 cm for the 5th crystal and 2.35 cm $< x <$ 2.40 cm for the 2nd crystal. Fig. 6.15 shows the TY1 under this x cut for (a) the 5th crystal and (b) the 2nd crystal. The cut reduced the tilt effect significantly, and we measured the TY1 spread (σ) for both crystals to be 13 μrad which matches the number we expected, 14μrad.

One important application of the channeling incident angle is to select channeling events using the TY1 cut. Most particles that have an incident angle smaller than the critical angle should be channeled, the exceptions are those particles that have a very small impact parameter. We tried to correct the tilt effect so that we could use the corrected TY1 to select channeling events. To make the correction, a cut in x was necessary because the tilt had a different behavior as a function of x. The cut is: 2.00 cm $< x <$ 2.40 cm for the 5th crystal and 2.25 cm $< x <$ 2.65 for the 2nd crystal. We then divided the x region into 10 smaller intervals and fitted the TY1 to a Gaussian function in each area. We plotted the fitted Gaussian peak value of each

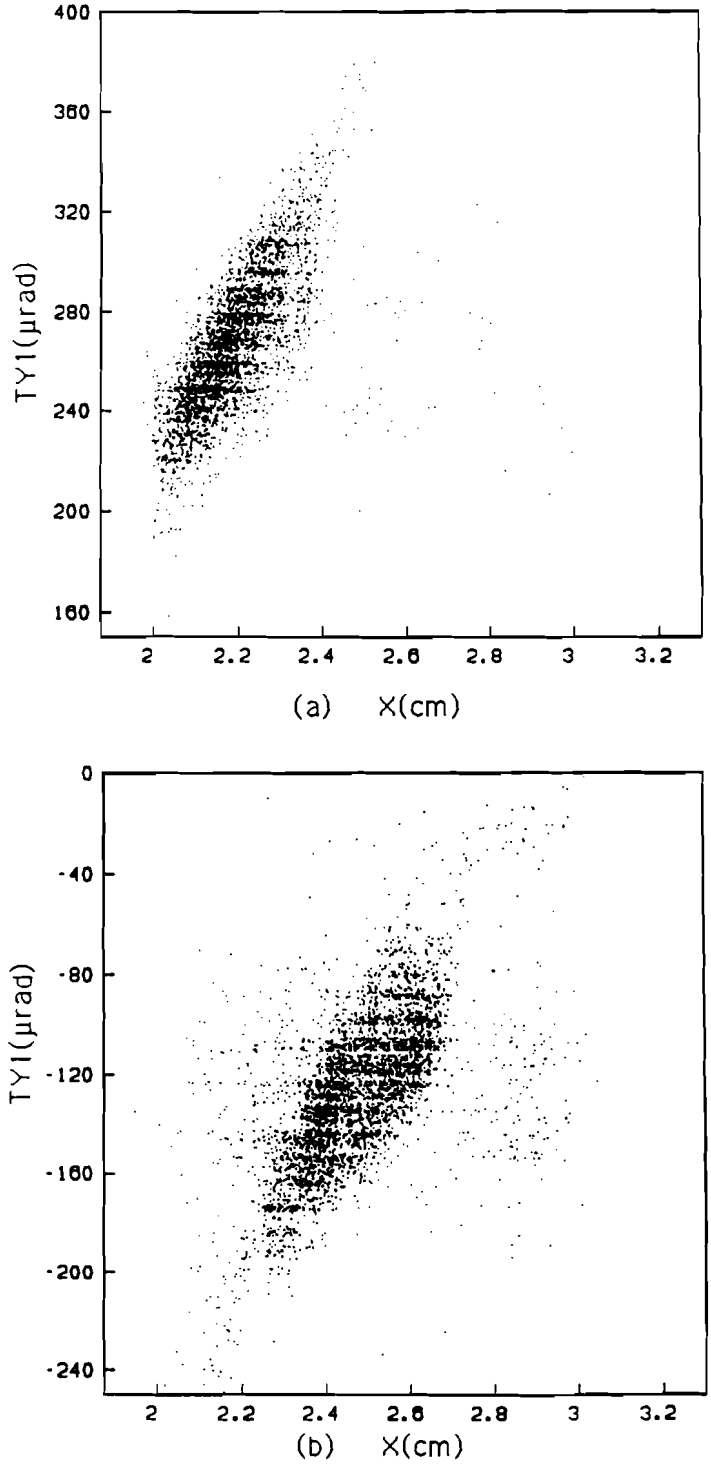

Figure 6.14: TY1 versus x under the strong channeling cut for (a) the 5th crystal and (b) the 2nd crystal.

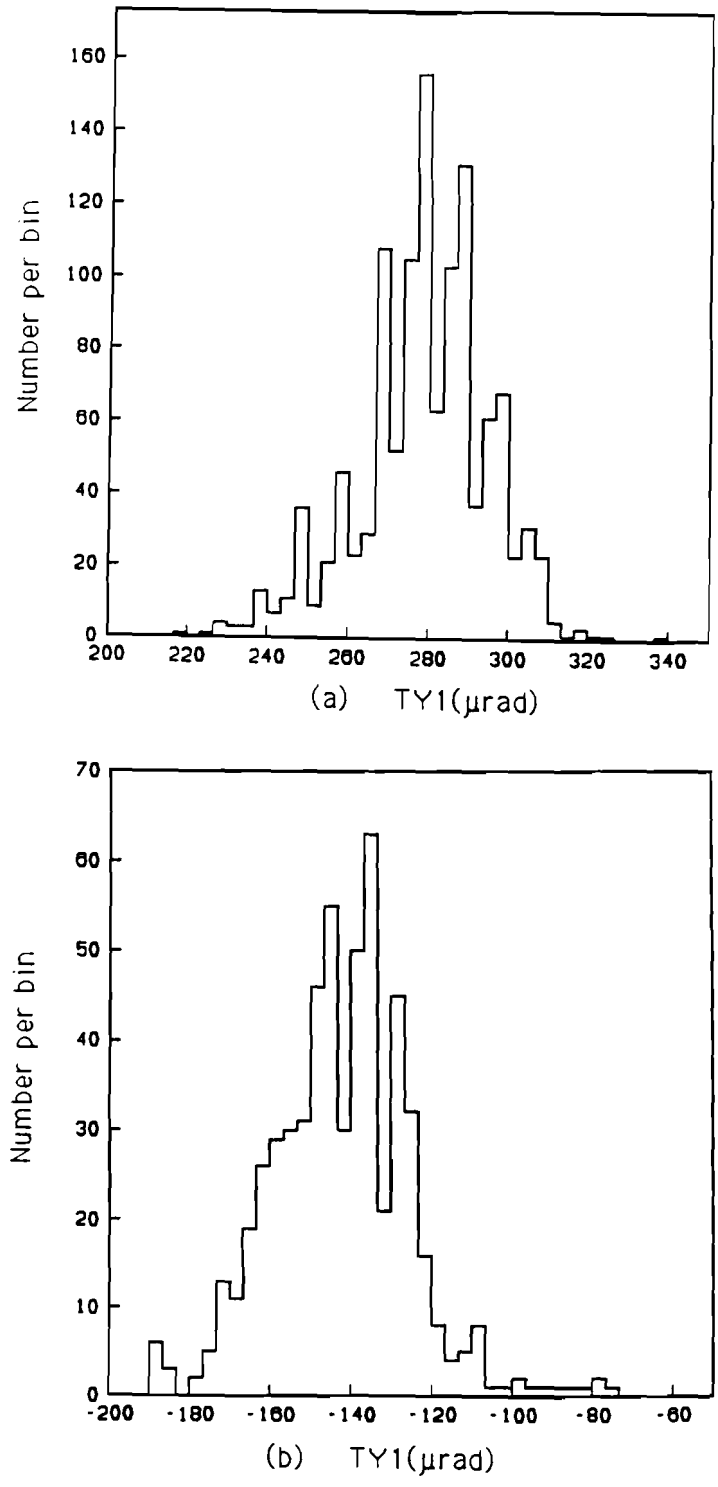

Figure 6.15: TY1 of channeling events of a 0.05 cm x strip for (a) the 5th crystal and (b) the 2nd crystal.

strip as a function of x, shown in Fig. 6.16 for both crystals, and found a function of TY1 in x, called FTY1. We found that FTY1 = -0.243 + 0.233×x mrad for the 5th crystal and FTY1 = -0.613 + 0.197×x mrad for the 2nd crystal. We defined the corrected channeling incident angle, TY1C, as TY1C= TY1 - FTY1. Fig. 6.17 shows the distribution of TY1C for (a) the 5th crystal and (b) the 2nd crystal. The resolution (σ) of the TY1C was 14 μrad which is about the same as we obtained from Fig. 6.15. We tried to use the TY1C as a cut to select channeling events so that we could release the energy loss cut which we know only worked on part of the crystals. However, the TY1C cut was not as efficient or definitive as we expected. The TY1C cut would reject about 30 to 40 % of the total channeling events, those outside the defined x region. Besides, the TY1C cut could not eliminate the events which were too close to the atomic planes and were scattered even if these events had a small incident angle. More background events were included by using the TY1C cut than using the energy loss cut. We decided not to use the corrected channeling incident angle cut.

6.4.3 Channeling Outgoing Angle

The channeling outgoing angle in y, TY2, was measured by our baryon spectrometer under the strong energy loss channeling cut. TY2 was also a function of x in much the same reason that TY1 was. The TY2 versus x distributions for both crystals are shown in Fig. 6.18.

We measured the tilt-cancelled TY2 using the same x strip cut technique. The TY2 nontilted distribution is shown in Fig. 6.19 for (a) the 5th crystal and (b) the 2nd crystal. If we remember the problem with the 2nd crystal, slip lines, it would not be a surprise to us to see the double peak on TY2 of the 2nd crystal. Since the double peak broadened the TY2 distribution of the 2nd crystal, we could estimate the real TY2 resolution using only the data of the 5th crystal. The resolution (σ) was measured as 20 μrad with the same x strip cut we used in the TY1 case. We also fit the TY2 as a function of x to a linear function, FTY2, using the same technique we used for the TY1. We found that FTY2 = -1.790 + 0.187×x mrad for the 5th crystal and FTY2 = -0.770 + 0.303×x mrad for the 2nd crystal. The FTY2 for the

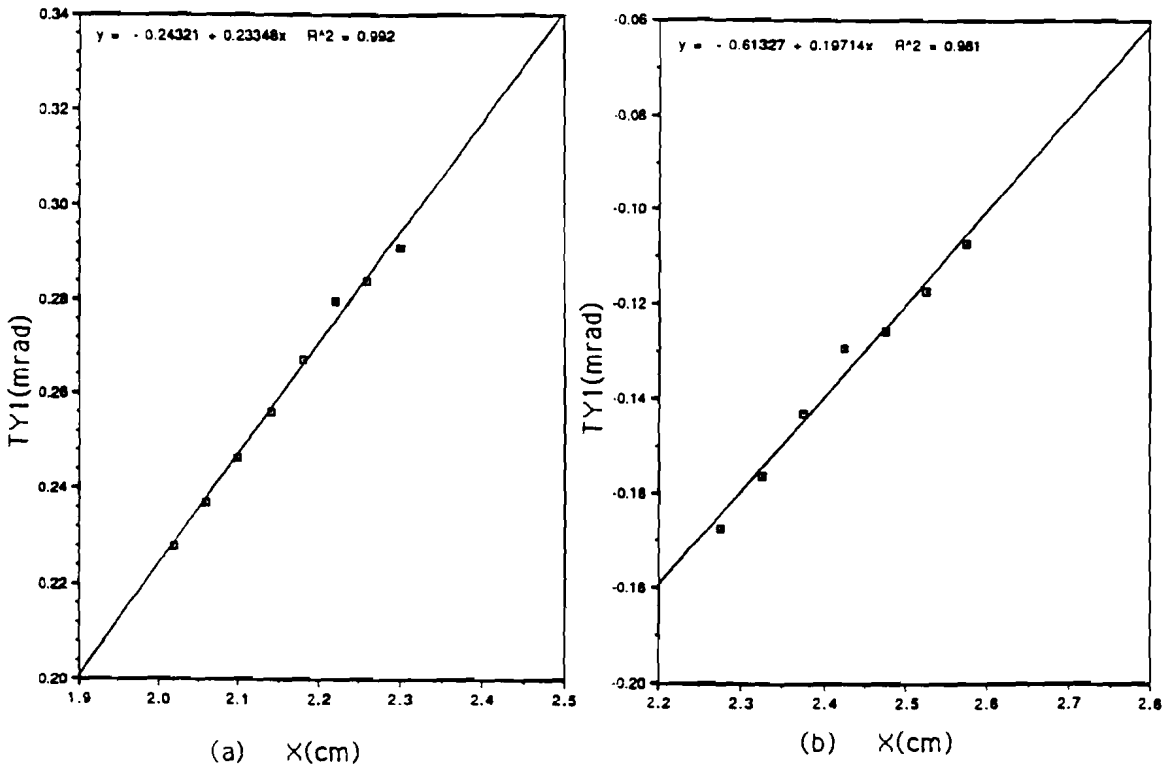

Figure 6.16: TY1 as a function of x for (a) the 5th crystal and (b) the 2nd crystal. Straight line is the fit function.

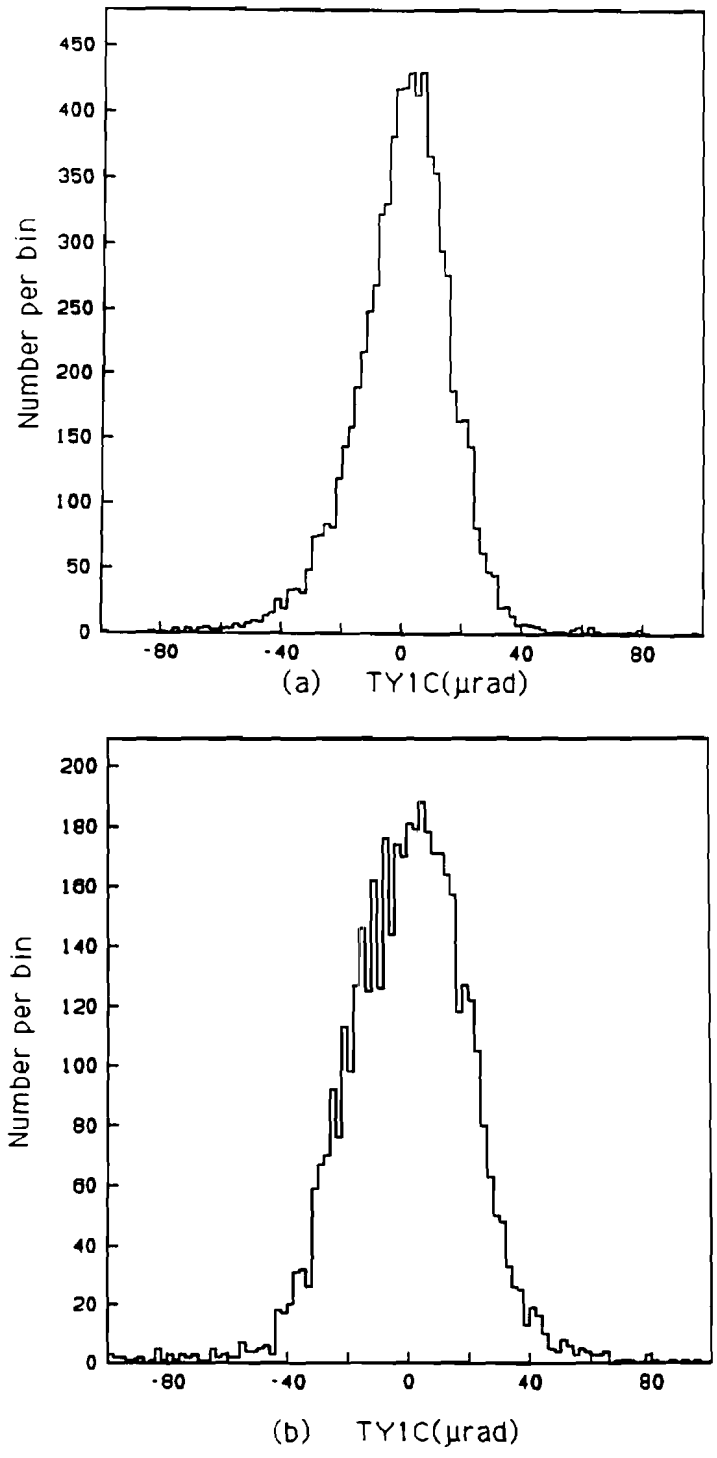

Figure 6.17: Corrected channeling incident angle, TY1C, distribution for (a) the 5th crystal and (b) the 2nd crystal.

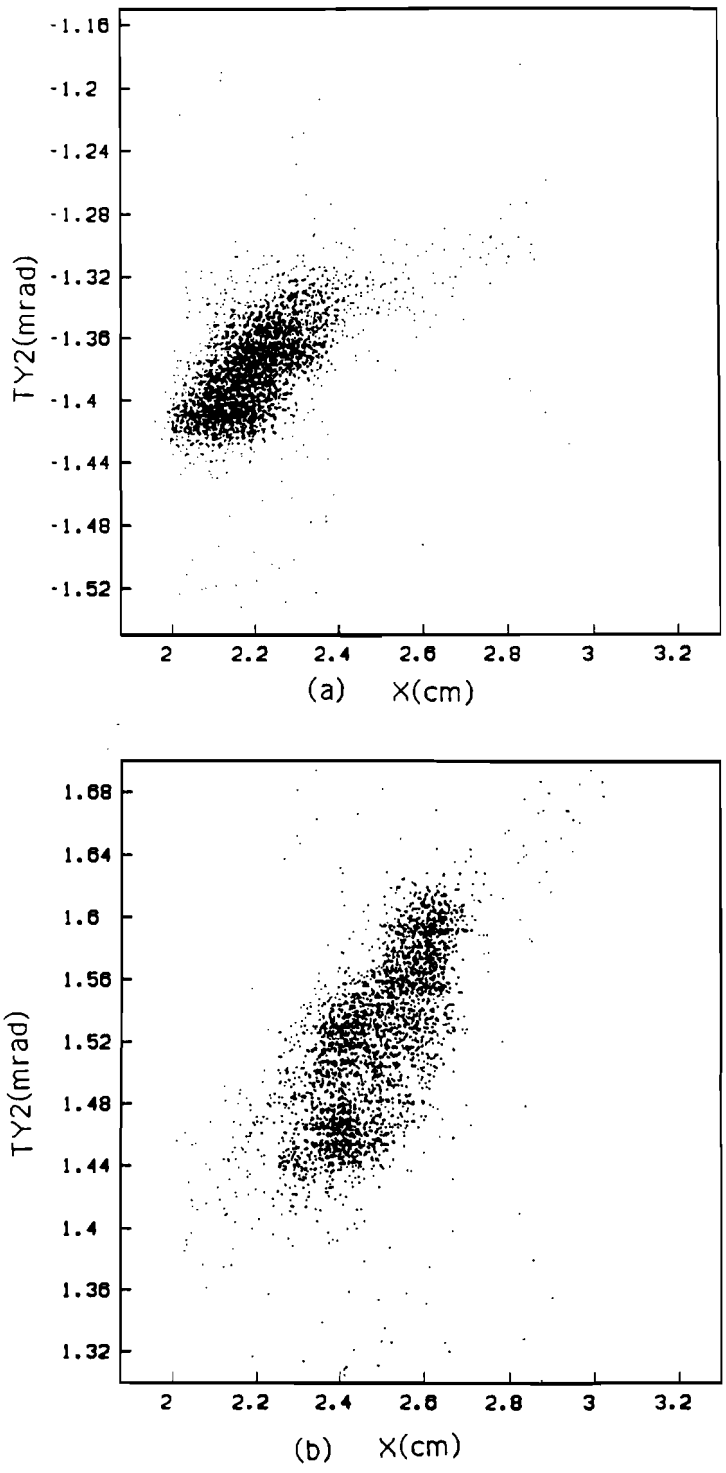

Figure 6.18: Channeling outgoing angle TY2 as a function of x for (a) the 5th crystal and (b) the 2nd crystal.

2nd crystal might not be an accurate fit because of the double peak. Fig. 6.20 shows the fitted linear function for (a) the 5th crystal and (b) the 2nd crystal.

6.4.4 Crystal Bending Angle

The crystal bending angle, DTY, was obtained by taking the difference between the outgoing angle, TY2, and the incident angle, TY1. The resolution of DTY was determined by the resolution of TY1 and TY2. Fig. 6.21 plots the DTY distribution as a function of x for (a) the 5th crystal and (b) the 2nd crystal. From the figure we see that the corelation between DTY and x was not as strong as was the case for TY1 and TY2. The fitted DTY as a function of x, FDTY, is FDTY = $-1.560 - 0.040\times x$ mrad for the 5th crystal and FDTY = $1.420 + 0.092\times x$ mrad for the 2nd crystal. Fig. 6.22 plots the FDTY function for (a) the 5th crystal and (b) the 2nd crystal. The nonlinear behavior of the 2nd crystal was due to the irregular dechanneling of the 2nd crystal. The plot also shows that there is no strong correlation between the DTY and x because the subtraction of TY1 from TY2 cancelled most of the correlation. So we can measure the DTY without doing any tilt correction.

The accurate measurement of DTY is crucial for reconstructing the channeled Σ^+ and estimating the precession angle of the Σ^+ in the crystals because the precession angle is proportional to the bending angle. The detailed distributions of DTY after the strong channeling cut, the coincidence of the energy loss cut between first pad and last pad, for both crystals are shown in Fig. 6.23. The DTY of the Gaussian fitted peak value was -1.649 $\pm$ 0.025 mrad for the 5th crystal and 1.649 $\pm$ 0.043 mrad for the 2nd crystal. The worse resolution of the 2nd crystal was due to the slip line problem. When we reconstructed the channeled Σ^+, we used a loose channeling cut which only cut the energy loss on the center pad. This channeling cut gave us more channeled events. Fig. 6.24 shows the DTY distribution after the loose channeling cut for both crystals. There was more background on the small bending angle side of the 2nd crystal, some of which were dechanneling events. If we fit the distribution using a Gaussian function, we obtained a different peak value: -1.640 $\pm$ 0.030 mrad for the 5th crystal and 1.613 $\pm$ 0.065 mrad for the 2nd crystal. Under the different channeling cuts, for the 5th crystal, DTY differed by up to 9 μrad which is a 0.5 %

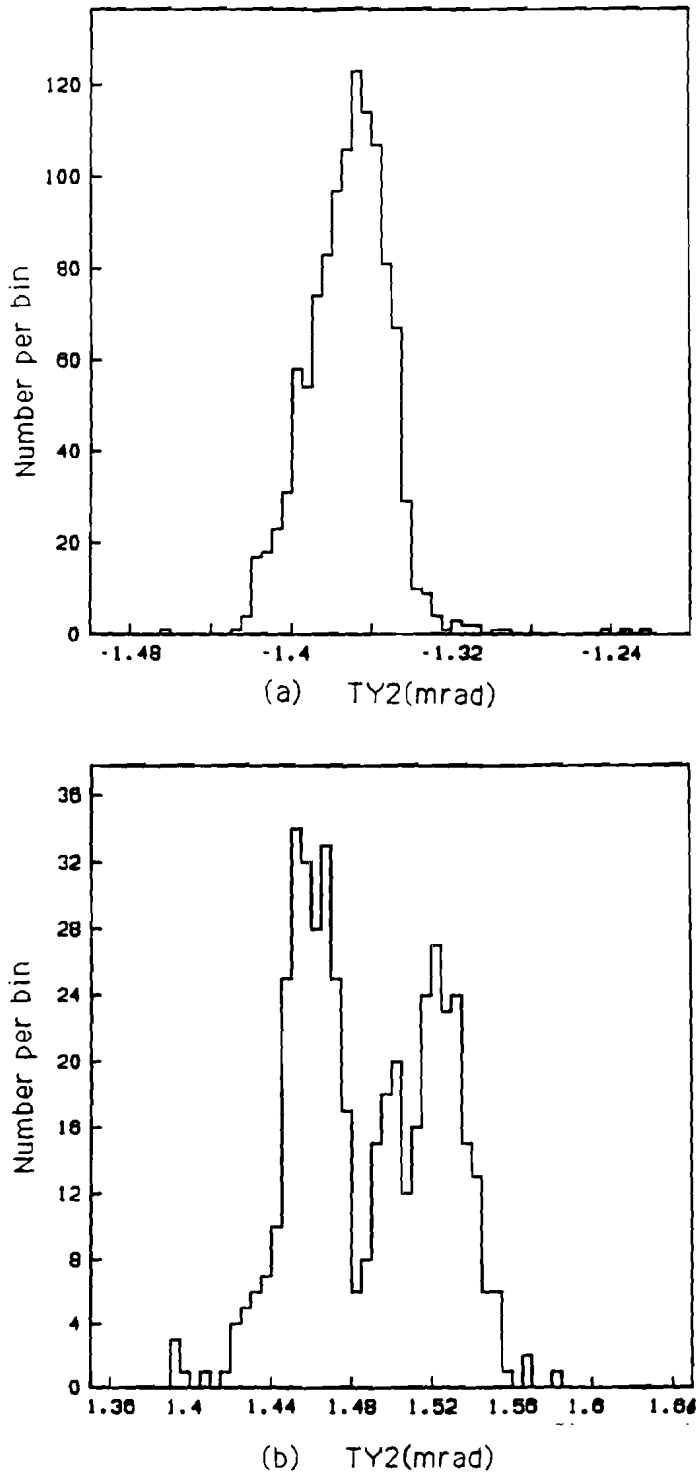

Figure 6.19: TY2 of channeling events of a 0.05 cm x strip for (a) the 5th crystal and (b) the 2nd crystal.

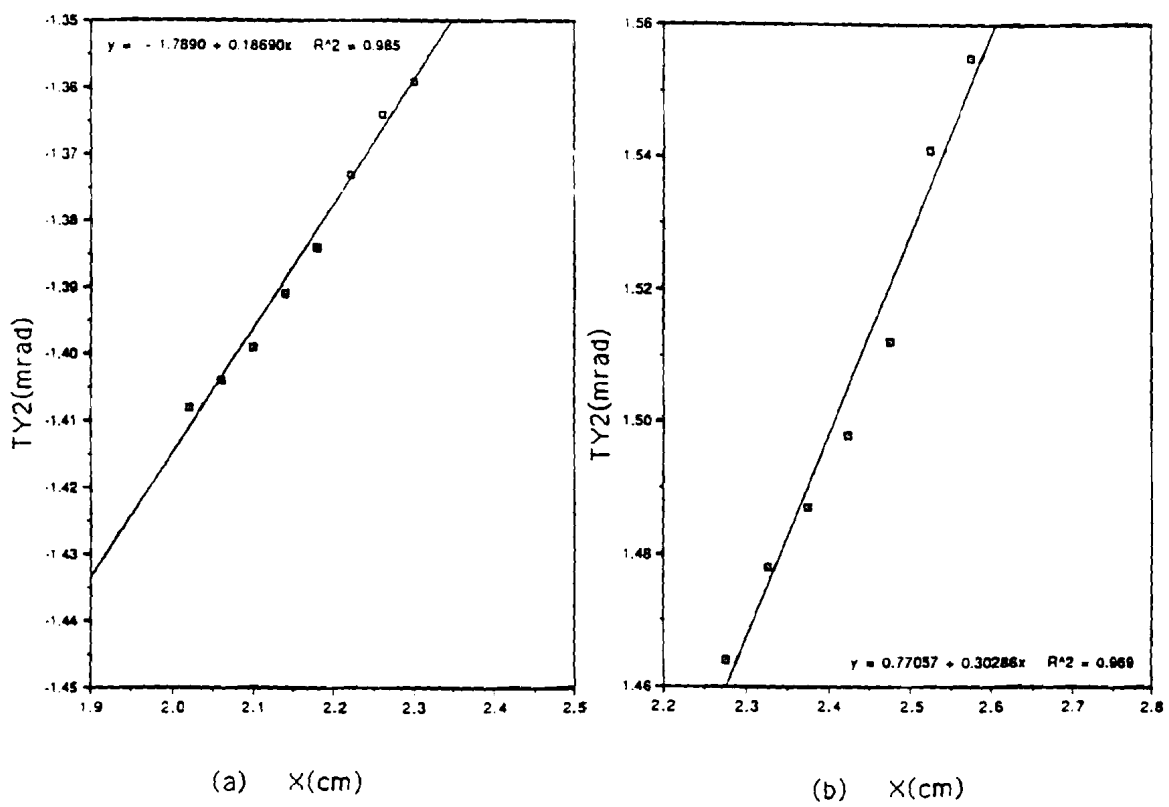

Figure 6.20: TY2 as a function of x for (a) the 5th crystal and (b) the 2nd crystal. Straight line is the fit function.

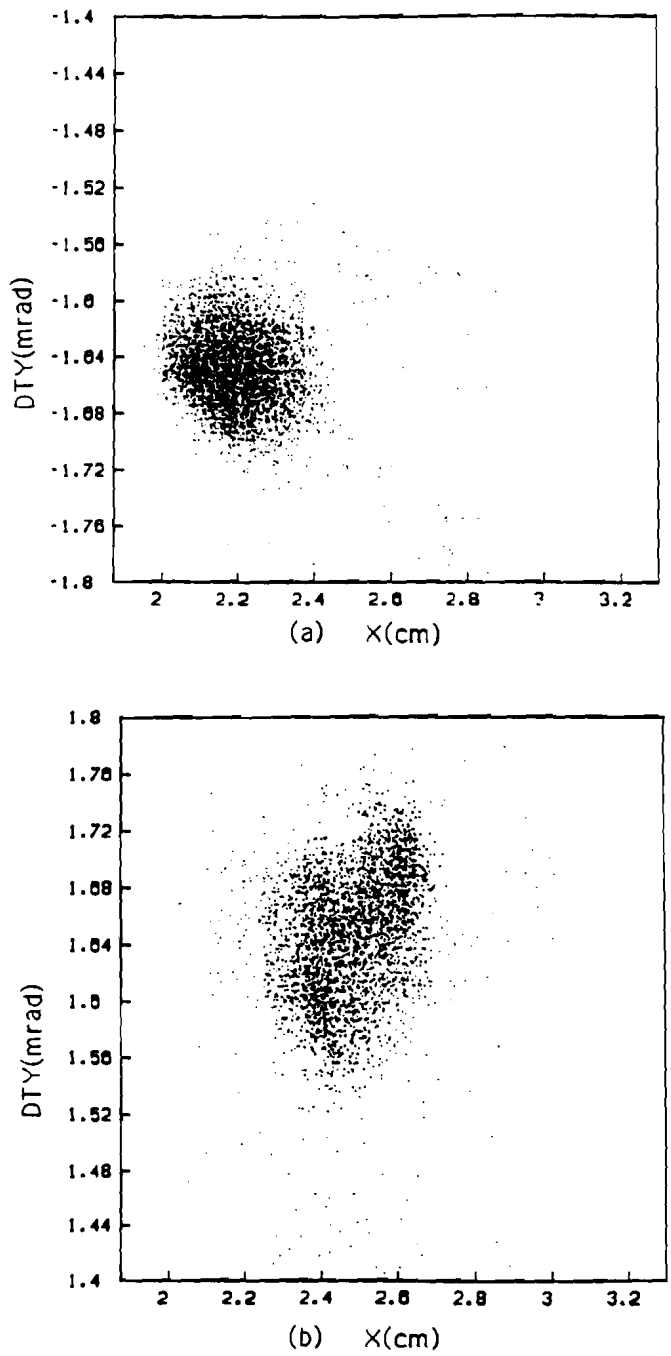

Figure 6.21: Channeling bending angle DTY as a function of x for (a) the 5th crystal and (b) the 2nd crystal.

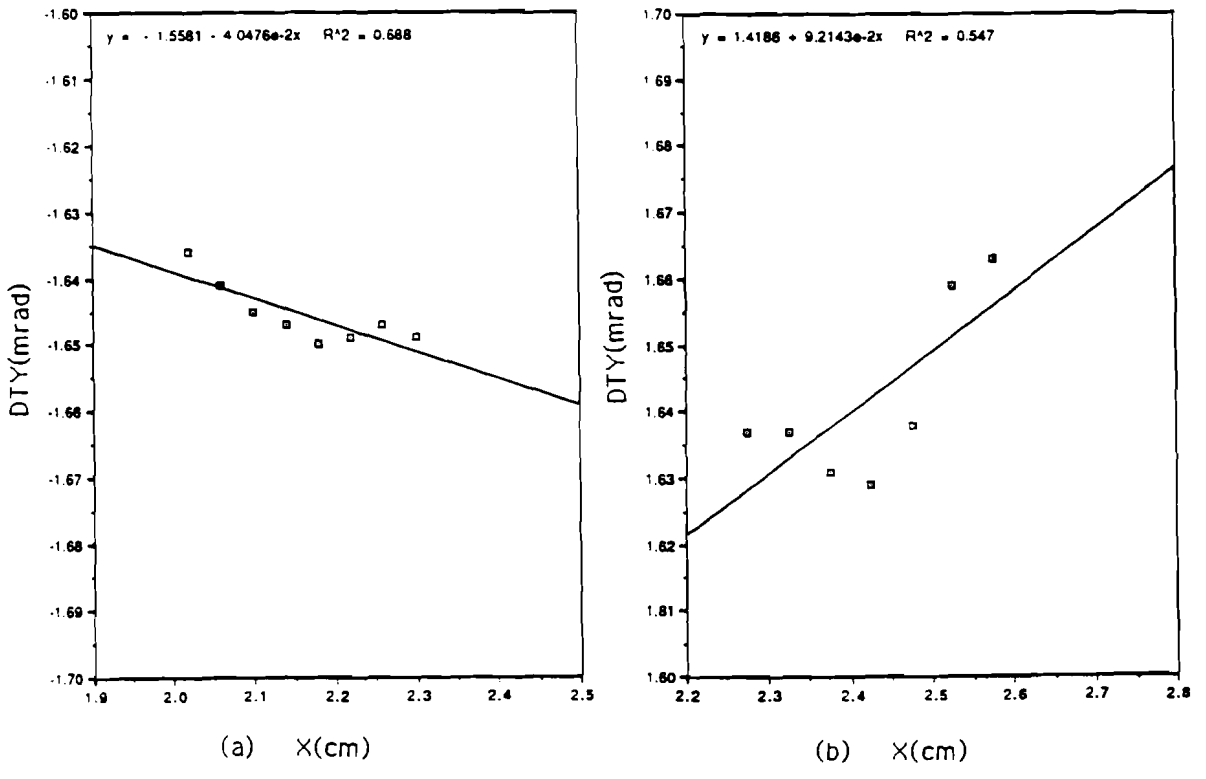

Figure 6.22: DTY as a function of x for (a) the 5th crystal and (b) the 2nd crystal. Straight line is the fit function.

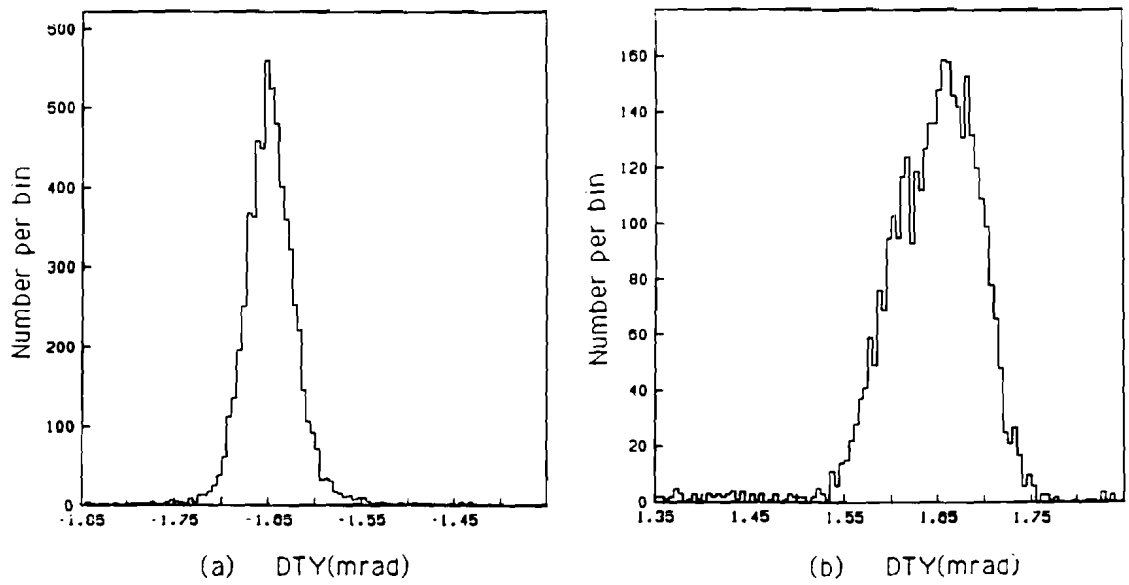

Figure 6.23: Crystal bending angle DTY under the strong channeling cut for (a) the 5th crystal and (b) the 2nd crystal.

relative error on DTY and for the 2nd crystal, DTY differed by 36 μrad which is a 2.2 % relative error on DTY. From this, we can conclude that the error from the DTY would be a maximum of 2.2 % which is smaller than the statistical error discussed in later chapters.

6.5 Channeling Fraction

6.5.1 Theoretical Calculation

If we cut the silicon along the (111) plane, there are actually two different channels: the major (wide) channel and the small (narrow) channel. Fig. 6.25 shows the potentials of the channels. The major channel is three times wider and significantly deeper than the small channel. Almost all the channeling takes place in the major channel. In our channeling experiment, we can ignore the small channel and treat the crystal as if it has only the major channel for the (111) planes.

To calculate the channeling fraction, we need to know the channeling critical angle. Lindhard [36] and Gemmel [41] have derived the equations to calculate the critical

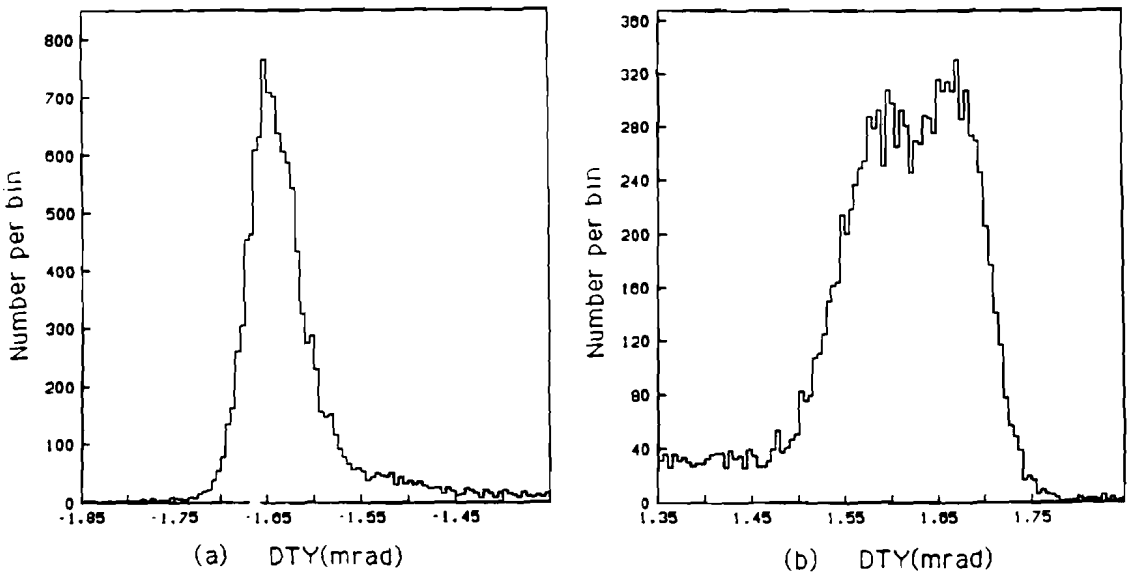

Figure 6.24: Crystal bending angle DTY under the loose channeling cut for (a) the 5th crystal and (b) the 2nd crystal.

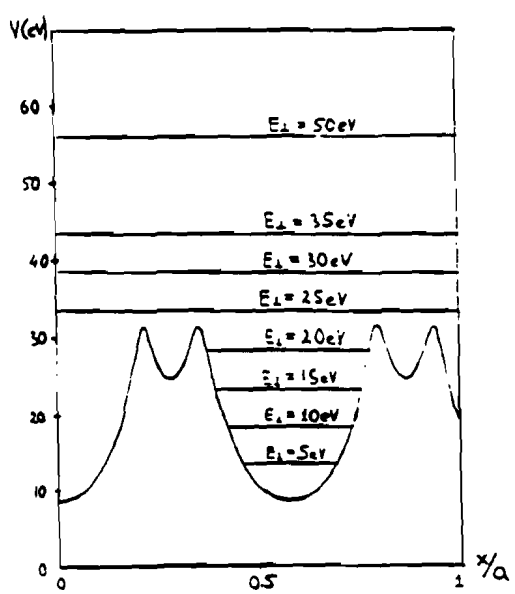

Figure 6.25: Potential and energy levels for silicon (111) plane. There are two potential wells. The deeper potential well is the major region for channeling.

angle. Using Lindhard's equation, (3.6), we estimated the critical angle for 375 GeV/c channeled Σ^+ for the Si (111) plane to be about 9.03 μrad. Using Gemmel's equation, the angle is 8.16 μrad at FWHM. These estimates differ by a few percent in part due to different approximations and assumptions about the atomic potential. We used 8.2 $\pm$ 1.0 μrad as the calculated critical angle.

From Fig. 6.13, we measured the TY1 (FWHM) covered by an individual crystal to be 70 μrad. So the angular fraction of the beam inside the critical angle was calculated to be $\frac{8.2\mu rad}{70\mu rad} \times 2 = 23$ % . The factor of 2 arises from applying the critical angle in both plus and minus directions. However, not all the particles within the critical angle will be channeled. Some of the particles are so close to the atomic plane and will be scattered. We define this deduction as the surface acceptance. Carrigan [43] estimated the surface acceptance for our case to be about 55 $\pm$ 20 %. Another factor we need to consider is the dechanneling, we estimated the total dechanneling factor to be about 20 $\pm$ 5 %, which gives 80 $\pm$ 5 % acceptance. Now, adding the spacial fraction, which is 3.4 % as we calculated before, we estimated the total channeling fraction to be, 3.4 % $\times$ 23 % $\times$ 55 % $\times$ 80 % = 0.34 %.

6.5.2 Experimental Estimation

To compare the experimental channeling rate with the theoretical estimated value, we have to define our trigger acceptance. Our trigger enhanced our channeling fraction both in the T1, beam trigger level and the T3, channeling trigger level. The difference between our T1 and the normal T1 used in the nonchanneled part of the experiment was that our T1 included a two-hole scintillator ANTI counter. We compared the trigger rate from the channeling run, 4266, with that from the nonchanneling run, 4388, in Table 6.1. The T1 rate in Table 6.1 was normalized to the beam rate, so the T1(4266)/T1(4388) would be the fraction of the beam that went through the two holes over the total beam. The value was measured to be 5.156 % which was larger than the beam fraction that went through the crystal, 3.4 %, as we expected because the size of the ANTI hole is larger than the crystal cross section, which we used to get the 3.4 %. If we include in the fact that the crystal cross section is about $\frac{4}{5}$ of the ANTI hole size in y direction, the T1(4266)/T1(4388) for the real crystal part is 4.1

	Channeled RUN 4266	Nonchanneled RUN 4388
Beam rate per spill (23s)	0.9406×10^{12}	0.5738×10^{12}
T1/Beam	0.232×10^{-6}	0.045×10^{-4}
T3/Beam	0.130×10^{-7}	0.021×10^{-6}
T3/T1	0.056	0.0047

Table 6.1: Beam and trigger rate for channeling run 4266 and nonchanneled run 4388.

%, which is close to the 3.4 % estimated value. We also get the T3/T1 fraction for the channeling run. As we mentioned in the early trigger chapter, the rate reduction of T3 from T1 was due to the deflection veto counter and the threshold of the detector on the surface of the crystals.

We used the data from one channeling run, 4266, to estimate the channeling fraction. The raw data contains 1,262,560 events triggered by T3. The PASS1 track finding program eliminated 607,162 raw events and the PASS1 momentum and blob cut discarded an additional 351,674 events. We set a simple channeling cut: -1.750 mrad $<$ DTY $<$ -1.550 mrad for the 5th crystal and 1.550 mrad $<$ DTY $<$ 1.750 mrad for the 2nd crystal. Among the rest of the 303,724 events, 54,065 passed the channeling cut: 27,400 for the 5th crystal and 26,665 for the 2nd crystal. Using this number, we calculated the channeling fraction over the T3 to be 0.0428 and the channeling fraction over our T1 to be 0.002498. Then we converted the channeling fraction to the whole hyperon beam size by multiplying by the ANTI fraction T1(4266)/T1(4388). The channeling fraction over the total beam was then calculated to be about 0.01237 %. This number is about 27 times less than the theoretical number of 0.34 %. All the fractions are listed on Table 6.2.

To explain the factor of 27 larger in the channeling rate by theoretical calculation, we need to include many factors that we neglected when we did the calculation. One factor is the data-taking dead time which reduced the T1 rate to 71 $\pm$ 10 %. Another factor is the efficiency of the offline event reconstruction, which is about 80 $\pm$ 10 %, and the third factor is 46 % from the momentum cut. These factors reduced the difference in rate from a factor of 27 to a factor of 7. We also found that the channeling fraction of the crystals was not homogeneous in the x direction,

RUN 4266	
raw data, T3	1262560
Killed by track finding	607162
Killed by momentum cut	351674
Survived	303724
Channeling (5th)	27400
Channeling (2nd)	26665
Channeling (5th and 2nd)	54065
Channeling/Survive	0.178
Channeling/T3	0.0428
Channeling/T1	0.002498
Channeling/T1(no ANTI)	0.0001237

Table 6.2: Channeling Fraction from one tape data of run 4266.

so that only about 1/4 of the total crystal in x was fully working for channeling. The channeling inefficiency of the crystal in the x direction may be due to the tilt-like plane of our crystals. As we mentioned before, channeling does not happen at the top 50 μm of the crystals because of the impurities. This is another $\frac{1}{8}$ factor reduction. These bring the discrepancy between the theoretical estimation and the experimental observation of the channeling rate to a factor of only 1.5. The final theoretical calculated channeling fraction is 0.019 $\pm$ 0.009 %, which is consistent with the experimental value. We note that the crystals we used were not ideal. The problems with the crystals cost us about an order of magnitude in efficiency.

Chapter 7

Reconstruction of Channeled Σ^+

Starting from this chapter, we discuss only the Σ^+ decay events. This chapter describes the procedures that we used to reconstruct both the nonchanneled Σ^+ and channeled Σ^+. Two groups of channeled Σ^+ were obtained, one with the channeling cut and the other without it.

7.1 Reconstruction of Nonchanneled Σ^+

From the previous hyperon experiments at Fermilab, Jastrzembski [63] estimated that about 2 % of our 375 GeV hyperon beam were Σ^+ at a location 10 meters downstream of the target. Because our crystals were located about 15 m down stream of the target, it reduced the Σ^+ rate to 1 % inside the decay volume, which was defined from chamber SSD3 to WA. Of the 1 % Σ^+, only half of them decay to a proton and π^0, because the branching fraction of the Σ^+ decay to proton and π^0 is 51.6 % [10].

We started by reconstructing the nonchanneled Σ^+. Two important parameters were used in the lab coordinate system: R, the ratio of hyperon momentum to the baryon momentum, and THETA, the Σ^+ decay angle. From the two body decay kinematics, we expected the THETA versus R plot of the decay $\Sigma^+ \rightarrow p\ \pi^0$ to have a parabolic form as shown is Fig. 7.1 constructed from theoretical calculation. The curve on the right side corresponds to $\Sigma^+ \rightarrow p\ \pi^0$ decay and the curve on the left side corresponds to $\Sigma^+ \rightarrow n\ \pi^+$ decay. From this plot, we can decide which cuts we want

to use to select the Σ^+s. R > 0.6 would eliminate the $\Sigma^+ \rightarrow$ n π^+ decay. THETA < 800 μrad would include all the Σ^+ to proton decay. Fig. 7.2 shows the THETA versus R plot of the nonchanneling triggered data, run 4327. This run, along with the run 4329, is used to measure the polarization of the Σ^+ beam. Since we required at least one photon at the trigger, we mostly triggered the $\Sigma^+ \rightarrow$ p π^0 decay, that is why we cannot see the $\Sigma^+ \rightarrow$ n π^+ decay from the plot. To cut off the long-lived beam particles around R = 1 and THETA = 0, we had to set an upper limit on R and a lower limit on THETA. We also calculated the decay vertex, ZV, for each event. The ZV distribution after the R and THETA cut is shown in Fig. 7.3. SD3 is located at 0.0 and the crystals are at 120 cm. The peak at chamber WA (Z=1410 cm) was caused by the reconstruction program. The program artificially put the decay vertex of the events decaying downstream of WA at WA. We cut ZV from the SSD3 to upstream of WA in order to cut off the events at this peak. The cuts are summarized as:

0.6 < R < 0.96;

200 μrad < THETA < 800 μrad;

250 cm < ZV < 1250 cm.

After all these cuts, we calculated the missing mass squared of the $\Sigma^+ \rightarrow$ p π^0 using equation

$$m_0^2 = (\sqrt{\vec{p}_{\Sigma^+}^2 + m_{\Sigma^+}^2} - \sqrt{\vec{p}_p^2 + m_p^2})^2 - (\vec{p}_{\Sigma^+} - \vec{p}_p)^2, \tag{7.1}$$

where $\vec{p}_{\Sigma^+}$ and $\vec{p}_p$ are the measured hyperon and baryon momenta. Fig. 7.4 shows the missing mass squared distribution. We fit the missing mass squared to a Gaussian function and found the σ to be 0.0054 $(GeV/c^2)^2$ which is very close to the Monte Carlo estimation 0.005 $(GeV/c^2)^2$. We selected the events between -2σ to $+2\sigma$ as the Σ^+ event sample.

7.2 Reconstruction of Channeled Σ^+ Using a Channeling Cut

There are two ways to reconstruct the channeled Σ^+. This section discusses one way that uses the channeling energy loss cut. The next section discusses another way that

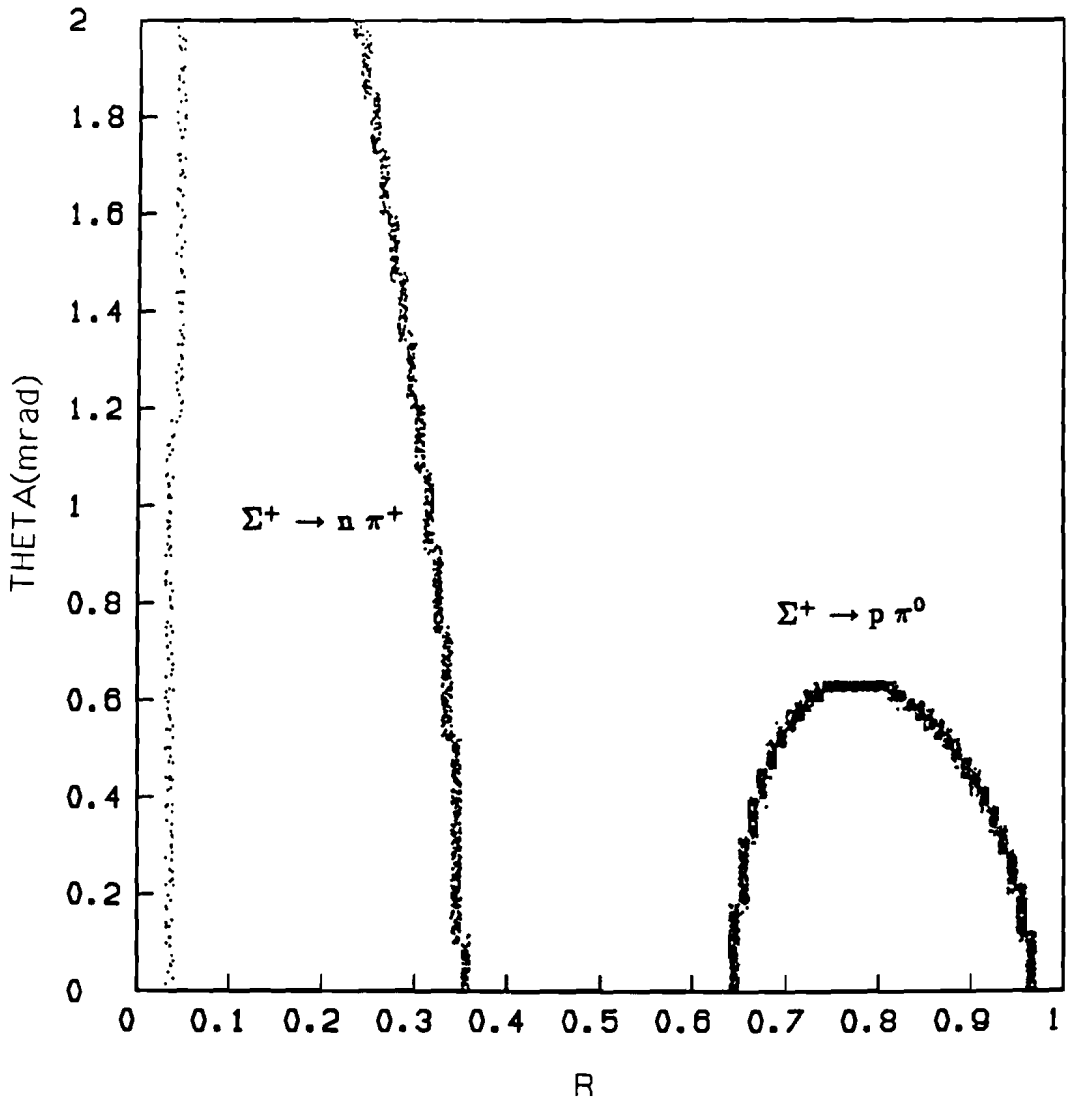

Figure 7.1: THETA versus R plot of theoretical calculation for Σ^+ decay.

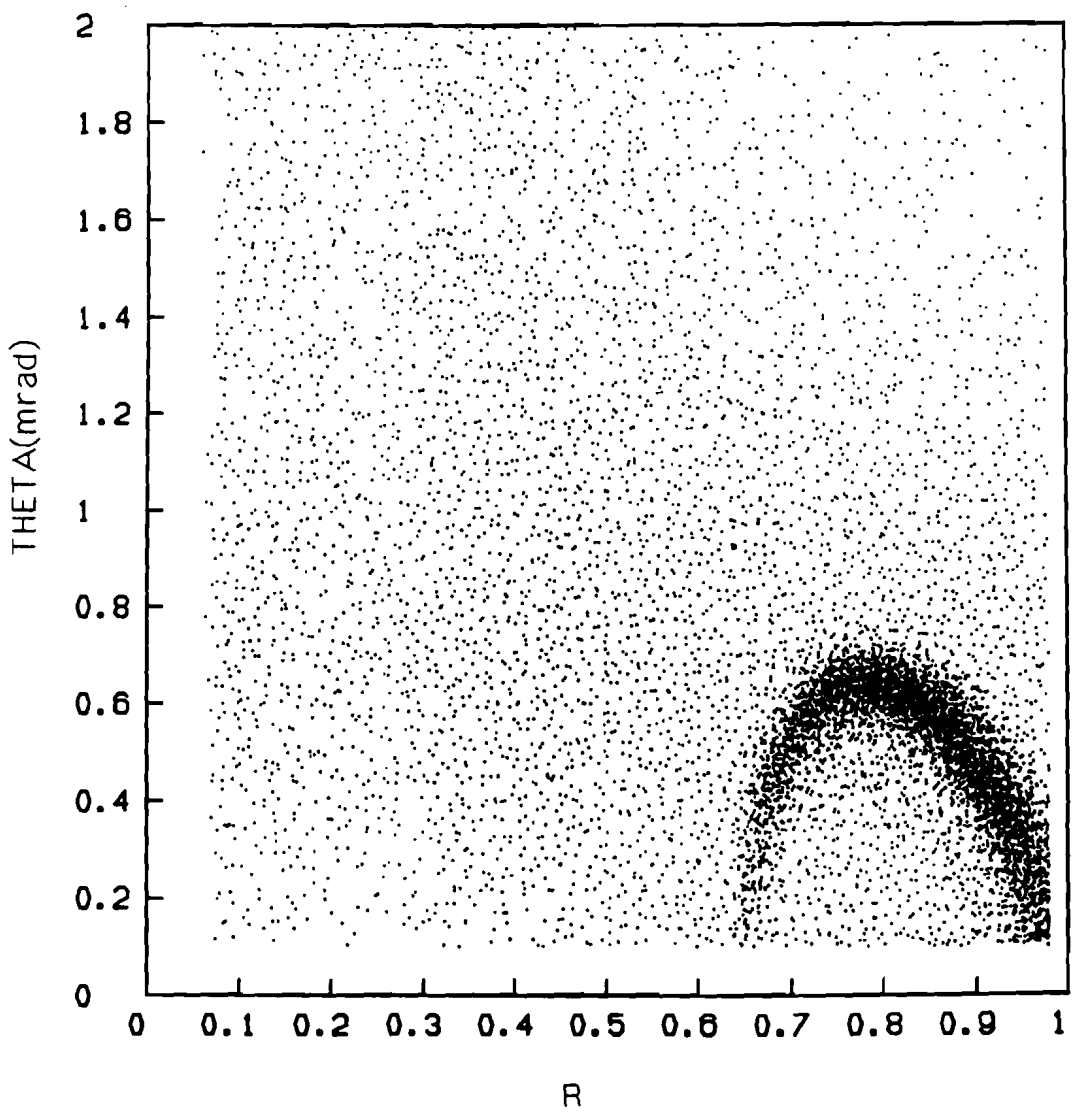

Figure 7.2: THETA versus R plot of the nonchanneling triggered data.

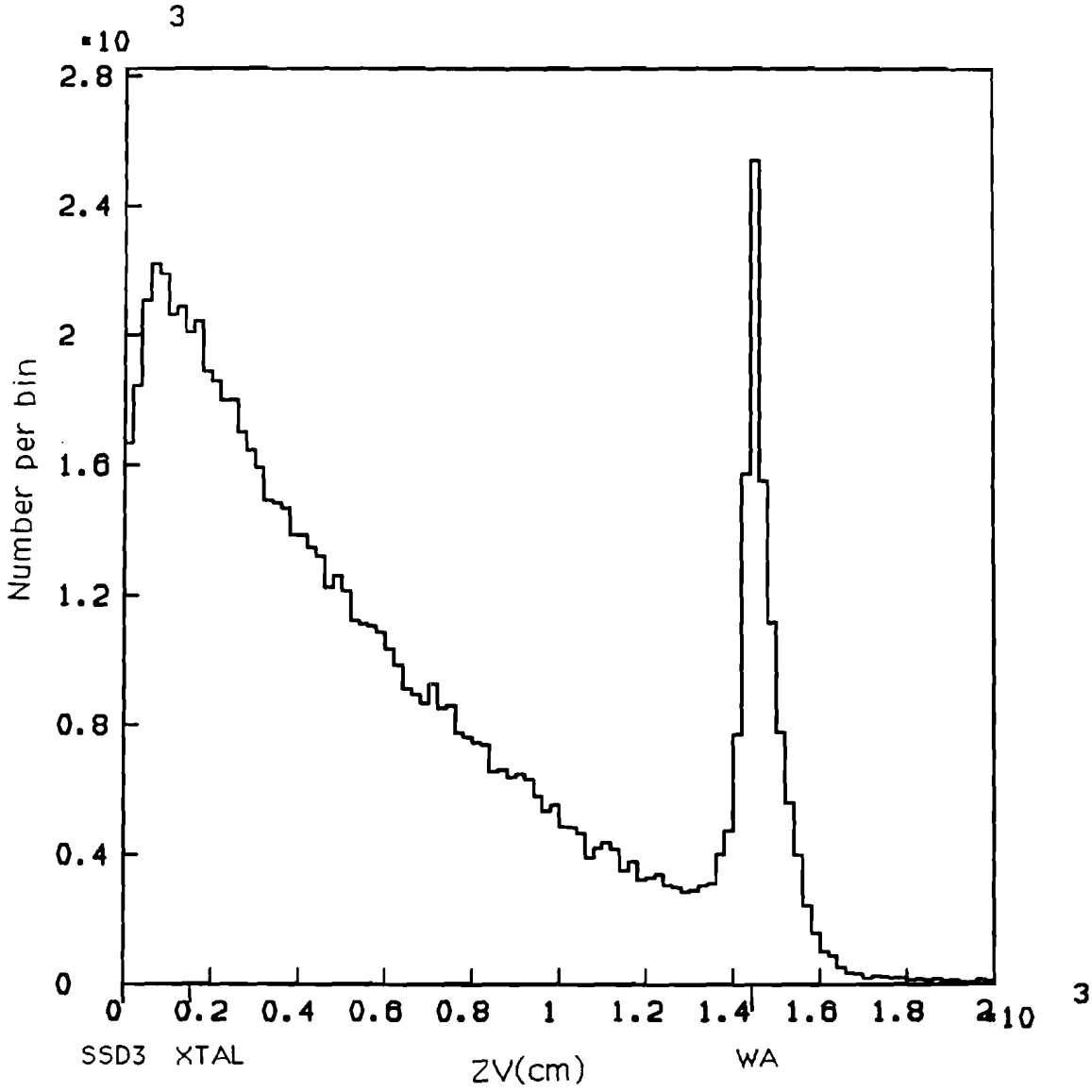

Figure 7.3: ZV distribution of the events after R and THETA cut.

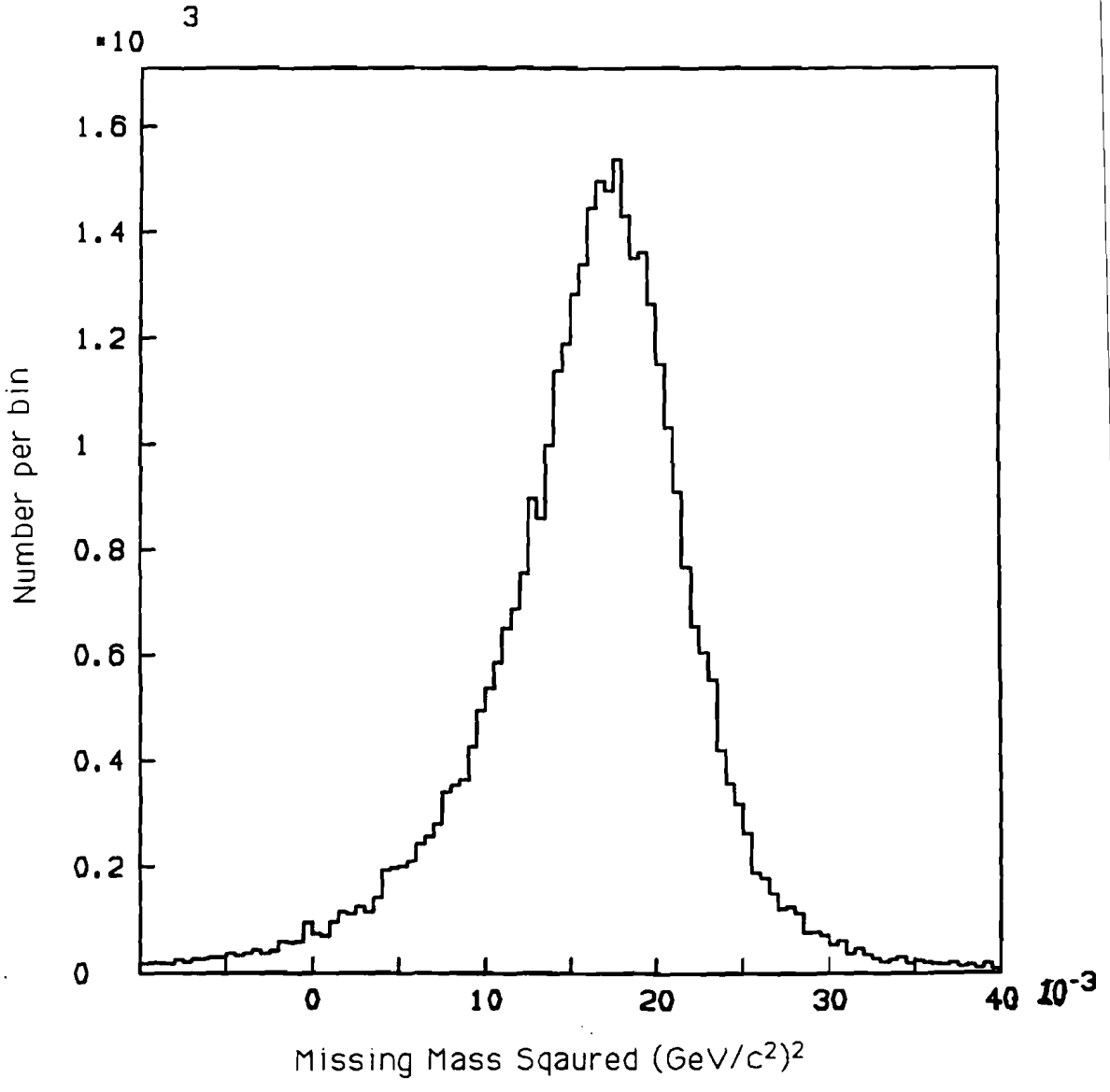

Figure 7.4: Missing mass squared distribution of nonchanneled Σ^+.

does not use the channeling loss cut.

To reconstruct the channeled Σ^+ with the channeling cut, we can perform two procedures. For the first procedure discussed in this section, we select the channeling events using a channeling cut. The next procedure is to isolate the 0.5 % channeled Σ^+ sample from the total sample of the channeling events. The R, THETA, and ZV cuts were also used but with the channeling modification.

The energy loss cut of only the center pad in the good crystal region was used as the channeling cut to select channeled particles. This cut was not as strong as the coincident energy loss cut and it did not give us a very clean channeling signal, but it gave us the maximum acceptance of channeling particles. The channeling particle bending angle, DTY, measured under this cut was -1.640 $\pm$ 0.030 mrad and 1.613 $\pm$ 0.065 mrad for the 5th and 2nd crystal respectively.

The basic channeling modification is the bending angle adjustment. We need to add the DTY to TY1, as the channeled hyperon angle before decaying, TY1′:

$$TY1' = TY1 + DTY.$$

This modification affects the decay angle as well as the ZV and missing mass squared distribution. Fig. 7.5 shows the THETA versus R plot after the bending angle modification for (a) nonchanneled Σ^+ from run 4327 and (b) channeled events. The THETA of nonchanneled Σ^+s were shifted to around 1.6 mrad, and the THETA of channeled events moved to 0.0. We then can apply the same cuts of R, THETA, and ZV to select the channeled Σ^+. The cut, R $<$ 0.96, corresponds to a 2.5 σ cut in R resolution around the peak at R = 1.0. The THETA cut, THETA $>$ 0.20 mrad, is a 4 σ cut in THETA resolution around the peak at THETA = 0.0 mrad. The peak was due to channeled, long-lived particles. The resolutions of R and THETA are related to the resolution of the momentum measurement and the angular resolution of our spectrometers modified by the DTY resolution, respectively.

Fig. 7.6 shows the missing mass squared distribution of channeled Σ^+s after the channeling cut and modified R, THETA and ZV cuts for (a) the 5th crystal and (b) the 2nd crystal. Comparing with the resolution of the missing mass squared of the nonchanneled particles, 0.0058 $(GeV/c^2)^2$, the resolution of the missing mass squared

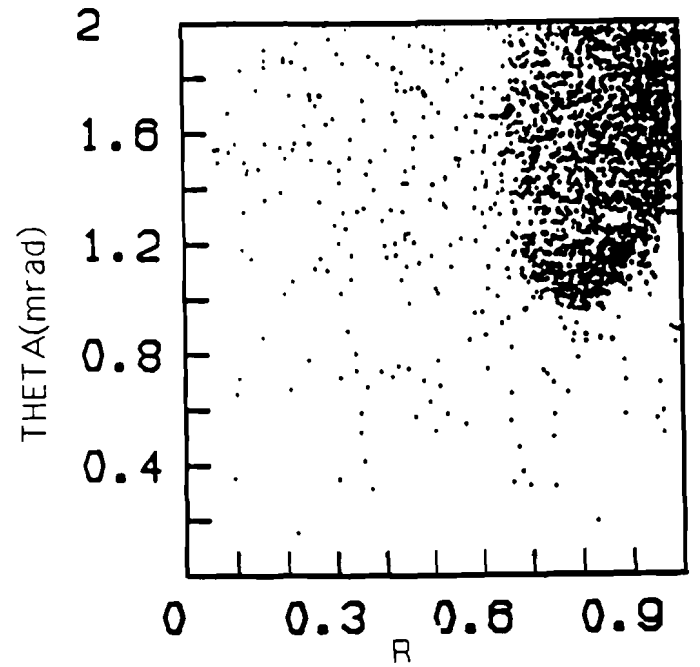

(a)

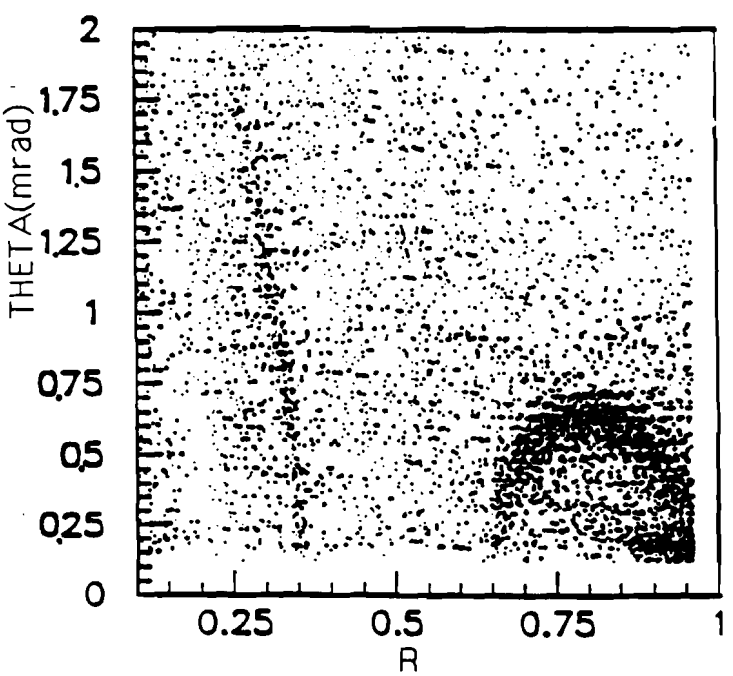

(b)

Figure 7.5: THETA versus R after bending angle modification for (a) nonchanneled Σ^+ and for (b) channeled events.

		5th crystal	2nd crystal	both crystals
Signal Area	σ $(GeV/c^2)^2$	0.0060	0.0080	
	total events	1234	1384	2618
	total background	172	279	451
	total Σ^+	1062	1105	2167
	f_s (%)	86.10	79.85	82.77
Background Area	total events	323	363	686
	total Σ^+	67	63	130
	total background	256	300	556
	f_b (%)	79.33	82.61	81.05

Table 7.1: Statistics of reconstructed channeled Σ^+ under the channeling cut.

of the channeled particles was about 20 % broader after the DTY modification. The resolution, σ from the fitted Gaussian distribution, of the missing mass squared was 0.0063 $(GeV/c^2)^2$ for the 5th crystal and 0.0080 $(GeV/c^2)^2$ for the 2nd crystal. The worse resolution of the bending angle DTY caused the degradation of the resolution in missing mass squared for the 2nd crystal. We fit the peaks to Gaussian functions and the backgrounds to second degree polynomial function.

Using the channeling cut, we reconstructed about 2167 channeled Σ^+s with a relatively small background. Table. 7.1 shows the σ and the numbers of channeled Σ^+ for each of the crystals. There were approximately 500 events for each crystal at each targeting angle. We defined the signal area from -2σ to $+2\sigma$ around the peak and the background area from -4σ to -2σ and from $+2\sigma$ to $+4\sigma$. The signal fraction, f_s, was defined as the number of Σ^+s over the number of total events in the signal area. The background fraction, f_b, was defined as the number of background over the number of total events in the background area. The σ and the number of signal and background events are listed in Table 7.1. Because of the small number of channeled Σ^+ events, we had a relatively large statistical error and therefore a large uncertainty in the polarization.

To recover more channeled Σ^+s, we have to sacrifice our signal to noise ratio.

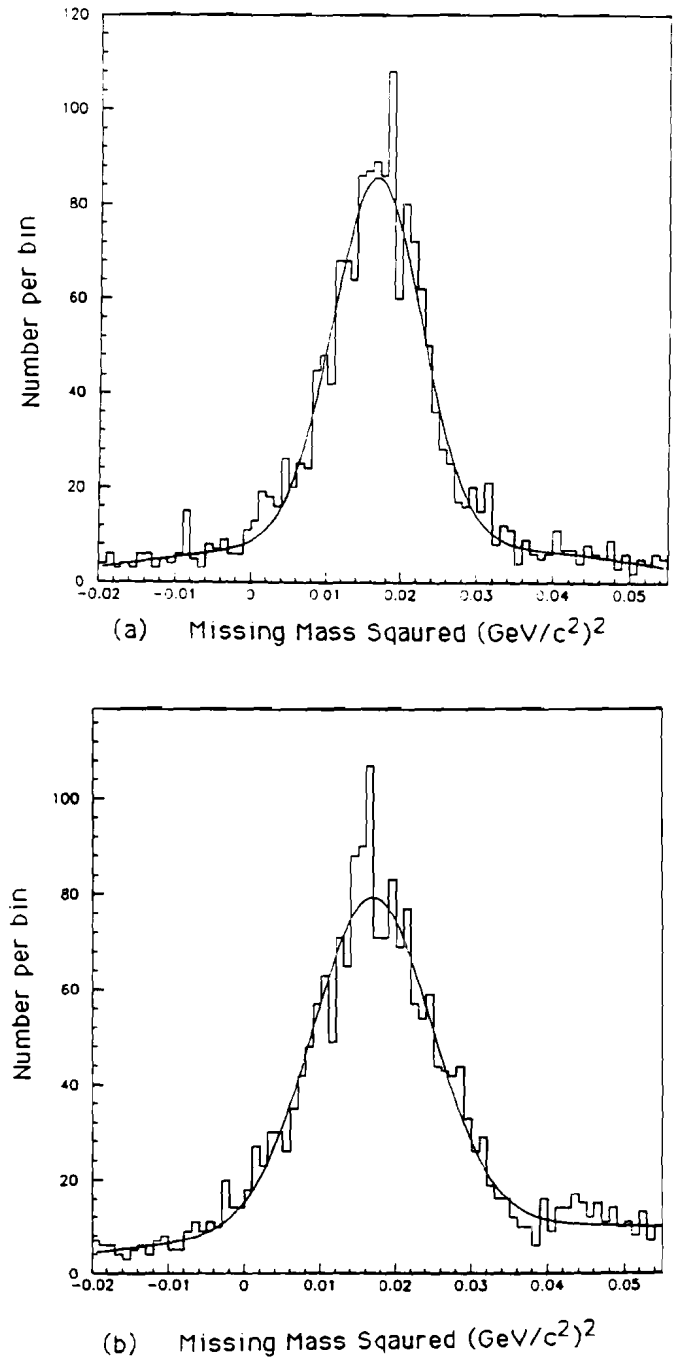

Figure 7.6: Missing mass squared distribution of channeled Σ^+ under the channeling cut for (a) the 5th crystal and (b) the 2nd crystal.

7.3 Reconstruction of Channeled Σ^+ without a Channeling Cut

The kinematics for the nonchanneled Σ^+ and channeled Σ^+ are different because of the bending angle modification. Fig. 7.5 showed the different distribution of THETA versus R for nonchanneled and channeled Σ^+s with the bending angle modification. Fig. 7.7 shows the different distributions of ZV for nonchanneled and channeled Σ^+ with the bending angle modification. We see that the ZV of the nonchanneled Σ^+ shifted to 120 cm, where the crystals were located. A cut of ZV > 250 cm may cut off these events. Comparing the differences, we can conclude that the normal Σ^+ cut with the DTY modification is a good cut for channeled Σ^+. The R cut would cut off most of the long-lived events, either channeled or nonchanneled. The background would come mostly from the nonchanneled long-lived interaction events which pass through our cuts.

We varied our cuts to maximize the ratio of the missing mass squared peak over the background. The final cuts were chosen as:

$0.6 < R < 0.96$;

$200\ \mu\text{rad} < \text{THETA} < 800\ \mu\text{rad}$;

$250\ \text{cm} < ZV < 1250\ \text{cm}$.

The missing mass squared distribution after the cuts are shown in Fig. 7.8 for (a) the 5th crystal and (b) the 2nd crystal. Notice the larger background in comparison with the distribution in Fig. 7.6. We fit the peaks to Gaussian functions and the backgrounds to second degree polynomial functions. The σ and the number of signal and background events are listed in Table 7.2.

We reconstructed a total of about 4041 channeled Σ^+ for both crystals. With these events, we can calculate the polarization of the Σ^+ after it went through the bent crystal, and therefore, measure the magnetic moment of the Σ^+.

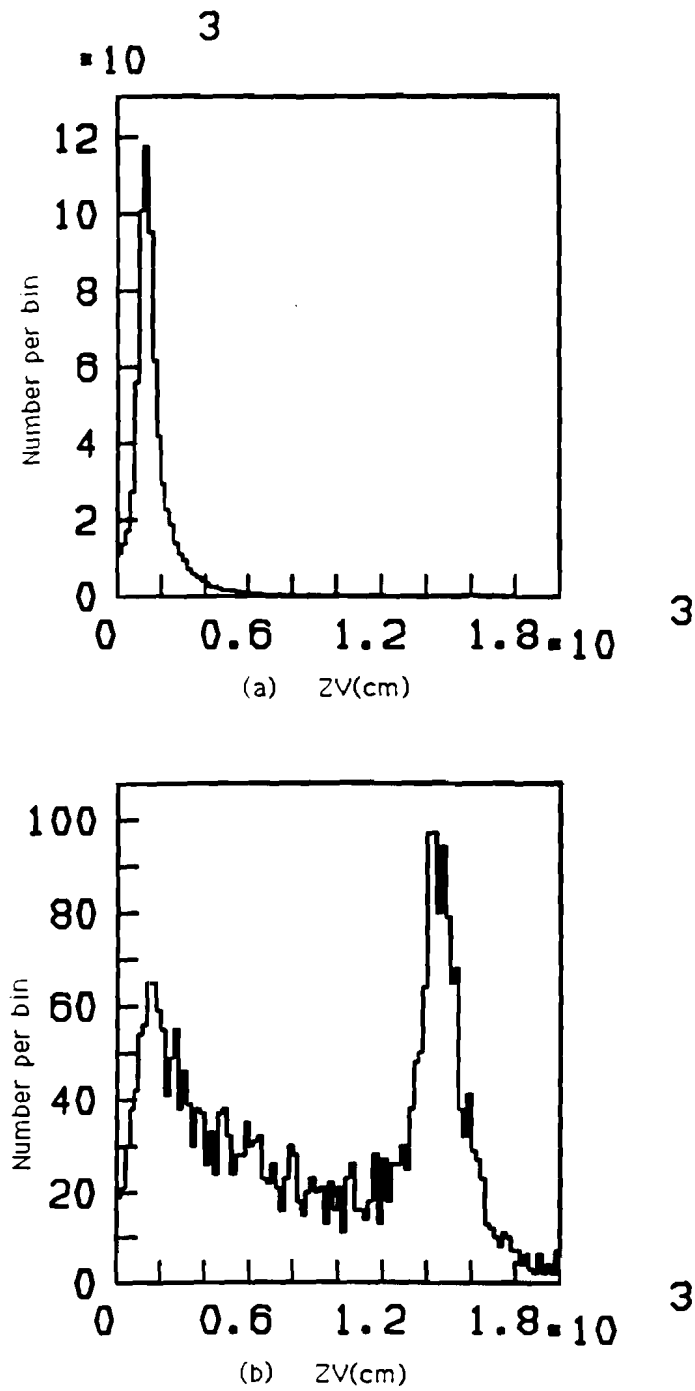

Figure 7.7: ZV distributions for (a) nonchanneled events and (b) channeled events.

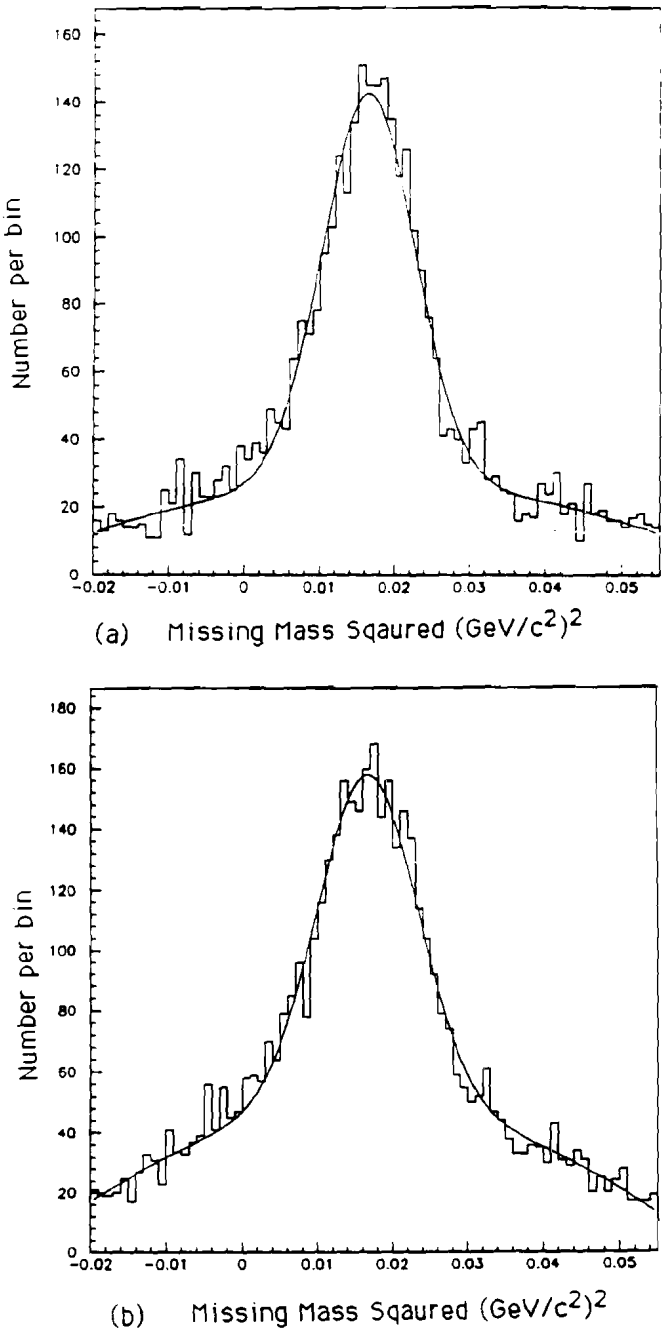

Figure 7.8: Missing mass squared distributions of channeled Σ^+ for (a) the 5th crystal and (b) the 2nd crystal. No channeling cut was used.

Signal Area		5th crystal	2nd crystal	both crystals
	σ $(GeV/c^2)^2$	0.0065	0.0080	
	total events	2920	3937	6857
	total background	1033	1783	2816
	total Σ^+	1887	2154	4041
	f_s (%)	64.64	54.71	58.93
Background Area	total events	1573	1911	3484
	total Σ^+	100	74	174
	total background	1473	1837	3310
	f_b (%)	93.66	96.15	95.00

Table 7.2: Statistics of reconstructed channeled Σ^+ and background without energy loss channeling cut.

Chapter 8

Measurement of the Spin Precession and Magnetic Moment of Σ^+

8.1 Polarization Measurement of the Σ^+ before the Crystals

The initial polarizations of the Σ^+ before the crystals were measured from nonchanneling trigger data. These data were taken at the same targeting angles, ± 4 mrad, as the channeling case.

The decay baryon distribution in the hyperon center of mass (CM) frame is a function of the polarization of the hyperon, $\vec{\mathbf{P}}$. The distribution of the proton in the Σ^+ CM frame after integrating over the azimuthal angle is given by

$$\frac{dN_i}{N_{0i} dcos\theta_i} = \frac{1}{2}(1 + \alpha \mathrm{P_i} \cos\theta_i), \tag{8.1}$$

where N_{0i} is the total number of events, θ_i is the angle between the baryon direction and the i axis (i = x, y and z) in the CM, and α is the asymmetry parameter of the decay $\Sigma^+ \rightarrow$ p π^0 ($\alpha = -0.98$ [10]). Including the acceptance of the apparatus,

equation (8.1) must be modified as

$$\frac{dN_i}{N_{0i}dcos\theta_i} = \frac{1}{2}A_i(1 + \alpha \mathbf{P}_i \cos\theta_i), \tag{8.2}$$

where A_i is the acceptance,which could be a function of θ_i and other parameters.

We used a bias cancelling technique to cancel the A_i. The distribution of the data with a positive targeting angle, i.e. with the polarization $\mathbf{P}^+$, can be written as

$$\frac{dN_i^+}{N_{0i}^+dcos\theta_i} = \frac{1}{2}A_i(1 + \alpha \mathbf{P}_i^+ \cos\theta_i). \tag{8.3}$$

And the equation for negative targeting angle, i.e. with the polarization $\mathbf{P}^-$, is

$$\frac{dN_i^-}{N_{0i}^-dcos\theta_i} = \frac{1}{2}A_i(1 + \alpha \mathbf{P}_i^- \cos\theta_i). \tag{8.4}$$

Assuming the same amplitude for the positive and the negative targeting angle, $\mathbf{P}_i^+ = -\mathbf{P}_i^-$, we can rewrite equation (8.4) as

$$\frac{dN_i^-}{N_{0i}^-dcos\theta_i} = \frac{1}{2}A_i(1 - \alpha \mathbf{P}_i^+ \cos\theta_i). \tag{8.5}$$

If we redefine $N_i^+ = \frac{dN_i^+}{N_{0i}^+dcos\theta_i}$ and $N_i^- = \frac{dN_i^-}{N_{0i}^-dcos\theta_i}$ and assume that A_i is the same for both targeting angles, from equation (8.3) and equation (8.5), we can derive

$$\frac{N_i^+ - N_i^-}{N_i^+ + N_i^-} = \alpha \mathbf{P}_i^+ \cos\theta_i. \tag{8.6}$$

From the plot of $\frac{N_i^+ - N_i^-}{N_i^+ + N_i^-}$ versus $\cos\theta_i$, we obtained the $\alpha \mathbf{P}_i^+$ from the slope of the distribution.

We used the nonchanneling triggered positive targeting angle run (RUN 4327) and negative targeting angle run (RUN 4329) to measure the Σ^+ polarization. There are about 65,000 Σ^+s in these two runs. These data were taken before the channeling data for the same configuration to measure the polarization of the Σ^+ beam. We divided the $\cos\theta_i$ distributions into 10 bins. To cancel the false asymmetry in the x direction due to the difference in beam phase space for positive and negative targeting beam, we also divided the hyperon beam angle in x (TX1) into 10 bins. We calculated $\mathbf{P}_i$ for all the TX1 bins and took the average. Fig. 8.1 shows the $\frac{N_i^+ - N_i^-}{N_i^+ + N_i^-}$ distribution as

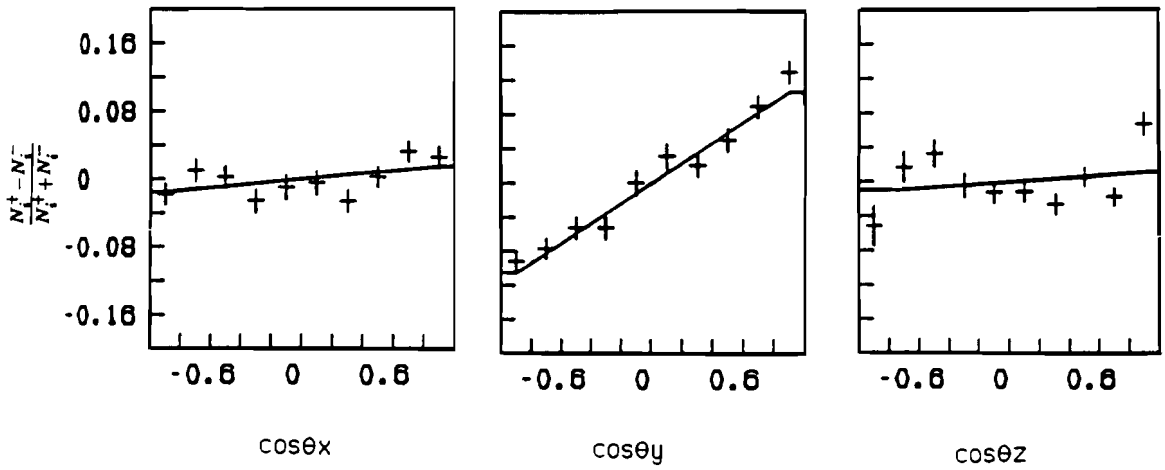

Figure 8.1: The $\frac{N_i^+ - N_i^-}{N_i^+ + N_i^-}$ distribution of nonchanneled Σ^+. About 65,000 nonchanneled Σ^+ are used here.

a function of $\cos\theta_i$. Because the Σ^+ was produced in the XZ plane, we only expect the Σ^+ to be polarized in the y direction. The flat distribution in x and z confirmed the zero polarization in the x and z directions. The polarization of the Σ^+ before the crystals is shown in Table 8.1. The errors shown are statistical only.

P_x	P_y	P_z
0.017 ± 0.007	0.119 ± 0.007	0.012 ± 0.008

Table 8.1: Polarization of Σ^+ before the crystals.

8.2 Polarization Measurement of the Σ^+ after the Crystals

8.2.1 Theoretical Estimation

After knowing the bending angle of the crystals, we can estimate the precession angle of the polarization vector in the crystals using equation (3.14). We used the value of the Σ^+ magnetic moment from the Particle Data Group (PDG) and $\gamma = E/m_0c^2$ =315. We estimated that for the 5th crystal the precession angle is $61.3° \pm 1.8°$ in the YZ plane, and for the 2nd crystal the angle is $-60.3° \pm 1.8°$. Fig. 8.2 illustrates the precession angle of the polarization vector for (a) the 5th crystal and (b) the 2nd crystal. The dashed lines are the initial and the predicted final polarizations of the channeled Σ^+.

8.2.2 Experimental Measurement with the Channeling Cut

The polarization of the Σ^+ after the crystals was obtained by using the channeled Σ^+ sample. We applied the bias cancelling technique, with the channeling modification, to the channeled Σ^+ that reconstructed using the channeling cut. Since there were only about 2000 channeled Σ^+ in this sample, we expected a large statistical error on the measured polarization value.

Fig. 8.3 shows the $\frac{N_i^+ - N_i^-}{N_i^+ + N_i^-}$ distribution as a function of $cos\theta_i$, i = x, y and z for (a) the 5th crystal and (b) the 2nd crystal. The measured polarizations of the channeled Σ^+ are listed in Table 8.2. Since there were only a few background events inside the signal area, we did not make any effort to deduct the possible background effects at this stage.

Fig. 8.4 shows the measured polarization and precession angle in the y-z plane. The polarization vector precessed in opposite directions for the two oppositely-bent crystals as expected. The precession angle was measured to be $51.2° \pm 23.2°$ for the 5th crystal and $-72.1° \pm 26.2°$ for the 2nd crystal which were close to the predicted value. The average precession angle was $60.4° \pm 17.4°$. The x component of the polarization was measured to be zero within statistical error.

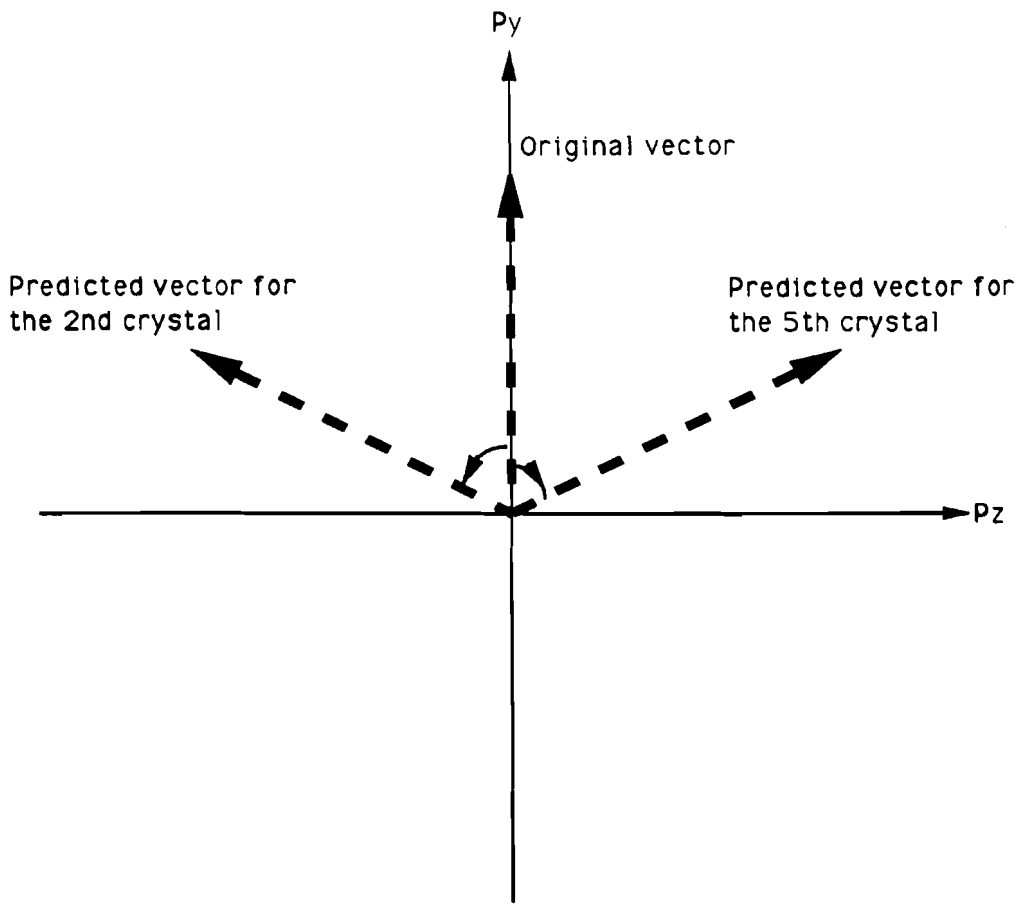

Figure 8.2: The initial polarization of Σ^+ and the final polarization of channeled Σ^+ from theoretical prediction for the 5th and 2nd crystals.

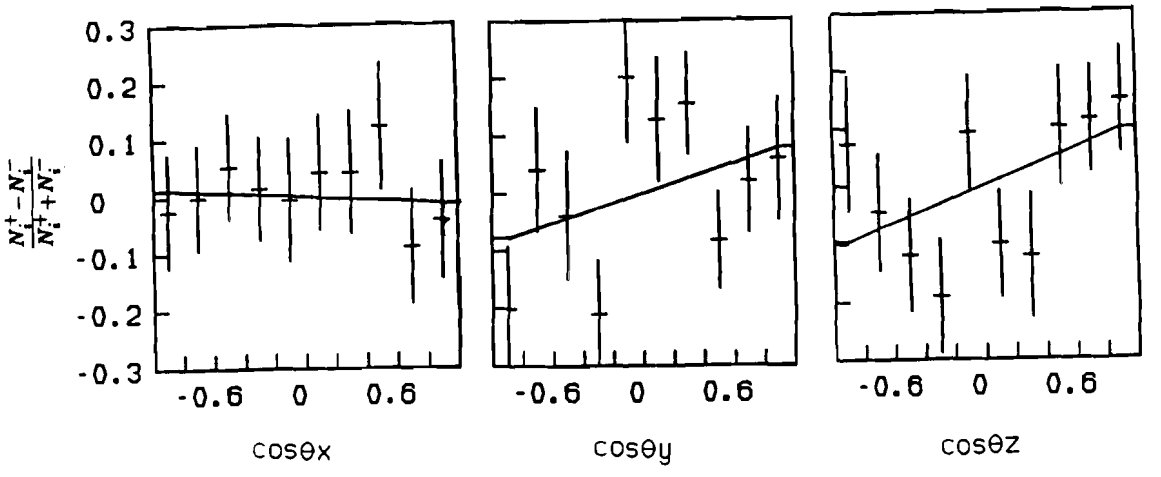

(a)

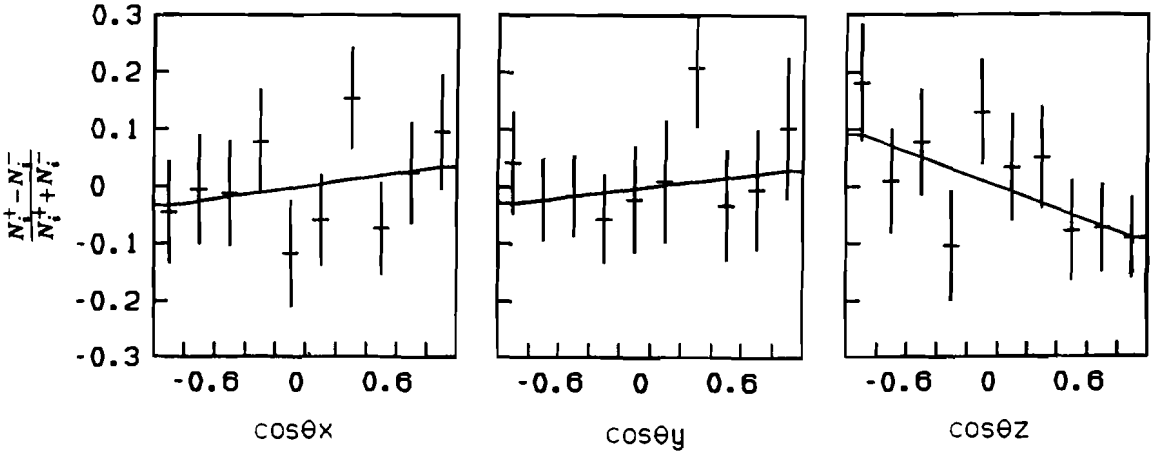

(b)

Figure 8.3: The $\frac{N_i^+ - N_i^-}{N_i^+ + N_i^-}$ distribution of the channeled Σ^+ with the channeling cut for (a) the 5th crystal and (b) the 2nd crystal.

5th crystal		x component	y component	z component
	P_{Σ^+}	-0.014 ± 0.054	0.085 ± 0.055	0.106 ± 0.054
2nd crystal	P_{Σ^+}	0.038 ± 0.054	0.032 ± 0.049	-0.100 ± 0.046

Table 8.2: Polarization results of the channeled Σ^+ with channeling cut.

The magnitude of the polarization vector was measured to be 0.136 ± 0.055 for the 5th crystal and 0.105 ± 0.048 for the 2nd crystal. The average value of the two crystals, 0.118 ± 0.036, was consistent with the original value, 0.12 ± 0.01, that we measured before the crystals. Within the precision of our measurement, there is no indication of a depolarization by the bent crystals.

8.2.3 Experimental Measurement without the Channeling Cut

We also measured the polarization of the channeled Σ^+ using twice as many events, which were reconstructed without the special channeling cut. Since there were twice as many events, the statistical error for this sample of events would be reduced by a factor of $\sqrt{2}$ relative to the sample with the channeling cut. However, we also expected that the systematic error might be enlarged because of the larger background.

The same bias cancelling technique was used to measure the polarization of the reconstructed channeled Σ^+s. From the decay baryon distribution, we measured the asymmetries for the events both in the signal area and the background area. The asymmetry was defined as: $\mathbf{A} = \alpha\mathbf{P}$. Since we know the α parameter for the Σ^+ decay, $\alpha = -0.98$, and the polarization of Σ^+, $\mathbf{P}$ could be obtained easily by dividing the $\mathbf{A}$ by -0.98. However, we don't know the α for the background, and thus won't be able to derive the polarization. This is not important for our purpose of subtracting the possible effect of the background events, because we can use the asymmetry, $\mathbf{A}$, instead of the polarization, $\mathbf{P}$

Fig. 8.5 shows the $\frac{N_i^+ - N_i^-}{N_i^+ + N_i^-}$ distribution in the signal area for (a) the 5th crystal and (b) the 2nd crystal. Fig. 8.6 shows the $\frac{N_i^+ - N_i^-}{N_i^+ + N_i^-}$ distribution in the background area for (a) the 5th crystal and (b) the 2nd crystal.

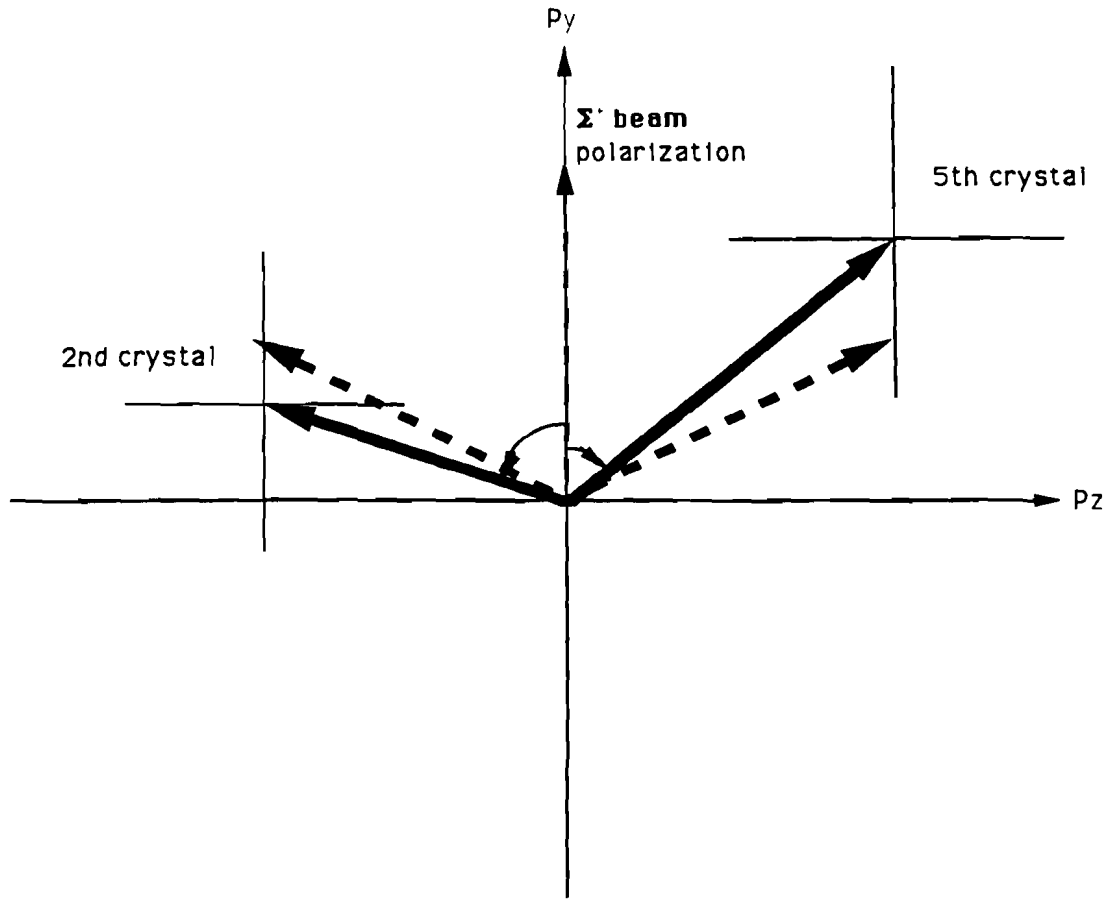

Figure 8.4: The polarization and precession angle of the channeled Σ^+ measured with the channeling cut. The dashed lines are the initial value and the theoretical predicted value.

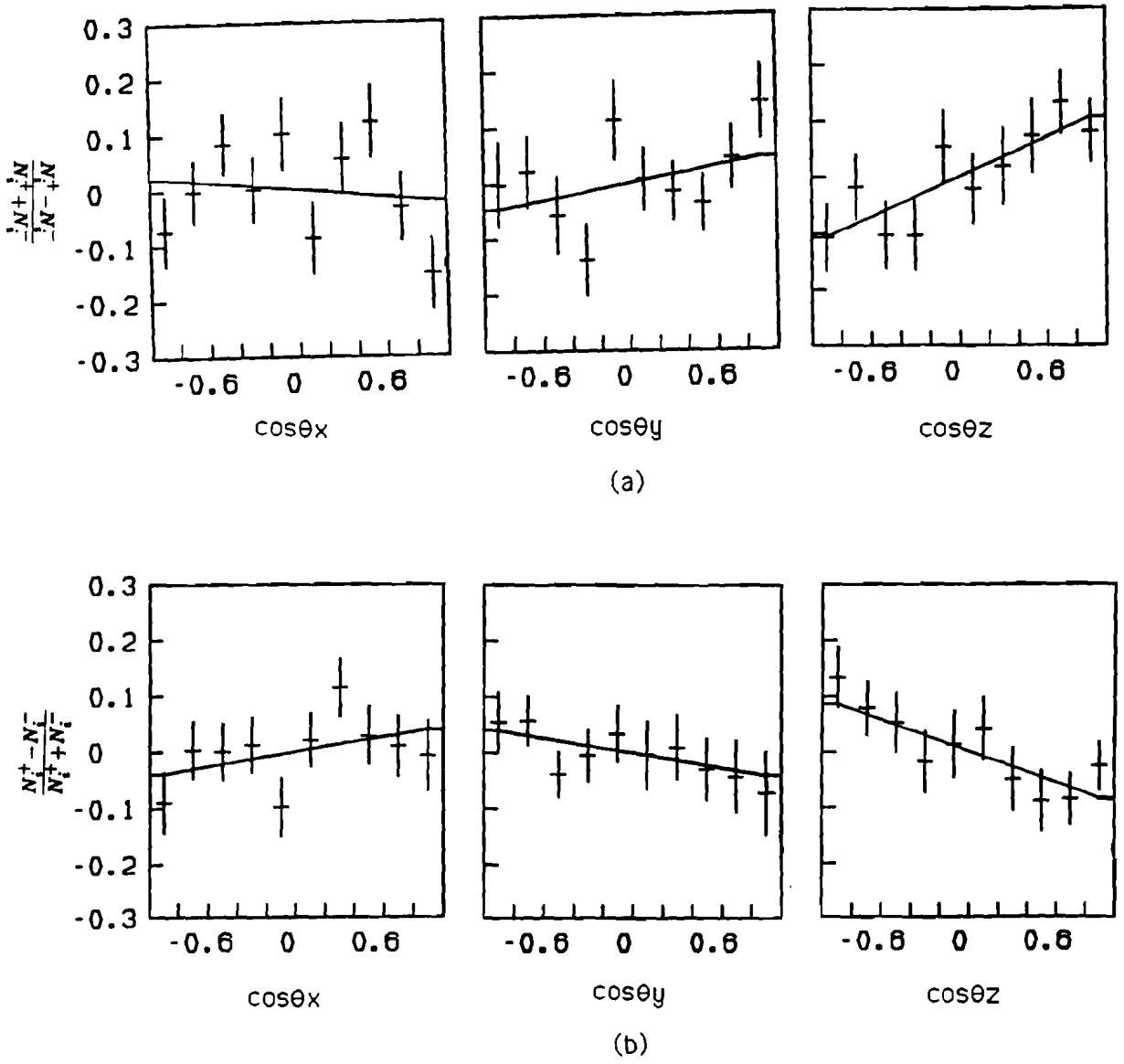

Figure 8.5: The $\frac{N_i^+ - N_i^-}{N_i^+ + N_i^-}$ distribution of the events in the signal area for (a) the 5th crystal and (b) the 2nd crystal.

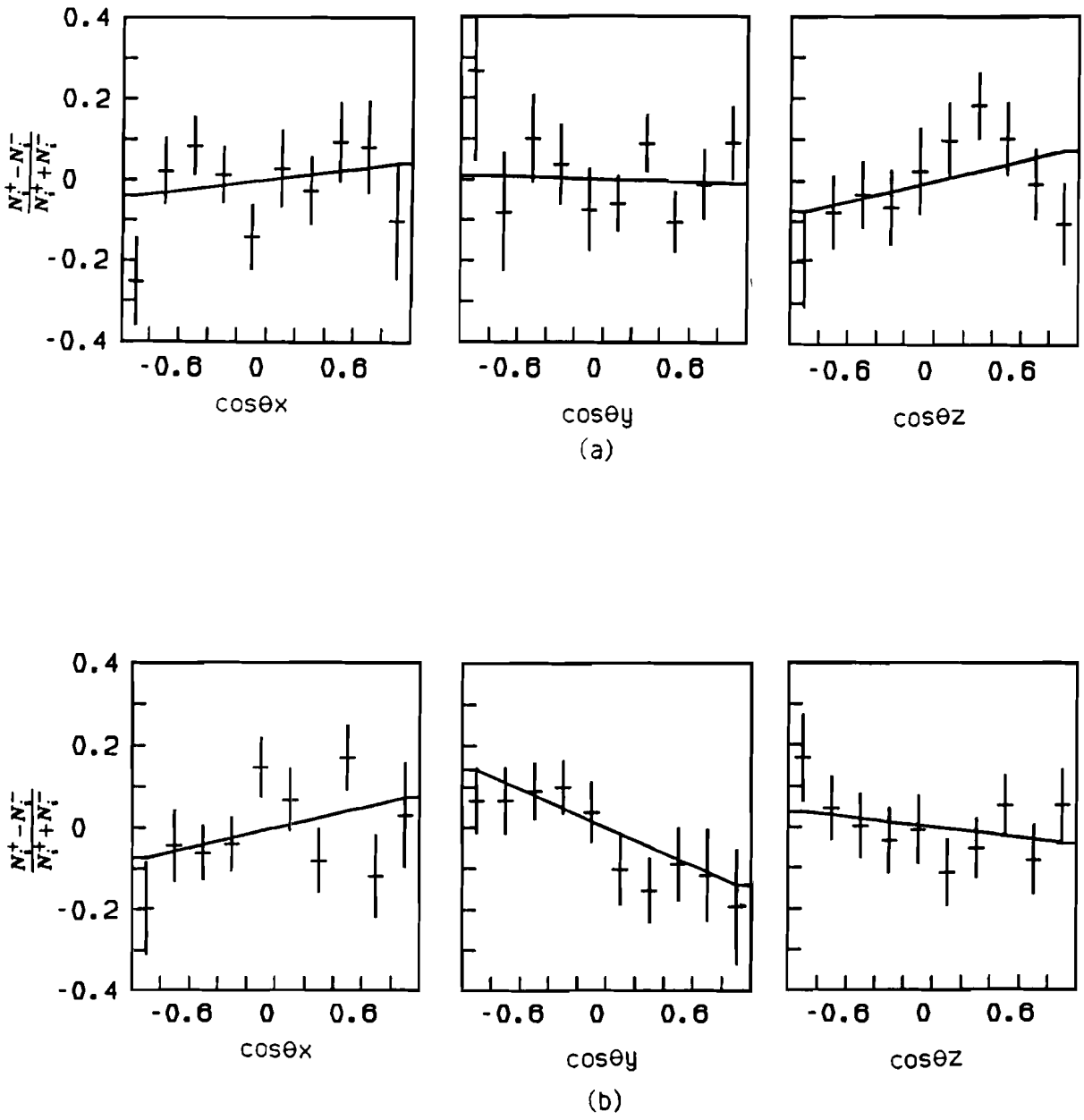

Figure 8.6: The $\frac{N_i^+ - N_i^-}{N_i^+ + N_i^-}$ distribution of the events in the background area for (a) the 5th crystal and (b) the 2nd crystal.

5th crystal		x component	y component	z component
	$\mathbf{A_s}$	0.024 ± 0.032	-0.050 ± 0.034	-0.116 ± 0.030
	$\mathbf{A_b}$	-0.043 ± 0.053	0.011 ± 0.055	-0.080 ± 0.050
	$\mathbf{P_{\Sigma^+}}$	-0.066 ± 0.064	0.091 ± 0.067	0.143 ± 0.061
	$\mathbf{A_B}$	-0.051 ± 0.060	0.018 ± 0.062	-0.078 ± 0.057
2nd crystal	$\mathbf{A_s}$	-0.044 ± 0.029	0.044 ± 0.029	0.093 ± 0.026
	$\mathbf{A_b}$	-0.080 ± 0.051	0.154 ± 0.048	0.041 ± 0.045
	$\mathbf{P_{\Sigma^+}}$	0.012 ± 0.074	0.056 ± 0.073	-0.144 ± 0.066
	$\mathbf{A_B}$	-0.084 ± 0.056	0.166 ± 0.053	0.038 ± 0.050

Table 8.3: Polarization results from our measurement. $\mathbf{A} = \alpha\mathbf{P}$ for Σ^+s.

We defined the background corrected asymmetry of channeled Σ^+ as $\mathbf{A_{\Sigma^+}}$; the asymmetry of background as $\mathbf{A_B}$; the measured asymmetry in the signal area as $\mathbf{A_s}$ and the measured asymmetry in the background area as $\mathbf{A_b}$. The relation between the background corrected asymmetry and the measured values is shown in the following equations:

$$\mathbf{A_s} = \mathrm{f_s}\mathbf{A_{\Sigma^+}} + (1 - \mathrm{f_s})\mathbf{A_B} \tag{8.7}$$

$$\mathbf{A_b} = (1 - \mathrm{f_b})\mathbf{A_{\Sigma^+}} + \mathrm{f_b}\mathbf{A_B}. \tag{8.8}$$

After measuring the $\mathbf{A_s}$, $\mathbf{A_b}$, f_s, and f_b, we calculated the asymmetry and therefore the polarization of the channeled Σ^+. Table 8.3 shows all the results with their statistical errors from our measurement. There was a significant asymmetry for the background of the 2nd crystal in the y direction.

Fig. 8.7 shows the background subtracted polarization vector of channeled Σ^+ compared with the initial vector and the theoretical predicted values(dashed line). The precession angle, $\Delta\phi$, of the Σ^+ polarization was measured to be $57.6° \pm 22.7°$ for the 5th crystal which was within 1σ of the predicted value. The angle for the 2nd crystal was $-68.7° \pm 27.2°$ which was also within 1σ of the predicted value. The average value was $62.2° \pm 17.4°$.

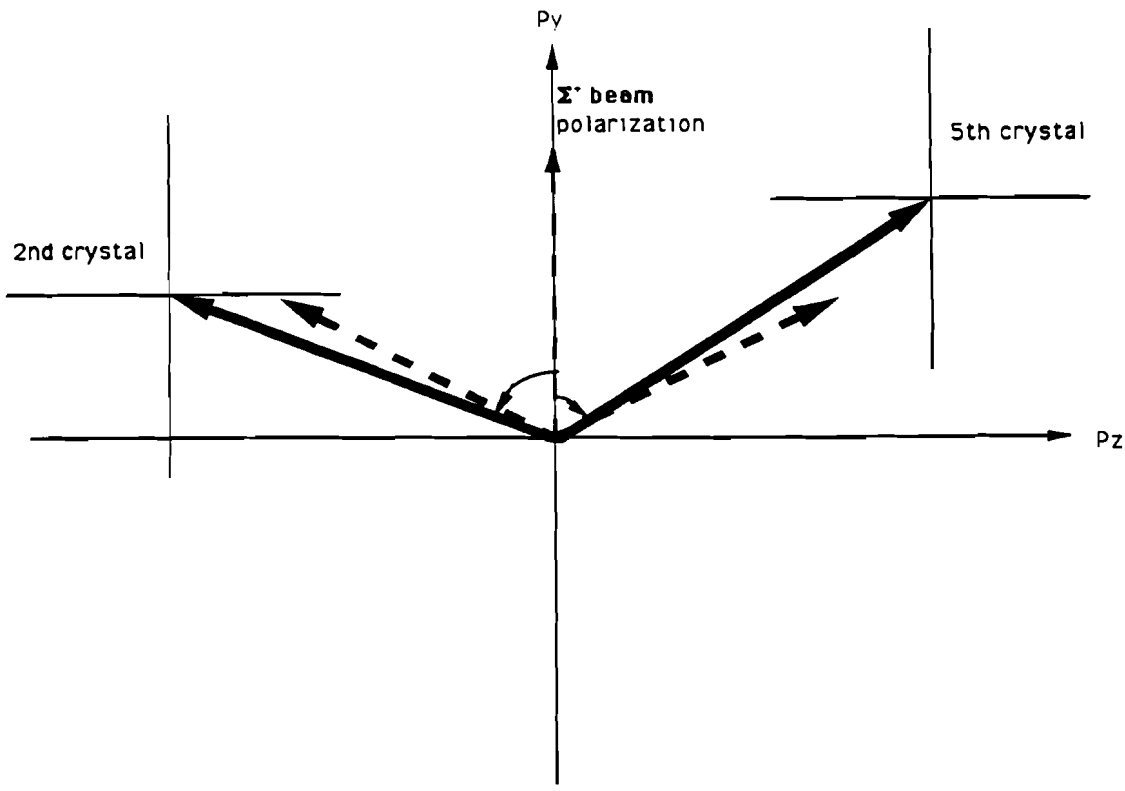

Figure 8.7: The polarization and precession angle of the channeled Σ^+ measured without the channeling cut. The dashed lines are the initial value and the theoretical predicted value.

	μ_{Σ^+} (μ_N) with channeling cut	μ_{Σ^+} (μ_N) no channeling cut
5th crystal	2.15 ± 0.61	2.32 ± 0.58
2nd crystal	2.74 ± 0.71	2.62 ± 0.73
Average	2.40 ± 0.46	2.44 ± 0.46
PGD	2.42 ± 0.05	

Table 8.4: Results of the μ_{Σ^+} measurement with statistical error only.

8.3 Magnetic Moment of the Σ^+

To calculate the magnetic moment of the Σ^+, we need to know the g factor of the Σ^+. The g factor was obtained by using equation (3.14) which is restated here:

$$\Delta\phi \approx \frac{(g-2)}{2}\gamma\Delta\theta_b.$$

After we knew the precession angle, $\Delta\phi$, and the bending angle, $\Delta\theta_b$, we calculated the g factor.

The magnetic moment was calculated using the equation

$$\mu_{\Sigma_+} = \frac{g}{2}\frac{m_p}{m_{\Sigma^+}}\mu_N, \tag{8.9}$$

where m_p is the proton mass, m_{Σ_+} is the Σ^+ mass and $\mu_N = e\hbar/2m_pc$ is the nuclear magneton.

We have two sets of results from two separate but correlated samples: the channeled Σ^+ with the channeling cut and without the channeling cut. The first set of data should be a subset of the second set. The results are listed in the Table 8.4 with only the statistical error.

The results from the two sets of data are consistent with each other. The results from the two crystals were independent and consistent within one σ. The average values of the magnetic moment of Σ^+ are 2.40 ± 0.46 and 2.44 ± 0.46, both consistent with the particle data group value 2.42 ± 0.05 within 1 σ. The large statistical error is due to the small number of channeled Σ^+ events.

8.4 Systematic Error

To study the systematic error of our measurement, we divided our whole channeled Σ^+ sample, called group A, into two smaller groups: group B and group C, by varying the cuts we used. Since we have few events, we made B a much bigger group than C so that we would have a relatively good measurement from B events and no direct measurement from C. We varied the cuts on the momentum ratio (R), the hyperon decay angle (THETA), the decay vertex (ZV), and the missing mass. We calculated the polarization of the Σ^+ under changes of the cuts, then compared the results with the polarization results under the unchanged standard cuts.

Since the results from group A and group B are highly correlated, we can not compare them directly. What we did was to calculate the possible results of group C from the results of group A and group B. Let the results from group A and B be denoted by x_A and x_B with errors σ_A and σ_B where x is a measured component of polarization and σ is its error. We can calculate the results of group C through the equations:

$$x_C = \sigma_C^2[\frac{x_A}{\sigma_A^2} - \frac{x_B}{\sigma_B^2}] \tag{8.10}$$

$$\sigma_C = [\frac{1}{\sigma_A^2} - \frac{1}{\sigma_B^2}]^{-\frac{1}{2}}. \tag{8.11}$$

After we had x_C and σ_C, we compared the results from group B with those of group C by calculating the χ^2 defined as:

$$\chi^2 = [\frac{x_B - x_C}{\sqrt{\sigma_B^2 + \sigma_C^2}}]^2. \tag{8.12}$$

We calculated the χ^2 for all the polarization components for all the cuts. The χ^2 distribution is shown in Fig. 8.8 together with the theoretical χ^2 distribution given by the connected line. For the most part, the distribution is consistent with the theoretical value. This does not mean there is no systematic error, but only means that the systematic errors are not as significant as the statistical error. However, there is an excess of cases at high χ^2. These are the places we looked carefully to determine our systematic errors. These large χ^2 occurred when we varied the ZV cut. In the ZV distribution of channeled Σ^+ shown in Fig. 7.7 (b), there is a big peak at

	μ_{Σ^+} (μ_N)
5th crystal	$2.15 \pm 0.61 \pm 0.40$
2nd crystal	$2.74 \pm 0.71 \pm 0.40$
Average	$2.40 \pm 0.46 \pm 0.40$
PDG	2.42 ± 0.05

Table 8.5: Final results of the μ_{Σ^+} measurement.

the crystals due to interactions. The cut we used, 250 cm < ZV < 1250 cm, could not cut all the events from the peak. There were a lot of background events which caused the large χ^2 in this polarization measurement. If we make tighter cuts on ZV, we would lose a lot of good signal events and therefore increase the statistical error. We took the average discrepancy of the precession angle between the different cuts as the systematic error. The systematic error for the precession angle is 14.8° which leads to a 0.40 μ_N error in the magnetic moment. There are other possible systematic errors caused by dechanneling, resolution of the momentum measurement etc., but they are an order of magnitude smaller than this one. For example, the systematic error caused by the bending angle resolution is about 2.2 % which is 1.3° on precession angle and 0.03 μ_N in the magnetic moment.

The final results of our measurement of Σ^+ magnetic moment with the statistical error and systematic error are shown in Table 8.5.

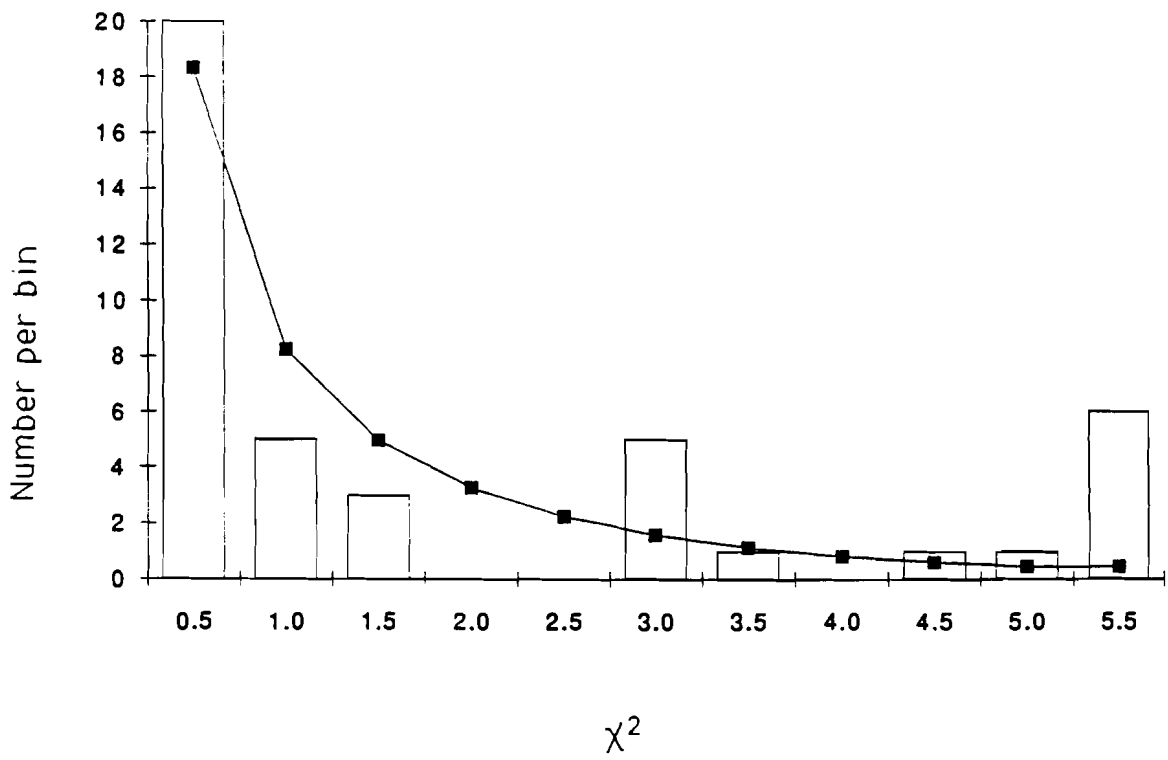

Figure 8.8: The χ^2 distribution of the systematic study. Connected line is the theoretical distribution.

Chapter 9

Conclusions

As I noted at the beginning of the thesis, this experiment was not designed to accurately measure the magnetic moment of the Σ^+. It was a test of a new idea, a new technique that might be applied to measure the magnetic moment of short-lived positively charged baryons such as the Λ_c^+. It is the first effort to measure a hyperon magnetic moment using channeling in bent crystals.

Our experiment demonstrated how effective the new technique was. We measured the magnetic moment of the Σ^+ to be $2.40 \pm 0.46 \pm 0.40\ \mu_N$ which is consistent with the world average value of $2.42 \pm 0.05\ \mu_N$ [10].

Fig. 9.1 shows the experimental values of the Σ^+ magnetic moment as a function of the year in which they were measured [69, 70, 71, 72, 73, 74, 75]. The large errors on the values before 1979 were due to the low beam fluxes and momenta. It is only after 1979 that the systematic error became dominant. The relatively large of error on our measurement using the channeling in bent crystals is due to the relatively low statistics.

There are several points that can be improved in future channeling experiments. Using a longer beam time and thicker crystals will certainly increase channeling data proportionally and therefore decrease the statistical error. The relation between the statistical error of the measured polarization (ΔP) and the number of measured events

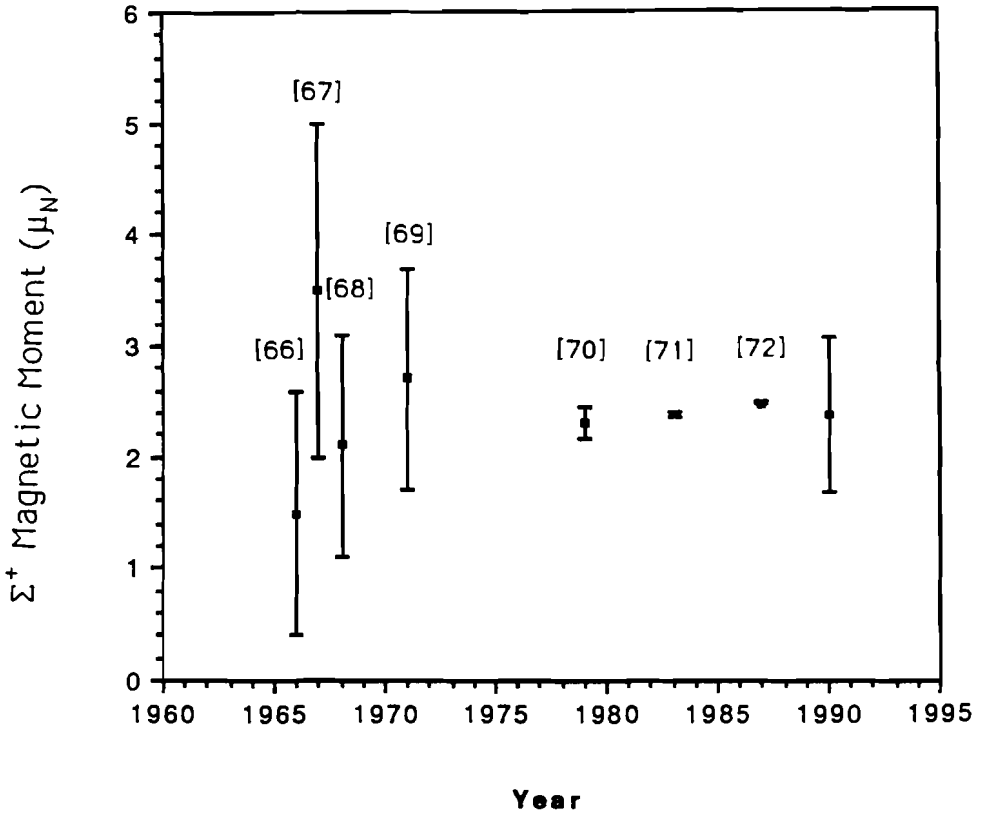

Figure 9.1: Experimental measurements of Σ^+ magnetic moment in history.

(N) [76] is shown in the following equation:

$$N = \frac{3 - (\alpha P)^2}{\alpha^2 (\Delta P)^2} \tag{9.1}$$

where α is the asymmetry parameter and P is the magnitude of the polarization. If the $(\alpha P)^2 \ll 3$, the relative error for the polarization can be written as

$$\frac{\Delta P}{P} = \frac{1}{\alpha P}\sqrt{\frac{3}{N}}. \tag{9.2}$$

Besides increasing the number of events, a larger bending angle will make the separation of the nonchanneled background from the channeling events easier. Since the spin precession angle is proportional to the bending angle (see equation 3.14), a larger bending angle can also precess the polarization through a larger angle. Fully depleted crystals will reduce the background and increase the signal events, and hence reduce the systematic and statistical errors.

Concerning the measurement of the magnetic moment of a charm hyperon such as the Λ_c^+, there are a lot of questions we have to answer before we can seriously discuss doing the experiment. There is no problem with the crystal apparatus, assuming that we make the improvements mentioned in the previous paragraph. The problems are with the character of Λ_c^+.

Λ_c^+ is the lowest-mass charm baryon. Like the Λ particle, the spins of the constituent quarks u and d are anti-parallel. According to the simple quark model: $\mu_{\Lambda_c^+} = \mu_c$. There have been several papers predicting the $\mu_{\Lambda_c^+}$ [27, 24]. The predicted $\mu_{\Lambda_c^+}$ values vary from 0.35 to 0.5 μ_N. A few thousand Λ_c^+ baroyns have been observed worldwide since it was first discovered in 1979 at Mark II [77]. Most of them were produced at e^+e^- colliders through either the decays of B mesons or the e^+e^- annihilations to $c\bar{c}$, observed by CLEO and ARGUS collaborations [78, 79]. The rest of them were from fixed target experiments using high energy photon (Fermilab TPS [80]) or hadrons (CERN ACCMOR and BIS collaborations [81, 82]) hitting a target. The Λ_c^+ mass and lifetime have been measured very accurately [10] to be 2284.9 ± 0.6 MeV/c^2 and $1.91^{+0.15}_{-0.12} \times 10^{-13}$ s.

Can we measure the magnetic moment of Λ_c^+ using crystal channeling now? The answer depends on the following questions: (1) Is there a strong Λ_c^+ source that we

can use to do the channeling experiment? An accurate measurement demands high statistics. (2) Is the Λ_c^+ source polarized? The spin precession method requires a polarized Λ_c^+ beam. (3) What kind of decay channel can we use to measure the asymmetry of the Λ_c^+? Is the decay parameter α for the decay channel big enough to produce a measurable asymmetry and therefore a polarization?

I will answer the questions in the reverse order.

To the question (3), the answer is yes. The Λ_c^+ two body weak decay channel $\Lambda_c^+ \rightarrow \Lambda\ \pi^+$ can be used to measure the Λ_c^+ polarization by measuring the Λ distribution. Bjorken [83] calculated the decay asymmetry parameter for this decay, $\alpha_{\Lambda_c^+}$, to be about −1. The CLEO collaboration [84] recently confirmed this prediction. They measured the $\alpha_{\Lambda_c^+}$ for that decay to be $-1.0^{+0.4}_{-0.0}$.

Due to the difficulties in measuring the neutral particles from the Λ_c^+ decay, there is almost no absolute branching ratio measurement. All the ratios are relative to the $\Lambda_c^+ \rightarrow$ p $K^-\ \pi^+$ decay. Unfortunately, the relative branching ratio for the $\Lambda\ \pi^+$ decay mode was measured to be 0.21 ± 0.06 [85], and if we take the absolute branching ratio of $\Lambda_c^+ \rightarrow$ p $K^-\ \pi^+$ as 0.039 ± 0.014 which was measured by CLEO [85], we would have the branching ratio of $\Lambda_c^+ \rightarrow \Lambda\ \pi^+$ less than 1%. Theorists predicted the branching ratio of this channel from 0.5% [86] to 5% [83]. Therefore, to use this decay channel, we need a very strong Λ_c^+ source. Note, however, that Bjorken [83] has suggested ways to measure the polarization of Λ_c^+ through its other decay modes.

The answer to the question (2), whether the Λ_c^+ is polarized, is also yes. Using 40 to 70 GeV neutrons impinging on a Carbon target, about 200 polarized Λ_c^+ were observed [87] by the BIS-2 collaboration at Serpukhov. The minimum absolute polarization of the Λ_c^+ was measured to be 0.5 ± 0.2. This may indicate that the polarization of Λ_c^+ is produced through strong interactions for the same reasons as the hyperon polarization production occurs. More work has to be done to check this phenomenon at higher energies.

The answer to question (1), if there is a strong Λ_c^+ source, is unfortunately no at this time. The Λ_c^+ from e^+e^- colliders do not have a narrow angular distribution that would match the channeling critical angle, typically several μrad. Besides, the energies of the Λ_c^+ produced this way, as well as those from the Neutron-Carbon

interactions, are too low to live through the crystals (few cm).

From the points mentioned above, we see that the measurement of the magnetic moment of Λ_c^+ is not realistic at this time because of the lack of a high energy and high intensity Λ_c^+ source through hadron production. It is possible that in the future, a polarized high energy Λ_c^+ beam may be achieved. In that sense, the measurement of magnetic moment of Λ_c^+ using channeling in bent crystals is feasible.

Bibliography

[1] M. Foucher *et al.*, Phys. Rev. Lett. **68**, 3004(1992). See Maurice Foucher's PhD thesis, Yale University.

[2] A. F. Elisev *et al.*, Phys. Lett. **88 B**, 387(1979).

[3] J. F. Bak *et al.*, Phys. Lett. **93 B**, 505(1980).

[4] S. I. Baker *et al.*, Phys. Lett. **137 B**, 129(1984).

[5] C. R. Sun *et al.*, Nucl. Instrum. Methods, **234 A**, 602(1985).

[6] S. I. Baker *et al.*, Nucl. Instrum. and Methods., **248 A**, 301(1986).

[7] S. P. Moller *et al.*, Phys. lett. **256 B**, 91(1991).

[8] A. A. Asseev *et al.*, Nucl. Instrum. and Methods., **309 A**, 1(1991).

[9] V. M. Samsonov and A. V. Khanzadeev, Preprint LNPI-1476, Leningrad (1989).

[10] Particle Data Group, Phys. Lett. B **239**, II.22(1990).

[11] Coleman and S. L. Glashow, Phys. Rev. Lett. **6**, 423(1960).

[12] J. Franklin, Phys. Rev. **172**, 1807(1968).

[13] P. C. Petersen *et al.*, Phy. Rev. Lett. **57**, 949(1986).

[14] N. Isgur and G. Karl, Phys. Rev. D **21**, 3175(1980).

[15] R. C. Verma and M. P. Khanna, Phys. Lett. **183 B**, 207(1987).

[16] A. Chodos *et al.*, Phys. Rev. D **9**, 3471(1974).

[17] A. Chodos *et al.*, Phys. Rev. D **10**, 2599(1974).

[18] T. DeGrand *et al.*, Phys. Rev. D **12**, 2060(1975).

[19] K. Ushio, Phys. Lett. **158 B**, 71(1985).

[20] K. Tsushima *et al.*, Phys. Lett. **205 B**, 128(1988).

[21] C. Chiu, J. Pasupathy and S. J. Wilson, Phys. Rev. D **33**, 1961(1986).

[22] Franklin, Phys. Rev. D **29**, 2648(1984).

[23] Ankenbrandt *et al.*, Phys. Rev. Lett. **51**, 863(1983).

[24] S. N. Jena and D. P. Rath, Phy. Rev. D **34**, 196(1986).

[25] E. M. Nyman and D. O. Riska, Nucl. Phys., **325 B**, 593(1989).

[26] J. Kunz and P. J. Mulders, Phys. Lett. **231 B**, 335(1989).

[27] D. P. Min and Y. Oh, Phys. Lett. **251 B**, 597(1990).

[28] J. Lindhard, Phys. Lett. **12**, 126(1964).

[29] S. Datz, T. S. Noggle, C. D. Moak, Nucl. Instrum. Methods **38**, 221(1965).

[30] M. W. Thompson, Morgan, Channeling (Wiley and Sons, New York, 1973), Chapter 1.

[31] D. S. Gemmel, and R. E. Holland, Phy. Rev. Lett. **18**, 304(1967).

[32] J. A. Ellison, Phy. Rev. B **13**, 1880(1976).

[33] J. A. Ellison, Phy. Rev. B **18**, 5948(1978).

[34] J. A. Ellison and S. T. Picraux, Phy. Rev. B **18**, 1028(1978).

[35] J. A. Ellison, Phy. Rev. B **12**, 4771(1975).

[36] J. Lindhard, K. Dan Vidensk. Selsk. Mat. Fys. Medd. **34**, No. 14(1965).

[37] R. B. Alexandar, P. T. Callanghan, and J. M. Poate, Phys. Rev. **9**, 3022(1974).

[38] M. A. Kumakhov, Radiat. Eff. **15**, 85(1972).

[39] I. J. Kim, Nucl. Phys. **B229**, 251(1983).

[40] H. Kudo, Nucl. Instrum. Methods, **189**, 609(1981).

[41] D. S. Gemmel, "Channeling and Related Effects," Rev. Mod. Phys. **46**, 1(1974).

[42] K. Hiroshi, Nucl. Instrum. Methods, **170**, 129(1980).

[43] R. A. Carrigan, Relativistic Channeling, eds. R. A. Carrigan and J. A. Ellison, Plenum, New York. 339(1987).

[44] W. M. Gibson, Relativistic Channeling, eds. R. A. Carrigan and J. A. Ellison, Plenum, New York. 101(1987).

[45] J. D. Jackson, Classical Electrodynamics, (Wesley, New York, 1975), Chapters 13, 15.

[46] H. Bethe, Ann. Phys., **5**, 325(1930).

[47] F. Block, Ann. Phys., **16**, 285(1933).

[48] U. Fanno, Ann. Rev. Nucl. Sci., **13**, 1(1963).

[49] Landau and Lipshitz,Electrodynamics of Continuous Media, (Wesley, Reading, Mass., 1960), Chapter 12.

[50] K. Detmann, Z. Phys., **272 A**, 227(1975).

[51] D. Pines, Elementary Excitations in Solids, (Benjamin, New York, 1964).

[52] H. Esbensen, J. A. Golovechenko, Nucl. Phys., **298 A**, 382(1978).

[53] S. P. Ahlen, Rev. Mod. Phys., **52**, 1(1980).

[54] C. R. Sun *et al.*, Nucl. Phys. **203 B**, 40(1982).

[55] E. N. Tsyganov, Fermilab TM-682 (1976).

[56] See S. M. Salman's Ph.D. thesis, SUNY at Albany (1982).

[57] R. L. Wijayawardana's Ph.D. thesis, SUNY at Albany (1985).

[58] V. G. Baryshevsky, Pis'ma Zh. Tekh. Fiz. **8** 182-184(Feb, 1979) [Sov. Tech. Phys. Lett. **5**, 182(1979)].

[59] V. L. Lyuboshits, Sov. J. Nucl. Phys. **31**, 509(1980).

[60] L. G. Pondrom Proceeding of 1982 DPF Summer Study on Elementary Particles and Future Facilities, P96, Snowmass, CO (1982).

[61] Private communications with V. M. Samsonov and A. V. Khanzadeev.

[62] T. R. Cardello *et al.*, Phys. Rev. D **32**, 1(1985).

[63] E. Jastrzembski, *Charged Hyperon Fluxes*, Hyperon Physics at the Tevatron, Workshop, Fermilab, 16, (1984).

[64] S. Hansen and S. Bracker, *Smart Camac Controller (SCC) Specifications*, Fermilab HN0063(1987); S. Hansen *et al.*, IEEE Trans. Nucl. Sci., **NS-34**, 1003(1987); M. Bernett *et al.*, *Smart Crate Controller Operating System User Reference Guide*, Fermilab PN0314 (1988); M. Bernett *et al.*, *Software for the Fermilab Smart Crate Controller*, Fermilab PN0330 (1987).

[65] *VME Readout Buffer (RBUF) Specifications*, Fermilab HN0082 (1989); R. Vignoni *et al.*, *Fermilab Fast Parallel Readout System for Data Acquisition*, Fermilab PN0331 (1987).

[66] *ACP68020 CPU Module 68KCPU*, Fermilab HN0071 (1986); *ACP User's Guide for Utilities*, Fermilab GA0002 (1987).

[67] A. E. Baumbaugh and M. D. Averett, *Motion Controller*, Fermilab RD Controls Design Note 43.1, (1989)

[68] Private communications with T. Nicol, Fermilab.

[69] V. Cook *et al.*, Phys. Rev. Lett. **17**, 223(1966).

[70] D. Kotelchuck *et al.*, Phys. Rev. Lett. **18**, 1166(1967).

[71] T. Mast *et al.*, Phys. Rev. Lett. **20**, 1312(1968).

[72] P. Alley *et al.*, Phys. Rev. D **3**, 75(1971).

[73] R. Settles *et al.*, Phys. Rev. D **20**, 2154(1979).

[74] C. Ankenbrandt *et al.*, Phys. Rev. Lett. **51**, 863(1983).

[75] C. Wilkinson *et al.*, Phys. Rev. Lett. **58**, 855(1987).

[76] J. Lach, internal unpublished memorandum, H-note 7 (30 Sept. 1975).

[77] G. S. Abrams *et al.*, Phys. Rev. Lett. **43**, 477(1979). G. S. Abrams *et al.*, Phys. Rev. Lett. **43**, 1555(1979).

[78] T. Bowcock *et al.*, Phys. Rev. Lett. **55**, 923(1985).

[79] H. Albrecht *et al.*, Phys. Lett. **207 B**, 109(1988).

[80] J. C. Anjos *et al.*, Phys. Rev. Lett. **60**, 1379(1988).

[81] S. Barlag *et al.*, Phys. Lett. **218 B**, 374(1989).

[82] A. N. Aleev *et al.*, Z. Phys. **23 C**, 333(1984).

[83] J. D. Bjorken, Phy. Rev. D **40**, 1513(1989).

[84] P. Avery *et al.*, Phys. Rev. Lett. **65**, 2842(1990).

[85] S. R. Klein, Intl. J. Mod. Phys. **8 A**, 1457(1990).

[86] J. G. Korner *et al.*, Phys. Lett. **78B**, 492((1983).

[87] A. N. Aleev *et al.*, Sov. J. Nucl. Phys. **43**, 395(1986).